UC Irvine
UC Irvine Electronic Theses and Dissertations

Title

Photodissociation Dynamics of CH2I2, OCS and CH3CHO

Permalink

https://escholarship.org/uc/item/8wr2h43n

Author

Toulson, Benjamin W.

Publication Date

2016

Copyright Information

Peer reviewed|Thesis/dissertation

UNIVERSITY OF CALIFORNIA,
IRVINE

Photodissociation Dynamics of CH_2I_2, OCS and CH_3CHO

DISSERTATION

submitted in partial satisfaction of the requirements
for the degree of

DOCTOR OF PHILOSOPHY

in Chemistry

by

Benjamin W. Toulson

Dissertation Committee:
Assistant Professor Craig Murray, Chair
Professor Filipp Furche
Professor Ara Apkarian

2016

DEDICATION

"Experiment is the only means of knowledge at our disposal.

Everything else is poetry, imagination"

- Max Planck

TABLE OF CONTENTS

LIST OF FIGURES

LIST OF TABLES

ACKNOWLEDGMENTS

CURRICULUM VITAE

Benjamin W. Toulson

2013-2016	Ph.D. in Chemistry University of California, Irvine, USA
2011-2013	Doctoral student University of Glasgow, UK
2009-2010	Assistant Research Scientist Lucite International, Redcar, UK
2007-2011	MSci in Chemistry with Industrial Experience, 1st University of Bristol, UK
2000-2007	Advanced Levels: Chemistry, Mathematics, and Physics Advanced Subsidiary: History King Edward VII School, Sheffield, UK

PUBLICATIONS

- Toulson, B. W., Alaniz, J. P., Hill, J. G. & Murray, C. Near-UV photodissociation dynamics of CH_2I_2. *Phys. Chem. Chem. Phys.* **18**, 11091–11103 (2016).

- Toulson, B. W. & Murray, C. Decomposing the first absorption band of OCS using photofragment excitation spectroscopy. *J. Phys. Chem. A.* **120**, 6745–6752 (2016).

- Toulson, B. W. & Murray, C. OCS photodissociation: imaging the $S(^1D)$ channel, *in prep.*

- Toulson, B. W. & Murray, C. OCS photodissociation: imaging the $S(^3P)$ channel, *in prep.*

- Kapnas, K., Toulson, B. W. & Murray, C. Near-UV photodissociation dynamics of CHI_2Cl, *in prep.*

- Toulson, B. W., Kapnas, K. Fishman, D. A. & Murray, C. Acetaldehyde photochemistry, *in prep.*

- Toulson, B. W. & Murray, C. Acetone photochemistry, *in prep.*

PRESENTATIONS

September 2013	Presented talk at AirUCI retreat, Lake Arrowhead, CA.
January 2014	Joint talk with theoretician J. Vincent, AirUCI, Laguna Beach, CA.
June 2014	Talk at the 69th International Symposium on Molecular Spectroscopy (ISMS), University of Illinois, Urbana-Champaign.
July 2015	Poster presentation at the 25th Dynamics and Molecular Collisions (DMC) conference, Asilomar, CA.

TEACHING ASSISTANTSHIPS

Spring 2013	General Chemistry 1B
Fall 2013	Quantum Mechanics 131A
Summer 2014	AirUCI high school teacher workshop
Fall 2014	Quantum Mechanics 231A (Graduate course)
Fall 2015	Quantum Mechanics 131A
Winter 2015	General Chemistry 1A
Spring 2016	Physical Chemistry laboratory 153L

AWARDS

2015	Associated graduate students travel award
2016	Graduate dissertation fellowship

ABSTRACT OF THE DISSERTATION

Photodissociation Dynamics of CH_2I_2, OCS and CH_3CHO

By

Benjamin W. Toulson

Doctor of Philosophy in Chemistry

University of California, Irvine, 2016

Professor Craig Murray, Chair

Chapter 1 outlines the focus of this thesis, understanding the mechanism of breaking a chemical bond following absorption of light.

In Chapter 2 the design, construction and calibration of a new velocity-map direct current slice ion imaging (VMI) time-of-flight mass spectrometer is described. Wavelength tunable pulsed lasers are used to selectively pump (dissociate) a target molecule, and probe (ionize) the fragments. Combing the techniques, correlated photofragment quantum state distributions can be explored.

Chapter 3 investigates the near-UV photodissociation dynamics of CH_2I_2 using ion imaging over a range of excitation wavelengths. Ground state $I(^2P_{3/2})$ and spin-orbit excited $I^*(^2P_{1/2})$ atoms were probed using 2+1 resonance-enhanced multiphoton ionization (REMPI) or with single-photon VUV ionization. Analysis of the ion images shows that, regardless of iodine spin-orbit state, ~20% of the available energy is partitioned into translation E_T indicating that the CH_2I co-fragment is formed highly internally excited. A refined C–I bond dissociation energy of $D_0 = 2.155 \pm 0.008$ eV is determined.

In Chapter 4 the photoproducts of OCS after UV excitation has been followed with photofragment excitation spectroscopy (PHOFEX), using REMPI to state-selectively monitor $S(^1D)$ and $S(^3P_{2,1,0})$ products while the pump wavelength was scanned. Probing the major $S(^1D)$ product results in a broad, unstructured action spectrum that reproduces the overall shape of the first absorption band. In contrast spectra obtained probing $S(^3P)$ products display prominent resonances superimposed on a broad continuum; the resonances correspond to the diffuse vibrational structure observed in the conventional absorption spectrum. The vibrational structure is assigned to four progressions, each dominated by the C–S stretch, following direct excitation to quasi-bound singlet and triplet states. The results confirm a recent theoretical prediction that direct excitation to the $2^3A''$ state can occur in OCS.

In Chapter 5 ion imaging measurements of CH_3 fragments from photolysis of CH_3CHO reveal multiple pathways to the same set of products. By systematically exploring product formation over a timescale of picoseconds to nanoseconds, and wavelengths between 265-328 nm, an evolving picture of the dynamics is found. Evidence to suggest that the three-body CH_3+CO+H pathway remains closed at all wavelengths is presented.

1 Introduction

This thesis focuses on understanding photodissociation, the process of breaking chemical bonds induced by the absorption of light.

$$AB + h\nu \rightarrow AB^* \rightarrow A + B$$

A and B may be atomic or polyatomic, $h\nu$ is the energy of a photon with frequency ν, and AB* is an excited state. Dissociation to form separate fragments A + B requires the photon energy must exceed the bond dissociation energy. The aim is to understand what governs motion at an atomic scale, i.e. what forces act on the nuclei.

1.1 Quantum mechanics

It is a postulate of quantum mechanics that the state of a system is fully described by the wavefunction $\Psi(R, r, t)$, where the spatial coordinates for the nuclei and electrons are denoted R and r, respectively, and time is labeled t. It is also postulated that the dynamical evolution of the wavefunction with time is given by the solution to the Schrödinger equation.[1,2]

$$i\hbar \frac{\partial}{\partial t} \Psi(R, r, t) = \hat{H}\Psi(R, r, t)$$

If we could accurately solve the Schrödinger equation for any molecule then we would understand how the system would evolve with time. The solutions are the eigenstates $\Psi(R, r, t)$, for non-stationary systems the solutions depend on time.

The non-relativistic Hamiltonian is given by the sum of kinetic and potential energy,

$$\hat{H} = \hat{T}_N(R) + \hat{T}_e(r) + \hat{V}(R,r)$$

where $\hat{T}_N$ is the nuclear kinetic operator, $\hat{T}_e$ is the electronic kinetic energy operator and the $\hat{V}(R,r)$ the potential energy operator.

$$\hat{T}_N(R) = -\sum_j \frac{\hbar^2}{2M_j} \nabla_j^2 \qquad\qquad \hat{T}_e(r) = -\sum_i \frac{\hbar^2}{2m_e} \nabla_i^2$$

The indices i, j indicate the sum over all electrons and nuclei respectively, ∇^2 is the Laplacian involving derivatives with respect to nuclear coordinates. m_e and M_j are the masses of the electrons and nuclei. If we assume that the potential energy function does not depend on time (as is written above), separation of variables then yields

$$\Psi(R, r, t) = \psi(R,r)\, f(t)$$

The Schrödinger equation can then be rewritten

$$i\hbar \frac{1}{f(t)} \frac{d}{dt} f(t) = \frac{1}{\psi(R,r)} \hat{H}\psi(R,r)$$

Noting that the left hand side depends only on time, and the right only on position, both sides must be equal to a constant. Upon rearrangement, we arrive at the time-independent Schrödinger equation

$$\hat{H}\psi(R,r) = E\psi(R,r)$$

1.2 Born-Oppenheimer approximation

Unfortunately exact solutions of the Schrödinger equation for multi-electron problems, i.e. Chemistry, are not possible. The Born-Oppenheimer approximation assumes that the nuclear and electronic motions can be decoupled owing to the large difference in masses $m_p/m_e \sim 1840$, the Hamiltonian can then be split into

$$\hat{H} = \hat{T}_N(R) + \hat{H}_e(r, R)$$

and wavefunction describing the system is assumed separable into nuclear and electronic wavefunctions, $\chi_i(R)$ and $\varphi_i(r, R)$, over all nuclei i, respectively

$$\psi^{BO}(\text{R}, \text{r}) = \chi_i(R)\varphi_i(r, R)$$

The electronic Schrödinger equation can be solved for fixed nuclei, to find the electronic energy $V_i(R)$.

$$\hat{H}_e(r, R)\varphi_i(r, R) = V_i(R)\varphi_i(r, R)$$

Repeatedly solving the electronic Schrödinger equation at different nuclear coordinates generates a potential energy surface (PES). The nuclear dynamics can then be found with classical, quasi-classical or quantum mechanical methods. The accuracy of the calculated dynamics relies on underlying electronic energies $V_i(R)$.

1.3 **Potential energy surfaces**

A potential energy surface describes how the energy of stationary molecular electronic states changes as a function of nuclear coordinates. The paradigm view is that molecular dynamics can be understood from the properties of the PES, as intuitive classical dynamics can be visualized on surfaces. The generation of global *ab initio* electronic surfaces, with accurate energies, gradients and surface coupling remains a formidable task for polyatomic molecules. The PES has 3N-6 dimensions for a nonlinear molecule with N nuclei. 3 degrees of freedom are associated with translation, and a further 3 with rotation. Alternative methods that can calculate molecular dynamics without pre-computed potential energy surfaces are gaining popularity.[3,4]

Both the timescale and the motions involved in breaking a chemical bond depend on the potential energy surface(s) that a molecule must traverse. Dissociation on a repulsive surface can be complete on the timescale of a vibration, femtoseconds (10^{-15} s). If the process occurs over picoseconds (10^{-12} s), the molecule may rotate prior to dissociation. For a polyatomic molecule, there are multiple bonds that can break, and energy can be distributed into product translational, vibrational and rotational excitation. The apportionment of energy into products reflects the characteristics of the PESs, describing how the molecule dissociated. Energy disposal provides a fingerprint of atomic motions, and can reveal whether a barrier to dissociation is present, the nature of a bottleneck (transition state), and if an intermediate complex forms. Photophysical process can also occur: radiationless transitions in molecules are often an important step en-route to dissociation. Photodissociation provides an experimental method to probe radiationless transitions between multiple PESs away from equilibrium geometries.[5]

Understanding photochemistry at a molecular level can lead to predictive power: which bond will

break, what is the branching between different accessible product channels, are multiple PESs important?[5]

1.3.1 Adiabatic and diabatic representations

The adiabatic representation uses the Born-Oppenheimer electronic wavefunctions, $\psi^{BO}(R, r)$. The Born-Oppenheimer wavefunctions are only valid when derivatives of the electronic wavefunction with respect to nuclear coordinates are small. PESs are commonly reported and discussed in the adiabatic representation as the symmetry of the state is conserved, and a single reactant electronic state can only connect to a single set of product electronic states. Adiabatic potentials of the same symmetry cannot cross and off-diagonal terms in the potential energy matrix linking different states are zero. The Born-Oppenheimer approximation breaks down when multiple PESs form an avoided crossing or conical intersection, i.e. approach degeneracy. By transforming into the diabatic representation, PESs that smoothly change with electronic configuration can be produced, however symmetry is not conserved.

1.4 Nonadiabatic coupling

In regions where electronic states approach degeneracy, the interactions between the states arising from nuclear kinetic energy becomes significant. i.e. non-Born-Oppenheimer behavior occurs. Landau and Zener independently modeled the probability of a nonadiabatic transition in a one-dimensional system by analyzing two intersecting diabatic potential curves.[6,7] The states are schematically shown in Figure 1-1, with the diabatic representation labeled ϕ, and the adiabatic state correlations labeled ψ. In a one-dimensional system adiabatic states of the same symmetry undergo an avoided crossing.
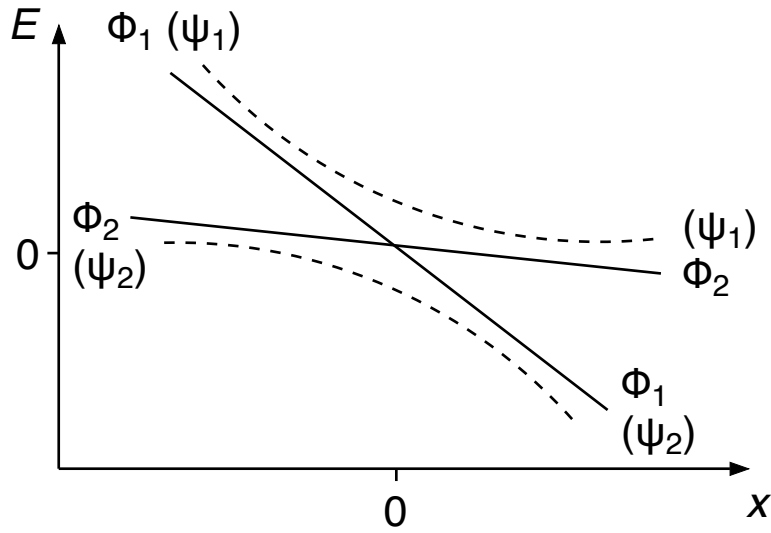
Figure 1-1. Potential energy curves for two intersecting states in one-dimension

The gradient of each slope and the coupling element in the diabatic basis H_{12} is assumed to change sufficient slow over the interaction region to be treated as a constant. The model assumes the energy separation between the two diabatic states (E_1 and E_2) changes linearly in time, and that all nuclear dynamics are classical. A modern derivation has been published by Wittig.[8]

The Landau-Zener formula for the probability of a nonadiabatic transition is given by

$$P = \exp(-2\pi\, \omega_{12}\, \tau_d) = \exp\left(\frac{-2\pi H_{12}^2}{\hbar v |E_2 - E_1|}\right)$$

At the intersection $\omega_{12} = |H_{12}|/\hbar$ corresponds to the frequency at which the system oscillates between the two diabats and $\tau_d = |H_{12}|/v|E_2 - E_1|$ gives the interaction duration,[9] with v the (constant) relative velocity and interaction 'length' $\propto |H_{12}|/|E_2 - E_1|$.

6

The Landau-Zener formula for the probability of a nonadiabatic transition is exact for a one-dimensional system. In a polyatomic molecule, a useful first approximation can be obtained if changes in the coupling strength are predominantly associated with a single coordinate.

In the adiabatic representation the potential energy matrix is diagonal, nonadiabatic coupling depends on nuclear momentum-like operators and is proportional to

$$\frac{\langle \Psi_2 | \boldsymbol{\nabla} \hat{H}_e(r, R) | \Psi_1 \rangle}{U_1 - U_2}$$

where Ψ denotes the adiabatic electronic wavefunction and U is the associated energy. The divergence $\boldsymbol{\nabla}$ is a vector operator. At a point of degeneracy the denominator $\rightarrow 0$ and the coupling diverges. Coupling in the diabatic representation arises from off-diagonal V_{12} terms in the potential energy matrix, while the nuclear kinetic energy matrix becomes diagonal. Potential-like operators are used to calculate the interstate coupling,

$$\left\langle \Phi_2 \left| \frac{\partial}{\partial R} \hat{H}_e(r, R) \right| \Phi_1 \right\rangle R$$

where Φ is the diabatic electronic wavefunction and R is a nuclear coordinate.[10,11]

Types of coupling that lead to the breakdown of the adiabatic approximation include: conical intersections, vibration, rotation and spin-orbit couplings.

1.4.1 Conical intersections

Multidimensional seams of conical intersection occur when two Born–Oppenheimer (adiabatic) nuclear potential energy surfaces are degenerate in energy. Two coordinates describe the intersection: the *tuning* coordinate that brings the two adiabatic states closer in energy *i.e.* V_{11} and V_{22} approach, while maintaining $V_{12} = 0$, and the *coupling* coordinate of non-totally symmetric motion that makes $V_{12} \neq 0$ in an avoided crossing. Motion in the remaining N-2 coordinates does not lift the degeneracy of the two adiabatic PESs, forming a seam of intersection. Figure 1-2 shows that when viewed from the tuning and coupling coordinates, the upper and lower adiabatic surfaces appear as two cones. Figure 1-2 highlights adiabatic pathways (solid arrows) and a non-adiabatic pathway that couples the two states (dashed arrow).[10]
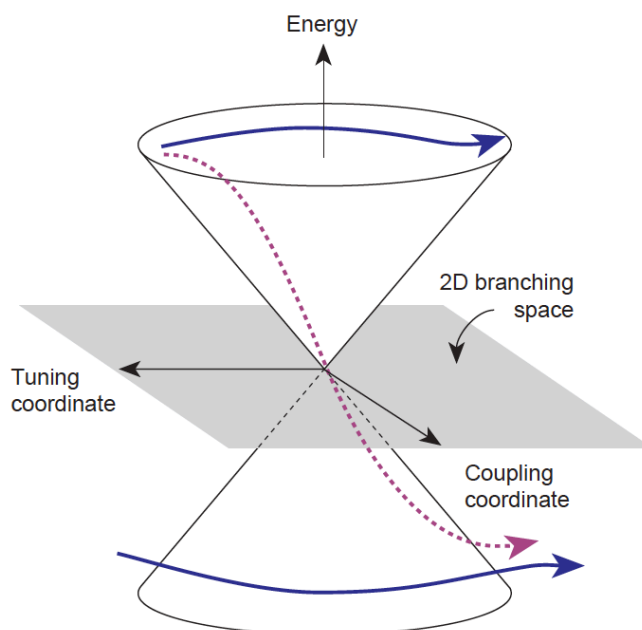
Figure 1-2. A schematic of a conical intersection between two adiabatic potential energy surfaces

Reproduced from Tutorials in Molecular Reaction Dynamics (RSC Publishing, 2012)

The requirement for a tuning and coupling coordinate to form a conical intersection highlights why the behavior of diatomic molecules differs to polyatomic molecules: the only available degree of freedom is extension of the bonding coordinate, a reduction in symmetry is not possible leading to the non-crossing rule for the electronic states of diatomic molecules.

1.4.1.1   Symmetry required

A molecule with a particular point group symmetry (e.g. C_{3v}) has states that are components of an irreducible representation that are required by symmetry to be degenerate (e.g. a pair of E states).[12]

"Although the Jahn-Teller theorem did not exist at that time, he [Lev Landau] told me about it… I disputed the idea…" [13]   – Edward Teller

The Jahn-Teller theorem states that a symmetric polyatomic molecule in a degenerate electronic state will distort to reduce symmetry, and holds for all molecules except those connected in a straight line.[13]

1.4.1.2   Accidental symmetry-allowed

A molecule can form an accidental symmetry-allowed intersection for two electronic states of distinct irreducible representation. An example would be a molecule with C_{2v} symmetry, that on deformation forms A_1 and B_2 states. All motions of symmetric displacement maintain C_{2v} symmetry and have $V_{12} = 0$, while $V_{11} = V_{22}$ is for satisfied accidentally only at specific nuclear coordinates.[14]

1.4.1.3 Accidental same-symmetry

The prevalence of same-symmetry accidental conical intersections was only recognized in the 1990s, and have since been implicated in a wealth of excited-state deactivation and/or fragmentation processes.[12] A key step in vision is the isomerization of the 11-cis retinal chromophore to the all-*trans* form, the remarkable efficiency and timescale of the photophysical process owes to a conical intersection.[15] The two specific motions that lift the degeneracy of the adiabatic PESs in a same-symmetry accidental conical intersection are not defined by symmetry, i.e. cannot be foreseen so require computation to locate.

1.4.2 Vibration induced coupling

Internal conversion (IC) can occur when vibrational motion induces coupling of electronic states. The coupling strength can be non-zero only if the product of the two electronic states symmetries and normal mode vibrational symmetry contains the totally symmetric representation. The rate of non-adiabatic transition from an initial bound electronic state i to an unbound final state f of the same multiplicity is given by Fermi's golden rule,[10]

$$P_{i \to f} = \frac{2\pi}{\hbar} \left| \langle f | \hat{T}_N | i \rangle \right|^2 \rho_f(\mathrm{E})$$

where $\hat{T}_N$ is the nuclear kinetic energy operator and $\rho_j(\mathrm{E})$ is the density of states, i.e. the number of states per unit energy.

Herzberg and Teller recognized that bending of a linear triatomic molecule in a degenerate

electronic state could break the degeneracy. Renner predicted the effect would manifest in vibrational bands of electronically degenerate states, as the vibrational and electronic motion couple. Renner-Teller coupling, as Herzberg named it,[16] leads to the breakdown of separable motions as are assumed in the Born-Oppenheimer approximation. The Renner-Teller effect is prominently displayed in the photochemistry of OCS, discussed later in this thesis. The effect was first observed in NH_2, where both the bent $^2B_1$ ground state and quasi-linear $^2A_1$ excited state correlate to the doubly degenerate linear $^2\Pi_u$. Dixon derived the Renner-Teller coupling strength to scale as $n^{-3/2}$, where n is proportional to the zero-order wavefunction overlap.[17] The magnitude of the exponent for the coupling is notably stronger than in the Landau-Zener case. The physical significance of this is that the Renner-Teller coupling quickly diminishes away from the symmetry required degeneracy.

1.4.3   Rotation induced coupling

Electronic states can couple by rotational motion of the nuclei, known as Coriolis coupling. Symmetry considerations determine if the coupling can be non-zero, most prominently states with different projections of electronic angular momentum on the internuclear axis (Ω) can become coupled by rotation.[18] The strength of rotational coupling is typically smaller than other types of coupling.

1.4.4   Spin-orbit induced coupling

Spin-orbit coupling can manifest in many ways including: electronic states of different symmetry may undergo electronic predissociation, molecules might undergo intersystem crossing (ISC) in

collision-free environment or photofragment branching may not follow adiabatic state correlations.

The non-relativistic Hamiltonian does not include the interaction of spin and orbital angular momenta of electrons. This may be a reasonable approximation for light atoms. In the case of hydrogenic atoms the energy levels can be calculated exactly, the magnitude of the coupling scales as $\hat{H}_{SO} \propto Z^4/n^3$, where Z is the atomic number and n is the principal quantum number. A general expression for the spin-orbit Hamiltonian is given by

$$\hat{H}_{SO} = A\ \hat{L}.\hat{S}$$

where A is the spin-orbit coupling constant, $\hat{L}$ is the total electronic orbital angular momentum operator and $\hat{S}$ is the total electronic spin angular momentum operator.

The importance of relativistic terms missing from the non-relativistic Hamiltonian can be illustrated by looking at different Hund's cases.[19] The cases represent situations where electrostatic, spin-orbit and rotation coupling take different strengths. The relativistic Hamiltonian includes only the former. Angular momenta for a diatomic are labeled **L** for the total electronic orbital angular momentum, **S** for the total electronic spin angular momentum, **J** for total angular momentum, **N** = **J** – **S** is the total spin-free angular momentum, and **R** = **N** – **L** for the rotational angular momentum of the nuclei.

Hund's case (a) is typical for a diatomic. *i.e.* spin-orbit coupling is intermediate. Figure 1-3 shows **L** coupled to the internuclear axis, giving the axial projection Λ and **S** spin-orbit coupling to **L**, with axial projection Σ. It is assumed that L and S remain coupled to the internuclear axis, giving Ω = Λ + Σ, finally **J** is the coupling of Ω to **R**.
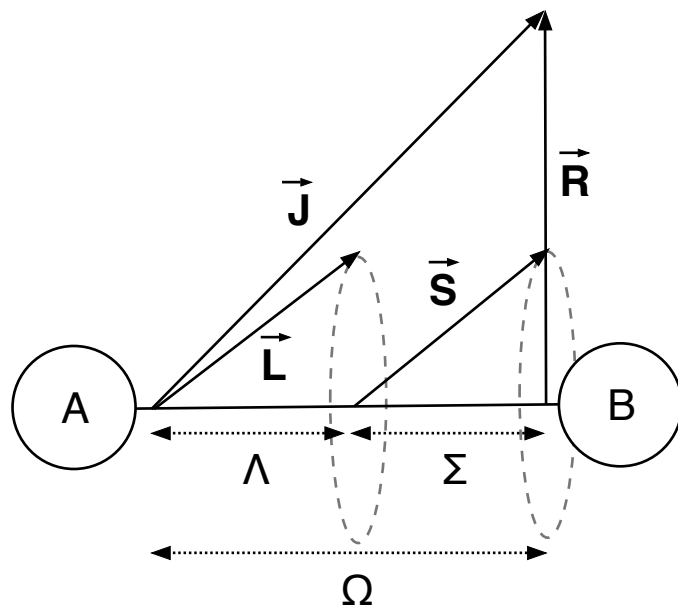
Figure 1-3. Angular momenta for Hund's case (a) in a diatomic molecule

If the spin-orbit coupling term dominates the electrostatic coupling, a situation often encountered with a heavy atom, then Hund's case (c) is most appropriate. **L** and **S** are not coupled to the internuclear axis and Λ and Σ cannot be defined. Ω is instead given by the axial projection of **L + S.**

Experimentally the Hund's cases are manifested in the energy level patterns observed in rotational spectroscopy. Another example, which will be utilized later in this thesis, is that spin-orbit coupling can cause the energy levels of atoms to split, providing a state-selective way to excite and detect atoms such as $S(^3P_J)$ or $I(^2P_J)$.

1.5 Franck-Condon principle

Franck noted that the mass of the nuclei in molecules is large compared to the mass of an electron, therefore the momentum of the nuclei is unchanged by an electronic transition.[20] The depth and displacement of two parabolas forming the ground and excited electronic states will determine the extent of vibration upon excitation.

Condon's paper, accepted *in lieu* of a PhD thesis, expanded on this idea.[20] Transitions that require the least adjustment of the position and momentum of the nuclei are favored. At the well minimum, the shape of potential can be approximated by the leading term

$$V(r) = \frac{1}{2}k(r - r_0)^2 + \cdots$$

where the force constant $k = (2\pi v)^2 \mu$, with the experimental vibrational frequency v, reduced mass μ and the moment of inertia determined by rotational spectroscopy can be used to find r_0. If a large structural rearrangement to reach the equilibrium geometry is required after excitation, r_0 will change, in other words the potentials are displaced and the Franck-Condon principle requires a large change in the vibrational quantum number.[21] Analysis of experimental electronic spectra of diatomic molecules supported this correlation.

Re-expressed in the language of quantum mechanics, the nuclear wavefunction remains unchanged during an electronic transition. A simultaneous vibrational and electronic (vibronic) transition from a state ψ to ψ' can be evaluated by separating the electronic and vibrational wavefunctions by means of the Born-Oppenheimer approximation,

$$\langle \psi_v{}'(R)\psi_e{}'(r,R)|\boldsymbol{\mu_e} + \boldsymbol{\mu_n}|\psi_v(R)\psi_e(r,R)\rangle$$

Where the electric dipole moment operator $\boldsymbol{\mu}$ is the sum over locations and charges of all electrons and nuclei. Applying the Condon approximation, $\langle \psi_e{}'(r,R)|\boldsymbol{\mu_e}|\psi_e(r,R)\rangle \sim$ constant, suggests the dominant term is the (Franck-Condon) overlap integral

$$S(v',v) = \langle \psi_v{}'(R)|\psi_v(R)\rangle$$

Invoking the Born interpretation of the wavefunction, the relative transition intensities are proportional to $|S(v',v)|^2$.

In 1930 repulsive potentials for molecular states had been predicted by quantum mechanical calculations, yet never directly observed. By reference to potential energy curves for molecular hydrogen, Bleakney tuned an electron source to 31.5 eV to access a repulsive state that correlates to $H + H^+ + e^-$. The asymptote was calculated to lie ~13 eV lower in energy than the Franck-Condon vertical excitation. Detection of the H^+ by mass spectrometry confirmed that H ions were formed with a kinetic energy of 6.5 eV, equivalent to a total energy release of 13 eV. A classical viewpoint of $H_2{}^+$ would allow only attractive interactions.[22]

1.6 Types of photodissociation

The work of Bleakney discussed above serves as an introduction to the topic of this thesis: dissociation. The experimental work carried out during my graduate studies uses light to initiate dissociation. Categories of molecular photodissociation mechanisms have emerged, based on the characteristics and interactions of PESs.

1.6.1 Direct

A photon excites a molecule from the ground state AB to an electronically excited state AB*, the excited state potential is repulsive and the molecule directly dissociates to products A + B. Figure 1-4 shows the change in potential energy $V(R_{AB})$ with extension of the distance between the two atoms, R_{AB}.
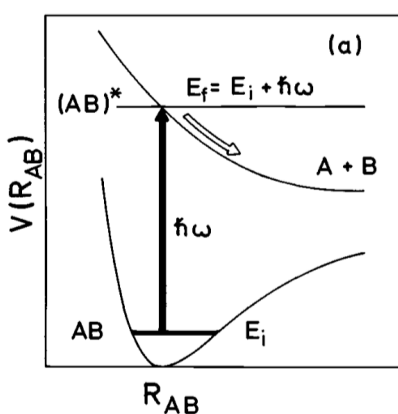
Figure 1-4. Schematic potential for direct photodissociation

Reproduced from Schinke, R. Photodissociation Dynamics: Spectroscopy and Fragmentation of Small Polyatomic Molecules. (Cambridge University Press, 1993).

1.6.2 Predissociation

Predissociation may occur after excitation to a bound electronically excited state. Two common types of predissociation are shown in Figure 1-5: (a) the bound state may electronically couple to a dissociative state by a radiationless transition (rt), or (b) may vibrationally predissociate by tunneling (tn) through the barrier or by internal energy redistribution (IVR) to pass over the barrier. Different vibrational levels of quasi-bound states in the well may be accessed with tunable excitation, the lifetime of which will depend on the coupling between the electronic states in electronic predissociation, and tunneling rate or IVR efficiency in the case of vibrational predissociaton.
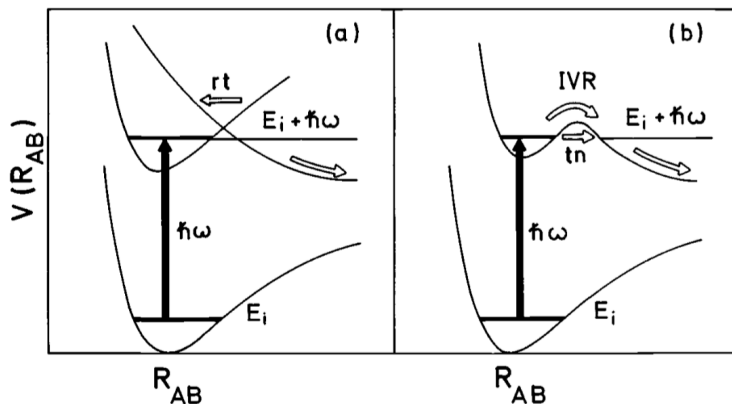
Figure 1-5. Schematic potential for (a) electronic and (b) vibrational predissociation

Reproduced from Schinke, R. Photodissociation Dynamics: Spectroscopy and Fragmentation of Small Polyatomic Molecules. (Cambridge University Press, 1993).

1.6.3 Unimolecular decomposition

Excitation occurs to a bound electronically excited state. This state may decay to the ground electronic state (S_0) by a radiationless transition as illustrated in Figure 1-6. The energy of the highly internally excited molecule lies above the bond dissociation threshold on S_0 so the bond can break.
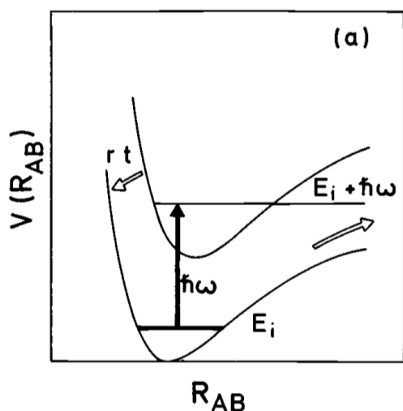
Figure 1-6. Schematic potential for unimolecular decomposition

Reproduced from Schinke, R. Photodissociation Dynamics: Spectroscopy and Fragmentation of Small Polyatomic Molecules. (Cambridge University Press, 1993).

1.7 Angular distributions

For an electronic excitation the Franck-Condon principle states the nuclear framework remains stationary. If a single electronic state is prepared and undergoes dissociatiion on a timescale that is rapid compared to the period of rotation, then the angular distribution of photofragments is defined by the initial orientation of the molecule.

Anisotropy in the angular distribution is given by averaging over the dot product of the transition dipole moment of the molecule and the electric vector of the light

$$\langle |\boldsymbol{\mu} \cdot \boldsymbol{\varepsilon}|^2 \rangle$$

Defining a nonrotating "space-fixed" laboratory frame (F) of coordinates XYZ and a set of rotating "molecule-fixed" (g) coordinates xyz, and fixing the electric vector $\boldsymbol{\varepsilon}$ of plane polarized light to be along Z. The simplest case for photodissociation will be introduced, where a diatomic molecule undergoes axial recoil and the two atoms separate along z.

For axial recoil of a diatomic,

$$\mu_x = \mu_y = 0; \ \mu_z \neq 0 \quad \text{for } \Delta\Omega = 0 \quad (\parallel \text{ transitions})$$

$$\mu_x = \mu_y \neq 0; \ \mu_z = 0 \quad \text{for } \Delta\Omega = \pm 1 \ (\perp \text{ transitions})$$
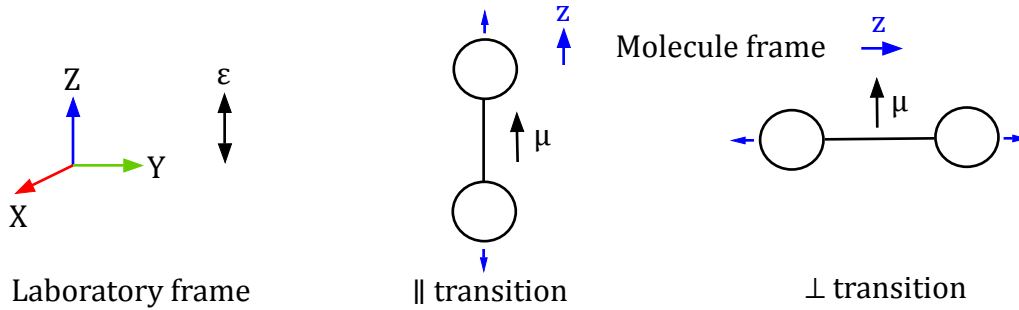
Figure 1-7. A molecule in the molecule-fixed frame (g) interacts with the electric vector $\boldsymbol{\varepsilon}$ aligned along Z in the laboratory frame (F). The transition dipole moment for a ∥ transition and ⊥ transition are shown.

Using the Eulerian angles ϕ, θ, ψ and defining ϕ as the polar angle between z and Z, θ as the polar angle between z and the XY plane, and ψ is the azimuthal angle about the z axis. The interaction of the transition dipole moment in the molecule frame with the electric vector of light in the laboratory frame can be related by an angle dependent coefficient $\Phi_{Fg}(\phi, \theta, \psi)$ that transforms between xyz and XYZ.

$$|\boldsymbol{\mu} \cdot \boldsymbol{\varepsilon}|^2 = \mu_g{}^2\, \varepsilon_F{}^2\, \left|\Phi_{Fg}(\phi, \theta, \psi)\right|^2$$

With the electric vector $\boldsymbol{\varepsilon}$ of plane polarized light to be along Z, the distributions are

$$I(x) = (1 + \beta P_2)\sin\theta \sin\phi$$

$$I(y) = (1 + \beta P_2)\sin\theta \cos\phi$$

$$I(z) = (1 + \beta P_2)\cos\theta$$

where $P_2(\cos\theta) = \frac{1}{2}(3\cos^2\theta - 1)$ is the second order Legendre polynomial and β parameterizes the anisotropy of the angular distribution.
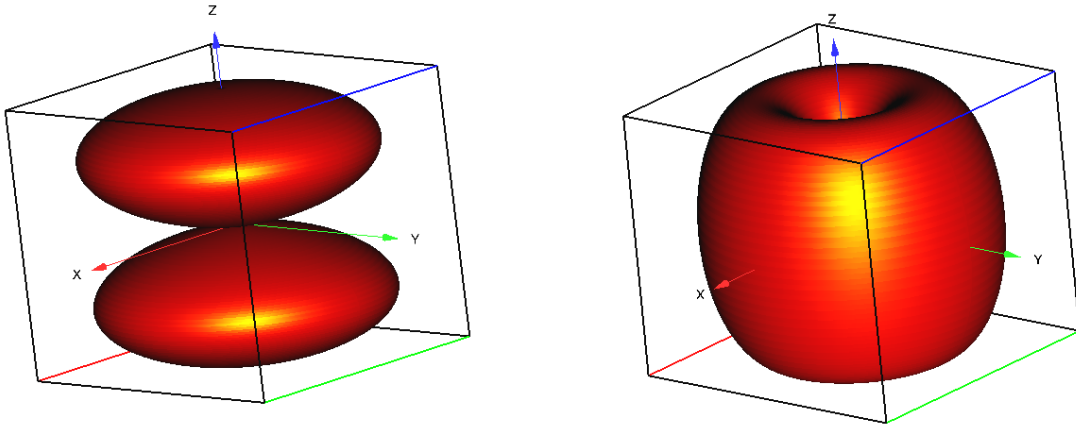
Figure 1-8. Three-dimensional Newton sphere for (a) ∥ transition, $\beta = +2$, and (b) ⊥ transition, $\beta = -1$.

Experimentally a 2D detector in the XZ plane observes the cylindrically symmetric distribution, averaging over the azimuthal angle

$$\frac{1}{2\pi}\left|\Phi_{Fg}(\phi,\theta,\psi)\right|^2 = \begin{cases} \cos^2\theta\,, & \mu = z & (\parallel \text{ transitions}) \\ \frac{1}{2}\sin^2\theta\,, & \mu = x,y & (\perp \text{ transitions}) \end{cases}$$

The result above emphasizes that fragments will take a spatial distribution of either $\cos^2\theta$ or $\sin^2\theta$ for axial recoil from parallel and perpendicular transitions, respectively.

A general expression for the angular distribution of the central slice of the three-dimensional photofragment distribution (Newton sphere) is then

$$I(\theta) = \frac{1}{4\pi}(1 + \beta P_2(\cos\theta))$$

20

Distributions that would be observed for a two-dimensional slice of the Newton sphere for purely $\parallel$ transition $\beta = +2$, $\perp$ transition $\beta = -1$, and $\beta = 0$ are shown in Figure 1-9 to illustrate characteristic distributions with the electric vector $\boldsymbol{\varepsilon}$ of plane polarized light aligned vertically.
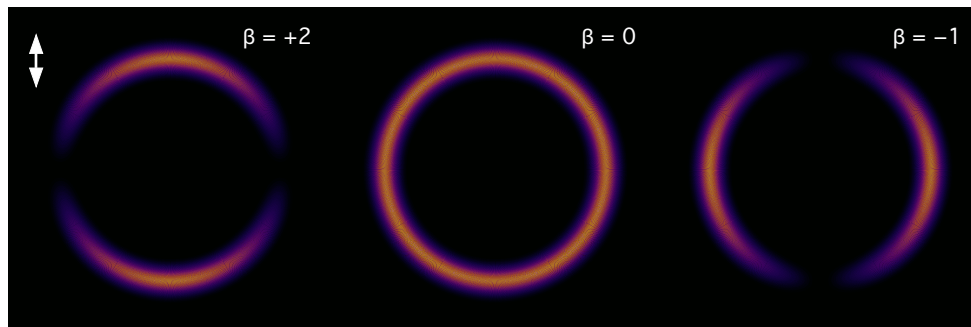
Figure 1-9. Two-dimensional slices through three-dimensional photofragment distributions

Deviation from the limiting cases of the anisotropy parameter occurs commonly in polyatomic molecules where the transition dipole moment is rotated away from the bond that will break. Alternative reasons the anisotropy parameter may be less than the limiting value includes excitation to multiple electronic states of mixed symmetry, deviation from axial recoil approximation and dissociation occurring on a timescale exceeding the period for molecular rotation.

1.8 Probing photodissociation products

This section discusses techniques that can be used to experimentally probe a potential energy surface. Specifically techniques that allow mass-resolved detection of photoproducts are introduced. Using laser light allows the process to be 'clocked' by using pump and probe pulses that are well defined in time. Wavelength tunable pulses can be used to initiate the dissociation from different electronic states, and allow products to be probed state-selectively, i.e. one electronic, vibrational or rotational state of a fragment.

1.8.1   Wiley-McLaren mass-spectrometry

Ions formed in an inhomogeneous electric field will be accelerated and reach a detector at a time that depends on their initial position and velocity. Setting the potential energy equal to the kinetic energy

$$qV = \frac{1}{2}mv^2$$

where q is the charge and V is the accelerating potential, m is the fragment mass and v the velocity. The time-of-flight t is found by rearrangement

$$t \propto D\sqrt{\frac{m}{qV}}$$

where D is the flight distance. This is illustrated in Figure 1-10a, where an ion created at t_0 in the region s is accelerated by the repeller electrode potential V_R, before entering a field free region D and striking the detector.

22
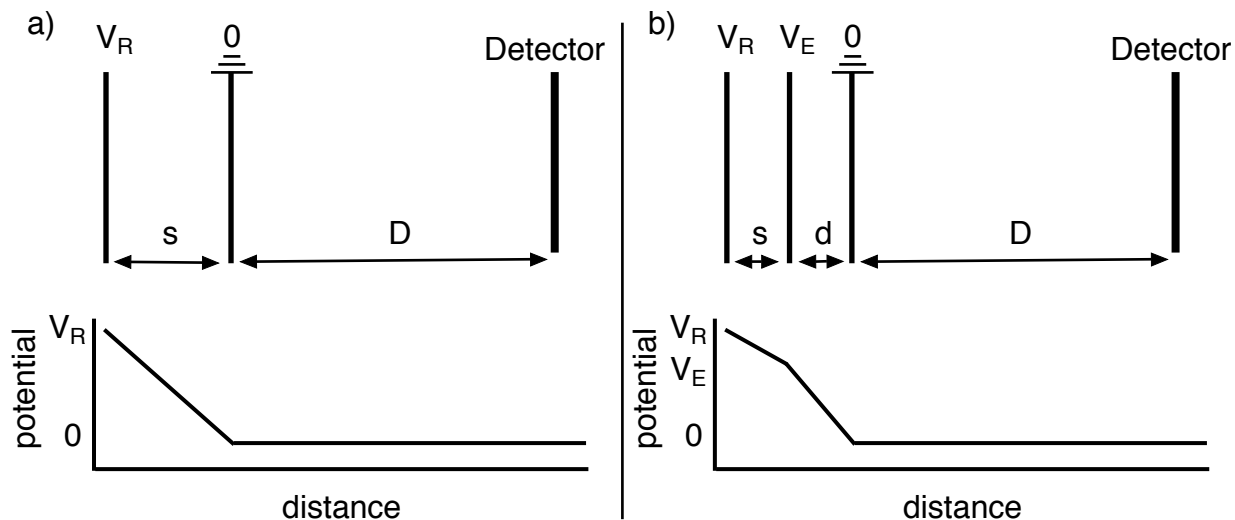
Figure 1-10. Schematic for time-of-flight mass spectrometer with a) one and b) two acceleration regions.

Wiley and McLaren noticed that two acceleration regions could make the arrival time independent of the initial position and velocity spread for all masses.[23] The Wiley-McLaren electrode configuration is illustrated in Figure 1-10b, where in the first acceleration region an ion starting further back from the detector or moving more slowly will spend longer in the acceleration region. This acceleration will make the ions catch up with those initially closer or moving more quickly, the distance at which the two converge is approximately given by[24]

$$D = 2sk^{\frac{3}{2}} - \frac{2dk}{\sqrt{k}+1}$$

where s and d are defined as the distance between the repeller – extractor and extractor – ground electrodes, respectively (see Figure 1-10b) and

$$k = \frac{sV_R + dV_E}{sV_R}$$

23

Note the expression is independent of fragment mass. The ratio of the potentials applied to the electrodes defines the focusing condition so that the whole mass-spectrum can be acquired in a single measurement. This decreases acquisition time and allows relative abundances to be studied. A single acceleration region can only resolve a narrow range of masses, necessitating multiple measurements at different accelerating potentials to collect the whole mass-spectrum.

1.8.2   Resonance-enhanced multiphoton ionization

A mass-spectrometer does not distinguish the quantum state of a fragment, just the mass to charge ratio. Resonance-enhanced multiphoton ionization (REMPI) is a technique that can preferentially ionize a fragment based on the quantum state. Resonance with a virtual state enhances the probability of absorption, and ultimately accessing the ionization continuum. The conventional notation is ($m+n$), where m denotes the number of photons to reach the virtual state, and n is the number of photons required to subsequently ionize. If the frequency of m and n are not same, i.e. two colors are used to achieve ionization, then a prime is added ($m+n'$). In Chapter 4 REMPI will be employed to ionize of $S(^1D)$ atoms via the $3p^34p$ $^1F_3$ level at 288.17 nm, whereas $S(^3P_J)$ atoms can be ionized via the $3p^34p$ ^3P_J levels at one-photon wavelengths near 308.20 nm, 310.09 nm and 310.96 nm, which probe the J = 2,1, and 0 levels, respectively.

1.8.3   H Rydberg atom photofragment translational spectroscopy

An alternative to ionization of fragments in a small spatial region is to 'tag' fragments by excitation to a Rydberg state. H Rydberg atom photofragment translational spectroscopy (HRA-PTS) is a technique developed to probe the translational energy of photolytically produced H atoms with

high resolution.[25] A two-photon double resonance scheme is used where excitation at 121.6 nm, the Lyman-α transition frequency, promotes an electron from a 1s to 2p orbital. A second laser at ~365 nm further excites the atom to a Rydberg state with high principle quantum number n~80. Tagged fragments fly through a field free time-of-flight region to a large charged particle detector, and are field ionized by the potential bias applied to the detector. A change in H atom velocity of ~0.3% can be resolved, this high resolution owes from minimizing the density of charged particles that would otherwise repel each other. Selective detection is achieved as the internal energy of untagged neutrals is insufficient to be field ionized, and further improved by applying a pulsed electric field to sweep any ions formed accidentally away from the detector. Advantages to detecting H atoms include: excess energy must reside in the co-fragment as no vibrational or rotational energy can be stored in an atom, and only a single probe scheme is required.

 H Rydberg atom photofragment translational spectroscopy (HRA-PTS) has been used to show that dissociation of imidazole, pyrrole and phenol populates only a very limited number of the accessible product vibrational states, incompatible with unimolecular decay on S_0 and confirming the role of $^1\pi\sigma^*$ states.[26] The non-radiative decay of imidazole, pyrrole and phenol chromophores in nucleobases and aromatic amino acids serves as a protective mechanism in biological systems.[26] Strong absorption in the UV is primarily associated with the $\pi^* \leftarrow \pi$ transition. The $\sigma^* \leftarrow \pi$ transition is accessible for imidazole and pyrrole, but is much weaker. Direct excitation or non-radiative transfer from the $^1\pi\pi^*$ state to the $^1\pi\sigma^*$ state and subsequent relaxation of the $^1\pi\sigma^*$ state by N-H / O-H bond extension was suggested to occur.[27] This provides an efficient non-radiative decay pathway by bond cleavage in the gas phase. The conventional wisdom was that a bound state such as the $^1\pi\pi^*$ state would undergo unimolecular decay by internal conversion to S_0, where the highly internally excited molecule would then eventually dissociate. Small molecule photochemistry helps to bridge the gap to understanding larger more complex biological species.

1.8.4 Ion imaging

The original implementation of ion imaging by Houston and Chandler combined time-of-flight mass spectrometry with two-dimensional detection, to obtain information on the spatial distribution of nascent photofragments.[28] Widespread adoption of ion imaging occurred after velocity focusing conditions of the electrodes were developed that enabled the nascent velocity of an ion regardless of initial position, to be mapped onto a detector.[29] A velocity map ion imaging (VMI) experiment can be described in four distinct stages: *creation–conversion–projection–recovery*.[30]

Creation starts with the introduction of a target species seeded in a noble gas (He, Ar, Xe) into a source chamber at high vacuum by a pulsed solenoid valve. Supersonic expansion results in rapid internal cooling and preparation of isolated gas phase molecules. The expansion is skimmed to sub-select those with the lowest velocity spread parallel to the detector face, forming a molecular beam with a temperature typically ~10 K. The beam passes into a differentially pumped ionization chamber, and is intersected perpendicularly by counter-propagating photolysis and probe laser beams (Figure 1-11)
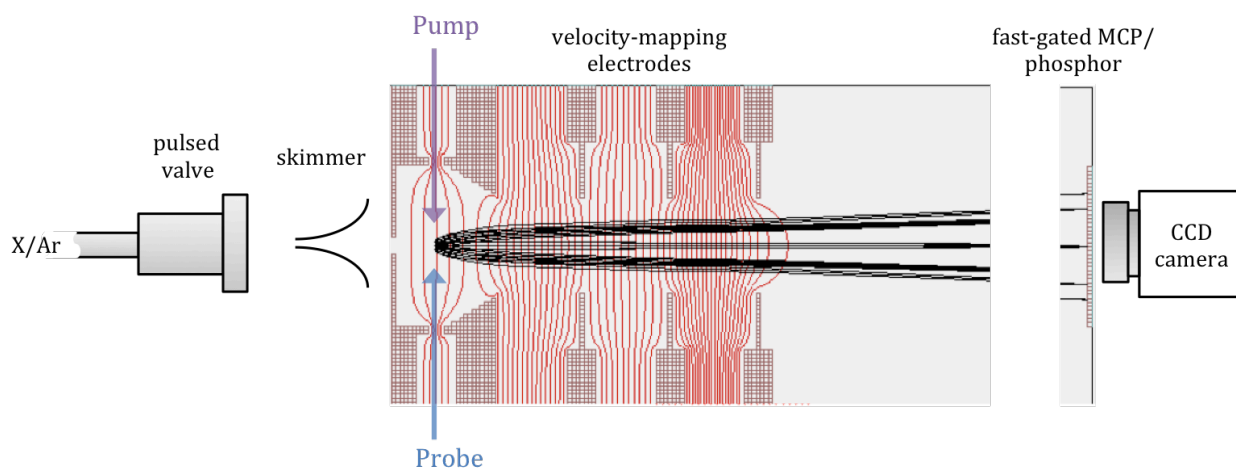
Figure 1-11. Velocity map imaging spectrometer schematic

Conversion is synonymous with probing nascent neutral photofragments by ionization, preferably with a state-selectively technique such as REMPI.

Projection uses an electrostatic lens assembly to guide charged species (analogous to an optical lens guiding light) to a position sensitive detector comprised of a multichannel plate (MCP)/Phosphor assembly in a third differentially pumped region. An ion strike produces a bright spot on the Phosphor screen that is captured by a CCD camera.

Simulated ion trajectories in Figure 1-12 are reproduced from A. Eppink and D. Parker, Rev. Sci. Instrum. 68 (9) 3477, **1997**. Equipotential surfaces are indicated. The ionization laser propagates along the y direction, intersecting the molecular beam propagating in the x direction. Ions can be formed in x and y multiple positions owing to the finite width of the molecular and laser beams. The velocity focusing conditions (mapping nascent velocity regardless of initial position) for ions with a large range of kinetic energy moving in any direction are desired.[31] At the focal plane ions with the same initial ejection angle but different initial positions coalesce.
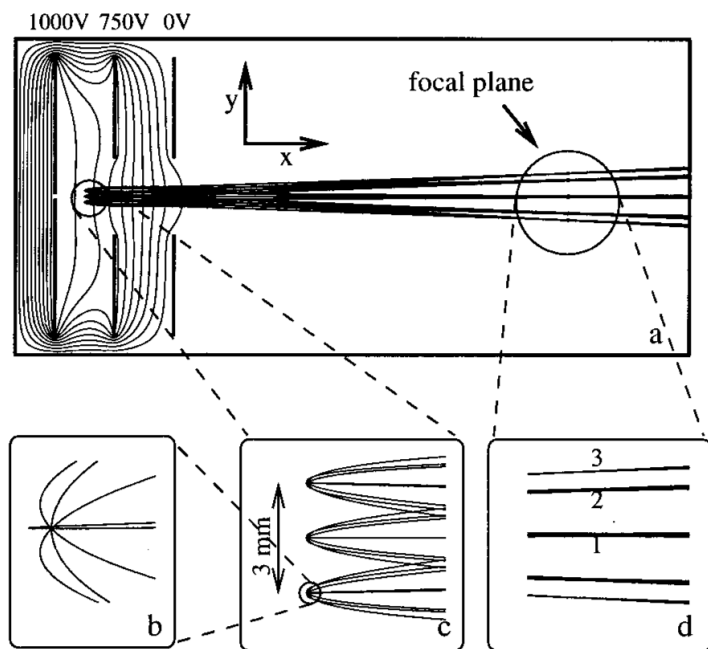
Figure 1-12. Simulated ion trajectories for velocity map imaging electrodes

Reproduced from A. Eppink and D. Parker, Rev. Sci. Instrum. 68 (9) 3477, **1997**

Recovery. In the original implementation by Eppink & Parker the Newton sphere is temporally collapsed (pancaked) onto the detector, and must be retrieved by inversion methods such as an Abel inversion or Polar Onion Peeling[32] to select only the central slice of the three-dimensional Newton sphere. This method requires cylindrical symmetry of the system, and so restricts possible combinations of photolysis and probe laser polarizations, as well as introducing noise in the image.

1.8.4.1   Slicing imaging

An alternative to temporal collapse of the Newton sphere is temporal expansion. The challenge lies in achieving sufficient expansion without loss of velocity mapping resolution. Techniques based around expansion are typically termed slicing, as the central slice of the Newton sphere can be

directly obtained by gating the active time of the position sensitive detector, obviating then need for

inversion algorithms to process the acquired image. The speed and angular distributions of sliced

ion images can be determined by integration of the image.[30]

1.9 **References**

1. Griffiths, D. J. *Introduction to quantum mechanics*. (Pearson Prentice Hall, 2005).
2. Atkins, P. W. & Friedman, R. *Molecular quantum mechanics*. (Oxford University Press, 2011).
3. Car, R. & Parrinello, M. Unified Approach for Molecular Dynamics and Density-Functional Theory. *Phys. Rev. Lett.* **55,** 2471–2474 (1985).
4. Öhrn, Y. & Deumens, E. Toward an ab Initio Treatment of the Time-Dependent Schrödinger Equation of Molecular Systems. *The Journal of Physical Chemistry A* **103,** 9545–9551 (1999).
5. Schinke, R. *Photodissociation Dynamics: Spectroscopy and Fragmentation of Small Polyatomic Molecules*. (Cambridge University Press, 1993).
6. Landau, L. D. Zur theorie der energieubertragung. II. *Physics of the Soviet Union* **2,** 46–51 (1932).
7. Zener, C. Non-Adiabatic Crossing of Energy Levels. *Proceedings of the Royal Society of London A: Mathematical, Physical and Engineering Sciences* **137,** 696–702 (1932).
8. Wittig, C. The Landau–Zener Formula †. *The Journal of Physical Chemistry B* **109,** 8428–8430 (2005).
9. Chichinin, A. I. Comment on 'The Landau–Zener Formula'. *J. Phys. Chem. B* **117,** 6018–6018 (2013).
10. Brouard, M., Vallance, C. & Royal Society of Chemistry (Great Britain). *Tutorials in Molecular Reaction Dynamics*. (RSC Publishing, 2012).
11. Farag, M. H., Jansen, T. L. C. & Knoester, J. Probing the Interstate Coupling near a Conical Intersection by Optical Spectroscopy. *J. Phys. Chem. Lett.* **7,** 3328–3334 (2016).
12. Domcke, W. & Yarkony, D. R. Role of Conical Intersections in Molecular Spectroscopy and Photoinduced Chemical Dynamics. *Annu. Rev. Phys. Chem.* **63,** 325–352 (2012).
13. Teller, E. The Jahn-Teller effect — Its history and applicability. *Physica A: Statistical Mechanics and its Applications* **114,** 14–18 (1982).
14. Zhu, X. & Yarkony, D. R. Non-adiabaticity: the importance of conical intersections. *Molecular Physics* **114,** 1983–2013 (2016).
15. Polli, D. *et al.* Conical intersection dynamics of the primary photoisomerization event in vision. *Nature* **467,** 440–443 (2010).
16. Gerhard Herzberg. *Molecular Spectra & Molecular Structure III. Electronic Spectra and Electronic Structure Polyatomic Molecules*. (1966).
17. Dixon, R. N. The role of inter-state Renner-Teller coupling in the dissociation of triatomic molecules. *Molecular Physics* **54,** 333–350 (1985).
18. Rose, R. A. Ph.D. Thesis. Velocity Map Imaging of Photodissociation and Reaction Dynamics. (2010).
19. Herzberg, G. *Molecular Spectra and Molecular Structure I. Spectra of Diatomic Molecules*. (1963).
20. Condon, E. A Theory of Intensity Distribution in Band Systems. *Phys. Rev.* **28,** 1182–1201

(1926).

21. Condon, E. U. The Franck-Condon Principle and Related Topics. *American Journal of Physics* **15,** 365–374 (1947).

22. Bleakney, W. The Ionization of Hydrogen by Single Electron Impact. *Phys. Rev.* **35,** 1180–1186 (1930).

23. Wiley, W. C. & McLaren, I. H. Time-of-Flight Mass Spectrometer with Improved Resolution. *Review of Scientific Instruments* **26,** 1150–1157 (1955).

24. Chatterley, A. Ph.D. Thesis. Probing Nonadiabatic Dynamics in Isolated Molecules with Ultrafast Velocity Map Imaging. (2013).

25. Schnieder, L., Meier, W., Welge, K. H., Ashfold, M. N. R. & Western, C. M. Photodissociation dynamics of H2S at 121.6 nm and a determination of the potential energy function of SH(A 2Σ+). *The Journal of Chemical Physics* **92,** 7027–7037 (1990).

26. Ashfold, M. N. R., Cronin, B., Devine, A. L., Dixon, R. N. & Nix, M. G. D. The Role of πσ* Excited States in the Photodissociation of Heteroaromatic Molecules. *Science* **312,** 1637–1640 (2006).

27. Sobolewski, A. L., Domcke, W., Dedonder-Lardeux, C. & Jouvet, C. Excited-state hydrogen detachment and hydrogen transfer driven by repulsive 1πσ* states: A new paradigm for nonradiative decay in aromatic biomolecules. *Phys. Chem. Chem. Phys.* **4,** 1093–1100 (2002).

28. Chandler, D. W. & Houston, P. L. Two-dimensional imaging of state-selected photodissociation products detected by multiphoton ionization. *The Journal of Chemical Physics* **87,** 1445–1447 (1987).

29. Eppink, A. T. J. B. & Parker, D. H. Velocity map imaging of ions and electrons using electrostatic lenses: Application in photoelectron and photofragment ion imaging of molecular oxygen. *Review of Scientific Instruments* **68,** 3477–3484 (1997).

30. Ashfold, M. N. R. *et al.* Imaging the dynamics of gas phase reactions. *Phys. Chem. Chem. Phys.* **8,** 26–53 (2006).

31. Wrede, E. *et al.* Continuum state spectroscopy: A high resolution ion imaging study of IBr photolysis in the wavelength range 440–685 nm. *The Journal of Chemical Physics* **114,** 2629–2646 (2001).

32. Roberts, G. M., Nixon, J. L., Lecointre, J., Wrede, E. & Verlet, J. R. R. Toward real-time charged-particle image reconstruction using polar onion-peeling. *Review of Scientific Instruments* **80,** 053104 (2009).

2   Experimental

2.1   Velocity map imaging spectrometer

A new velocity map imaging (VMI) spectrometer has been designed, constructed and calibrated. VMI is a variant of time-of-flight mass spectrometry that incorporates a position sensitive ion detector to allow measurement of photofragment velocities.[1,2] The spectrometer consists of three differentially pumped high vacuum regions: source, ionization and drift/detection. Each chamber is evacuated by oil-free turbomolecular and roots pumps. A supersonic gas expansion in the source region is skimmed to produce a molecular beam with a temperature of < 30 K.[3] The molecular beam is carefully aligned into the center of an electrode stack contained inside the ionization chamber, where two independently tunable lasers are used to pump and probe the dissociation process. The electrode stack extracts ions to a position sensitive detector.

Figure 2-1 shows a refined electrode from a design reported in the literature[4] incorporating a conical extraction lens to shield the interaction region from stray fields.[5] Polyether ether ketone (PEEK) was used to mount each electrode, as it is: electrically insulating, rigid, not prone to shattering, readily machined into custom shapes and high vacuum compatible. The entire electrode assembly is removable as a single piece, dowel alignment pins ensure the assembly can be remounted and consistently return to the same position. The electric fields used to extract ions are specific to the experiment and electrode geometry. Simulation in SIMION was used to solve the Laplace equation and determine the electric fields.[6] Iterative optimization of electrode geometry and voltages was performed with the objective of maintaining velocity-mapping conditions for ions created with a broad range of initial positions, velocities and masses. The extended time-of-flight length of 620 mm in our apparatus, compared to the original design of 260 mm, requires a greater electrostatic field gradient to maintain spatial mapping onto the 40 mm diameter detector, and

results in modest temporal compression of the Newton sphere. From left to right Figure 2-1 depicts regions held at a potential of: ground (red), $V_{repeller}$ 2000 V (pink), $V_{extractor}$ 1760 V (green), V_{lens1} 1420V (blue), V_{lens2} 800 V (purple), ground (red), ground (red) and a photograph of the final assembled electrodes.

Figure 2-1. Velocity map imaging electrodes incorporating conical extractor design

Position sensitive detection is achieved by an assembly of two chevron stacked multichannel plates (MCPs) operating with a large potential bias across each plate so that an impinging ion creates a cascade of electrons, with a typical gain ∼10^6. In turn, the electrons strike a fast phosphor screen (P46, λ_{peak} = 530 nm, characteristic decay time ∼300 ns) resulting in an illuminated spot that is recorded by a CCD camera and transferred in real time to a data acquisition PC for analysis by event counting software. The camera shutter is slow, so acts to integrate all ions that arrive in the mass spectrum over a period of ∼20 μs. Time-of-flight mass spectrometry may be performed using a fast photon detector, such as a photomultiplier tube (PMT) or silicon photomultiplier (SPM) connected to an oscilloscope. Retrieving the central slice of a single fragment in the mass spectrum by direct current (DC) slicing[7] requires fast high voltage switching of the MCP stack from an inactive to active state. The MCPs are pulsed from low gain ∼1300 V to high gain ∼1800 V and back with a very short

(<30 ns) high voltage offset module (Photek GM-MCP, 9 ns minimum, +500 V, up to 1 kHz repetition rate). A pulse generator controls the timing of each component of the experiment (Quantum Composers 9520).

2.2 Continuum Horizon Optical Parametric Oscillator (OPO)

A broadly tunable mid-band optical parametric oscillator (Continuum Horizon II) pumped by a Nd:YAG (Continuum Surelite EX, 10 Hz, 3-5 ns, 220 mJ at 355 nm) can output radiation between 190-2750 nm with a linewidth of 3-7 cm^{-1} and minimum step size of 0.01 nm.

An OPO achieves optical gain by parametrically amplifying light at signal and idler frequencies (ω), at the expense of the pump frequency, by utilizing a medium whose polarization $\hat{P}(t)$ responds nonlinearly to the electric field of light $\hat{E}(t)$.[8]

$$\hat{P}(t) = \epsilon_0 \left(\chi^{(1)}\hat{E}(t) + \chi^{(2)}\hat{E}^2(t) + \cdots \right)$$

Where ϵ_0 is the permittivity of free space and $\chi^{(2)}$ is the second-order nonlinear optical susceptibility. Conservation of energy requires

$$\omega_{pump} = \omega_{signal} + \omega_{idler}$$

The nonlinear crystal allows for birifringent phase matching, so that conservation of momentum (k) can be satisfied

$$k_{pump} = k_{signal} + k_{idler}$$

The Horizon OPO optical layout is shown in Figure 2-2, two nonlinear crystals (Type-II BBO) are used in the oscillator cavity. Angular adjustment of the nonlinear crystals satisfies the phase matching condition, allowing control over the signal and idler frequencies produced. The design implements aspects described in US Patent 5,781,571 to construct a cavity resonant at the signal frequency. The pump is injected into the cavity by a notch mirror (HR 355, HT > 355), and counter-propagated. Care must be taken to control the pump intensity with resonant cavity designs, as resonant feedback amplifies the signal and/or idler frequency below peak output, and the parasitic reverse process dominates above the peak output. Therefore the output is strongly dependent on the pump intensity. A Porro prism acts a retroreflector and is used to terminate one end of the cavity; the narrow acceptance angle ensures that the angle-space for gain over multiple passes of the cavity is restricted. Combining the Porro prism with a Type-II BBO crystal results in a narrow beam divergence and spectral linewidth.
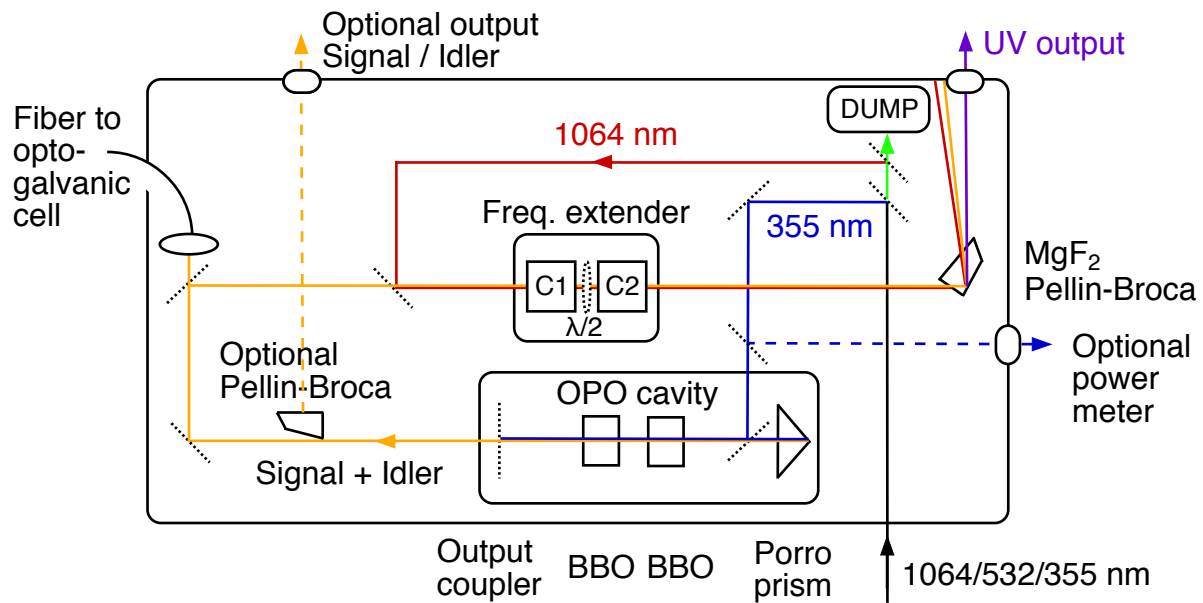
Figure 2-2. Horizon optical parametric oscillator layout

The Horizon signal output (400-700 nm) is extended into the UV by mixing, doubling or mixing

after doubling depending on the wavelength range required.

Table 2-1. Horizon output wavelength range and non-linear process

Wavelength (nm)	Process
190-208 (DUV)	Mixing after doubling (MAD) SHG of signal in C1, $\lambda/2$, then mixed with 1064 nm in C2.
208-235	SHG of signal in C2 (Type-I BBO 43.5°)
235-292	SHG of signal in C1 (Type-I BBO 64.3°)
292-400	Mixing of 1064 nm + signal
400-700	Signal OPO
700-2750	Idler OPO

Operation of the OPO requires calibration of the two BBO crystals in the oscillator cavity, and the two extra BBO crystals for UV generation. Due to the resonant cavity design it is critical that the 355 nm pump energy is stable, greater than 200 mJ but does not exceed 220 mJ. The angle of the first BBO crystal defines the wavelength; and the gain of the output is optimized by angle tuning the second crystal. During calibration a spectrometer (Ocean Optics USB2000, ±1 nm) is used to feedback the wavelength to the Horizon software. A lookup table is constructed for motor positions appropriate for the requested wavelength. When $\lambda > 400$ nm is desired, a pellin-broca prism separates the signal, idler and residual pump, and directs the output through the port labeled signal/idler. For $\lambda < 400$ nm, the pellin-broca is rotated out of the beam path, and two fixed 90° prisms direct the signal beam into two further BBO crystals. For near-UV generation, a notch mirror (HR IR, HT visible) combines the signal and 1064 nm in a BBO crystal. For UV generation, one of the two BBO crystals with the most appropriate cut angle is tuned. For DUV generation the signal is first doubled, then rotated by $\lambda/2$ by a manually inserted waveplate, and mixed with 1064

nm in the second BBO crystal. The output is resolved into constituent colors by a second pellin-broca (MgF_2) prism and exits via the port labeled UV. DUV generation requires optimal doubling is achieved prior to mixing, this can be visually inspected after separation by the pellin-broca with appropriate eye protection. Near-achromatic beam pointing stability can be achieved by calibration of the prism position in the far field. Small intervals in the motor position calibration of the four BBO crystals improve the absolute energy output, but may impact the smoothness of the energy output as a function of wavelength during scanning.

Two different techniques have been employed to verify the absolute UV wavelength calibration of the OPO. Recalibration of the optimal crystal positions oscillator in the OPO necessitates wavelength calibration is repeated.

1. An optogalvanic Ne spectra are measured from the voltage change in a filament bulb held at constant current upon resonant excitation of Ne atoms by incident light. An optical fiber captures a portion of the signal beam and is directed to a optogalvanic cell (Lambda Physik, 10 mA). The voltage response was monitored while scanning the OPO wavelength between 208-260 nm using an oscilloscope interfaced to a PC. Labview was used to integrate the optogalvanic cell response for the first microsecond after the laser pulse. A small wavelength offset of ~-0.14 nm provided satisfactory agreement with known line positions in PGOPHER.[9] The standard deviation between the observed and reference line positions is < 3 cm^{-1}, indicating the OPO is capable of good scanning linearity.

2. Halogens such as Br and I have many accessible resonantly enhanced multiphoton ionization schemes, the atomic line positions are accurately known and tabulated. The mass-spectrometer can be used to study a molecule containing a halogen in a one-color

experiment. A prerequisite is that the molecule can be dissociated by the same wavelength as the ionization scheme excitation wavelength.

2.3 Lambda Physik dye laser

The process of converting nascent photofragments into ions is preferably state-selective to enable fragments with the same mass to be distinguished e.g. $S(^3P_{2,1,0})$. Resonant-enhanced ionization achieves this aim, but requires tunable, intense and ideally narrow linewidth light. The second or third harmonic of a Nd:YAG (Continuum Surelite II-10) has been used to pump a dye laser (Lambda Physik Scanmate 2E) to produce visible light. The wavelength of the dye laser is controlled by the angle of a diffraction grating; this ensures narrow linewidth < 0.1 cm^{-1} and small scan step increments (0.002 nm) can be achieved, enabling high-resolution spectroscopy studies. Second harmonic generation produces UV between 205-350 nm.

2.4 Vacuum ultraviolet (VUV) generation

An alternative scheme for detection of nascent fragments is single photon VUV ionization. Third harmonic generation in a phase-matched mixture of Argon and Xenon of the frequency tripled output of a Nd:YAG is utilized to generate 118.2 nm (VUV) irradiation.[10–14] Many molecules and fragments have an ionization potential less than VUV photon energy of 10.49 eV, leading to the moniker (near) universal ionization.

Geometric ray tracing calculations were performed and are schematically shown in Figure 2-3 that achieve focusing of the VUV in the probe interaction region and re-collimation of UV incident light to be coupled out of vacuum chamber. The frequency tripled output of a Nd:YAG (Continuum

Surelite II-10) is focused near the midpoint of a home built gas cell (length 570 mm) containing an Argon/Xenon mixture by a plano-convex UV fused silica lens (focal length f = 502 mm) generating 118.2 nm light. A second lens separates the gas cell from the ionization chamber, held at pressures of 80 torr and 1×10^{-7} torr, respectively. The second lens is plano-convex and constructed from magnesium fluoride (Thorlabs f = 200 mm R_2 = 75.4 mm) to allow the VUV to be transmitted. The difference in refractive index is used to focus the VUV into the probe region (257 mm after the lens) while re-collimating the residual 355 nm to minimize unwanted multiphoton effects (R ~1.386 at 355 nm and ~1.68 at 118.2 nm).
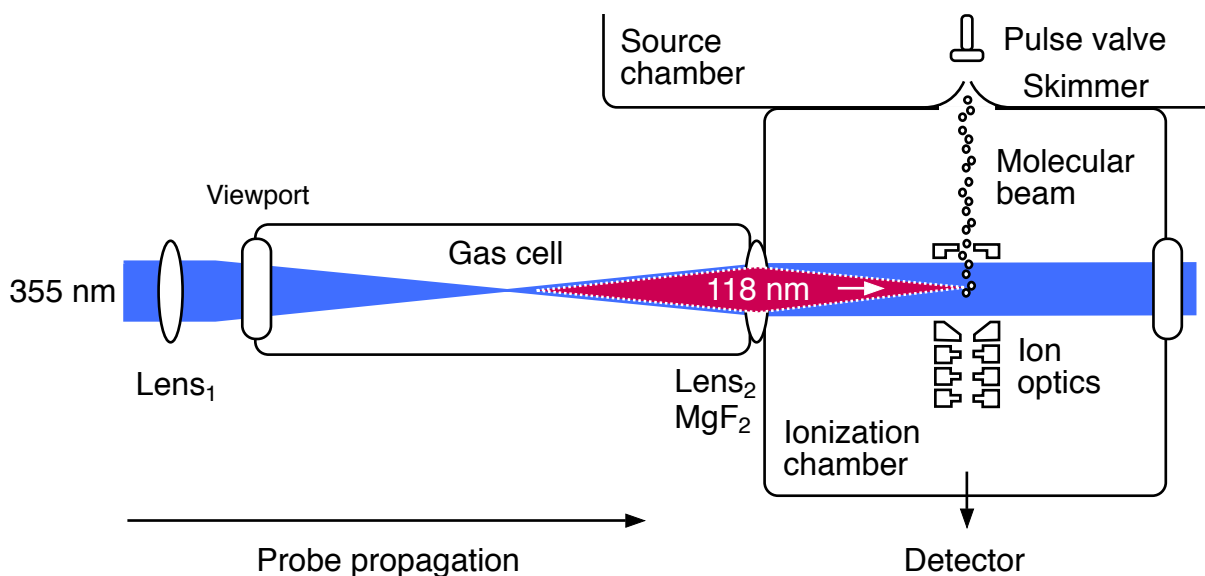
Figure 2-3. Schematic of geometric ray tracing calculations for VUV generation

The VUV stability was monitored by ionization of CH_2I_2 seeded in Argon (IP = 9.46 ± 0.02 eV). Iterative optimization of the mixture composition and total pressure with < 20 mJ of 355 nm pump led to a Argon/Xenon mixture of 10.06:1 at 80 Torr. Preparation of a large quantity of the mixture in a gas cylinder and allowing 12 hours to ensure uniform mixing dramatically improved reproducibility.

2.5 Data acquisition

This section presents the chronological pseudocode for experimental data acquisition. The code was developed in Labview® 2013.

(1) Initialize

- Verify communication to devices

- Configure oscilloscope channels

(2) Set multiple oscilloscope integration gates

- Mass peaks from silicon photomultiplier

- Pump and probe power from photodiode

(3) Cycle

- Define number of iterations experiment to run

    (4) Loop. Step through list of discrete values for:

    - Pump wavelength or toggle on/off

    - Probe wavelength or toggle on/off

    - Delay pump-to-probe

    - Delay gas valve

    - Delay detector slice

    - Motorized delay line (picosecond)

        (5) Scan. From start to end in incremental steps for:

        - Any device (as described above in loop)

            (6) Acquire for number of shots / scan step

            - Camera

            - Oscilloscope

(7) Analyze

• Camera event count and centroid

• Integrate oscilloscope gates

Data acquired during an experiment are assigned into arrays for each acquisition device:

Oscilloscope_array[cycle, loop, scan step, channel, gate, value]

Camera_array[loop, X value, Y value]

The oscilloscope (Teledyne Lecroy HDO 4054) has 4 channels (C1-4), as well as math (M1-2) and custom functions (F1-X) that may be transferred to the PC for post-processing. A multi-line string in Labview® is used to request data e.g. C1; C2. Oscilloscope data is integrated for the number of laser shots then analyzed on the fly for each active channel, gate and loop to display the average value and standard deviation for every scan step. Data acquired from the camera are integrated over both cycle and scan step, to reduce memory requirements of the program. A list of values may be entered into the loop menu if multiple ion images are desired.

2.6 Ion image analysis

During an experiment ions that strike a position sensitive detector are captured by a camera and are digitized to make images. The electric fields in the spectrometer ensure that the nascent velocity of ions is mapped into a position on the detector, irrespective of initial position. A fast gate applied to the detector ensures only the central slice of the three dimensional spatial distribution (sphere) is detected for a single mass. The displacement of the ion from the center of the image is proportional to its speed. Images are recorded as $I(x, y)$, and after defining a center point, the image can be represented in polar coordinates $I(r, \theta)$.
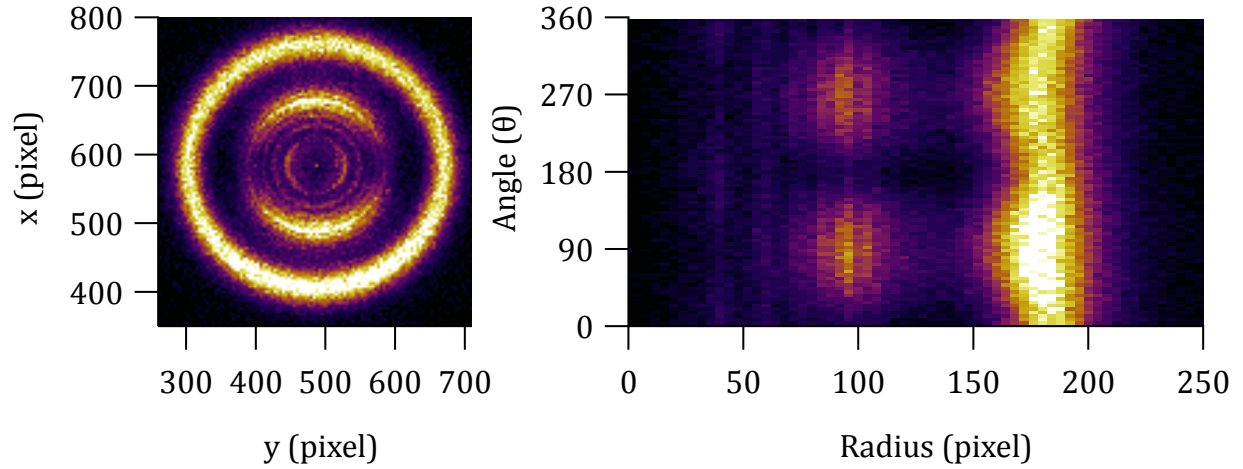
Figure 2-4. Ion image $I(x, y)$ transformation into polar coordinates $I(r, \theta)$

Integration over the angular coordinate, θ, and weighting by the Jacobian for a two dimensional slice of a three dimensional sphere gives the population distribution, $P(r)$ at each radial displacement, r.[15]

$$P(r) = \int I(r, \theta)\, r \sin \theta\, d\theta$$

While the angular distribution at each radial displacement is characterized by the anisotropy parameter β by fitting

$$I(r, \theta) = \frac{\beta_0(r)}{4\pi} \left(1 + \beta(r) P_2(\cos \theta)\right)$$

where β implicitly refers to β_2 the second order anisotropy parameter, P_2 is the second order Legendre polynomial and θ is the polar angle. By fitting each quadrant of an ion image individually, we obtained a more reliable determination of β and an uncertainty $\sigma(\beta)$ in the fit.

41

Figure 2-5 shows (a) a polar representation of an ion image that is converted to (b) a population distribution P(r) and (c) the anisotropy parameter β characterizing angular distribution. All code to analyze ion images was developed in Igor Pro (WaveMetrics, Inc., Lake Oswego, OR, USA) and is available in the Appendix.
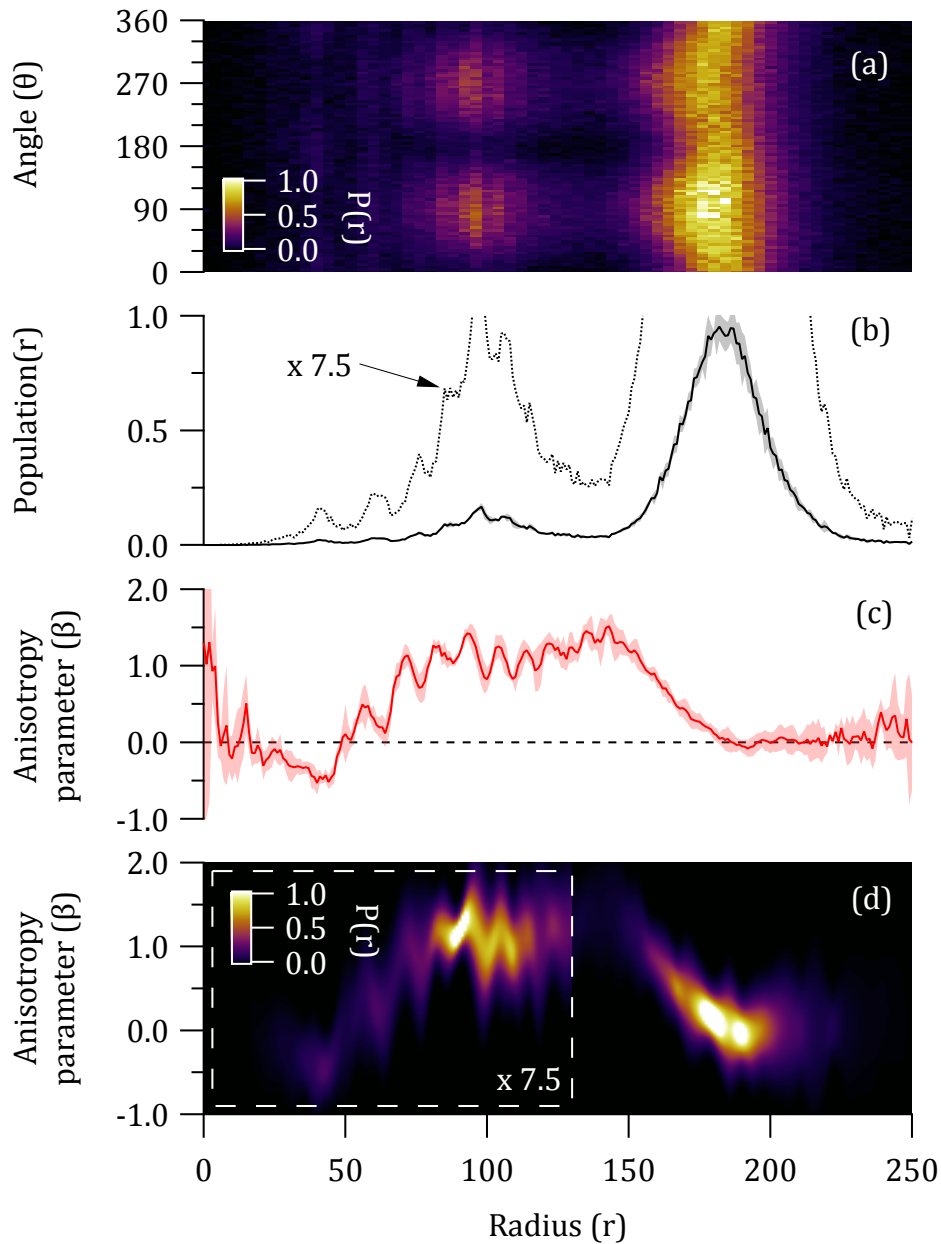
Figure 2-5. (a) Polar representation of an ion image $I(r, \theta)$, (b) population distribution P(r), (c) anisotropy parameter β characterizing angular distribution and (d) parameterized representation of ion image $I(r, \beta)$.

Photofragment speeds, v, are related to the image radius, r (in pixels), by the following equation:

$$v = \frac{Nr}{t}$$

where N is a calibration factor that must be determined empirically, and t is the flight time of the detected photofragment. The calibration factor depends on the electrode accelerating voltages, the camera distance from the phosphor screen, the camera lens, and whether super-resolution techniques are employed. The center-of-mass (centroiding) of each ion strike is calculated in Labview®, allowing the position to be determined with sub-pixel accuracy. Presently this is used to upscale the image resolution from the native camera 512x512 to 1024x1024 pixels.

The total translational energy E_T after photolysis is the sum of the translational energy of the fragments

$$E_T = \frac{p_{\text{ion}}^2}{2\,m_{\text{ion}}} + \frac{p_{\text{co-fragment}}^2}{2\,m_{\text{co-fragment}}}$$

where momentum $p = mv$. If the molecule dissociates into just two fragments, conservation of momentum between the two fragments allows the substitution

$$E_T = \frac{p_{\text{ion}}^2}{2\,m_{\text{ion}}} + \frac{p_{\text{ion}}^2}{2\,m_{\text{co-fragment}}}$$

Simplifying and switching to atomic mass units and energy in eV leads to

$$E_T = \frac{1}{2} m_{\text{ion}} v^2 \left(1 + \frac{m_{\text{ion}}}{m_{\text{co-fragment}}} \right) \frac{u}{eV}$$

Where E_T is the total kinetic energy released (TKER) in eV, m is the mass in atomic mass units, $u = 1.660539040(20) \times 10^{-27}$ kg and $eV = 1.602176565(35) \times 10^{-19}$ J. The mass of the co-fragment must be assumed to find the total translational energy. The script for processing experimental data uses a lookup table with the syntax "ion-cofragment", for instance, requesting "S-co" automatically passes $t = 5.7032$, $N = 38.75$, $m_{\text{ion}} = 32.07$ and $m_{\text{co-fragment}} = 28.05$. A similar lookup table allows the units to be selected between "eV" or "cm-1". Normalizing the resulting translational energy population distribution, $P(E_T)$ allows two images with different absolute ion counts compared. If the translational energy released is remarkably different, the quadratic point spacing from speed conversion ($E_T \propto v^2$) may bias the normalization. Linear interpolation of the $P(E_T)$ obviates both the normalization bias and the necessity to plot data against a nonlinear x-axis. The interpolation uses a fixed x-scaling ΔE_T and rescales the number of resultant points, ensuring the same scaling factor irrespective of molecule.

The energy available for translation after breaking the molecular bond D_0, allowing for the vibrational, rotational and spin-orbit state of the detected species $E_{v,J,so}$ if necessary, at a given pump energy $h\nu$, and initial internal excitation of the molecule (assumed to be negligible in the molecular beam) is given by

$$E_{T,max} = h\nu - D_0 - E_{v,J,so} + E_{int}$$

$E_{T,max}$ corresponds to the maximum translational energy release possible. Fragments with $E_T < E_{T,max}$ indicates that energy is disposed into internal modes of the co-fragment. To compare

fragments formed by photolysis at different pump energies, on an equal energy available basis, the distributions can be converted into fractional translational energy release

$$f_T = \frac{E_T}{E_{T,max}}$$

The linearly interpolated $P(E_T)$ can be converted to $f(E_T)$ by changing the x-scaling from ΔE_T to $\Delta E_T / E_{T,max}$.

2.6.1   An new view of ion images: parameterized coordinates

The information contained in ion images is typically extracted into radial (speed/energy) and angular (anisotropy) distributions, as shown in Figure 2-5 (b)-(c). Decoupling the two may obscure changes in the underlying dynamics. Instead the idea presented below is to represent the information contained in the ion images using parameterized coordinates, *i.e.*

$$I(r, \theta) \rightarrow I(E_T, \beta)$$

A typical parameterized coordinate plot is shown in Figure 2-5 (d). From each image a population P and anisotropy parameter β for each E_T is extracted. Acquiring multiple images gives an uncertainty $\sigma(\beta)$. The idea is to use a Gaussian to describe β, the width is described by the uncertainty in β. The pre-factor ensures the Gaussian remains area normalized regardless of σ.

$$F(\beta) = \frac{1}{\sqrt{2\pi}\,\sigma}\, e^{\frac{-(\beta - \beta_0)^2}{2\sigma^2}}$$

A Gaussian at each value of E_T is produced, the area is given by the population P, the position given by β and width determined by $\sigma(\beta)$. Repeating over the whole distribution:

$$I(E_T, \beta) = \frac{P(E_T)}{\sqrt{2\pi}\,\sigma_\beta(E_T)} e^{\frac{-(\beta - \beta(E_T))^2}{2(\sigma_\beta(E_T))^2}}$$

Where $P(E_T)$ is the population distribution, $\beta(E_T)$ is the anisotropy distribution, $\sigma_\beta(E_T)$ is the standard deviation in the anisotropy distribution. β is a grid of values spanning -2 $\leftrightarrow$ 3 to avoid curtailing the Gaussian width. The pre-factor ensures that the intensity remains directly proportional to $P(E_T)$ regardless of changes in the standard deviation in β.

2.7 **References**

1.   Parker, D. H. & Eppink, A. T. J. B. Photoelectron and photofragment velocity map imaging of state-selected molecular oxygen dissociation/ionization dynamics. *The Journal of Chemical Physics* **107,** 2357–2362 (1997).
2.   Eppink, A. T. J. B. & Parker, D. H. Velocity map imaging of ions and electrons using electrostatic lenses: Application in photoelectron and photofragment ion imaging of molecular oxygen. *Review of Scientific Instruments* **68,** 3477–3484 (1997).
3.   Anderson, J. B. & Fenn, J. B. Velocity Distributions in Molecular Beams from Nozzle Sources. *Physics of Fluids (1958-1988)* **8,** 780–787 (1965).
4.   Livingstone, R. A. *et al.* Time-resolved photoelectron imaging of excited state relaxation dynamics in phenol, catechol, resorcinol, and hydroquinone. *The Journal of Chemical Physics* **137,** 184304 (2012).
5.   Wrede, E. *et al.* Continuum state spectroscopy: A high resolution ion imaging study of IBr photolysis in the wavelength range 440–685 nm. *The Journal of Chemical Physics* **114,** 2629–2646 (2001).
6.   *SimIon.* (Scientific Services Inc.).
7.   Townsend, D., Minitti, M. P. & Suits, A. G. Direct current slice imaging. *Review of Scientific Instruments* **74,** 2530–2539 (2003).
8.   Boyd, R. W. *Nonlinear Optics.* (Academic Press, 2003).
9.   *PGOPHER, a Program for Simulating Rotational Structure, C. M. Western, University of Bristol, http://pgopher.chm.bris.ac.uk.* (PGOPHER, a Program for Simulating Rotational Structure, C. M. Western, University of Bristol, http://pgopher.chm.bris.ac.uk).

10. Kung, A. H., Young, J. F. & Harris, S. E. Generation of 1182-Å radiation in phase-matched mixtures of inert gases. *Applied Physics Letters* **22,** 301–302 (1973).
11. Kung, A. H., Young, J. F. & Harris, S. E. Erratum: Generation of 1182-Å radiation in phase-matched mixtures of inert gases. *Applied Physics Letters* **28,** 294–294 (1976).
12. Wynne, J. J. Coherent VUV Generation By Nonlinear Processes. *J. Phys. Colloques* **39,** C4–69–C4–74 (1978).
13. Mahon, R., McIlrath, T., Myerscough, V. & Koopman, D. Third-harmonic generation in argon, krypton, and xenon: Bandwidth limitations in the vicinity of Lyman- #945; *IEEE Journal of Quantum Electronics* **15,** 444–451 (1979).
14. Friedberg, R., Hartmann, S. R. & Manassah, J. T. Optimizing third harmonic generation in gases. *J. Phys. B: At. Mol. Opt. Phys.* **24,** 2883 (1991).
15. Whitaker, B. J. *Imaging in Molecular Dynamics: Technology and Applications*. (Cambridge University Press, 2003).

3 Near-UV photodissociation dynamics of CH$_2$I$_2$
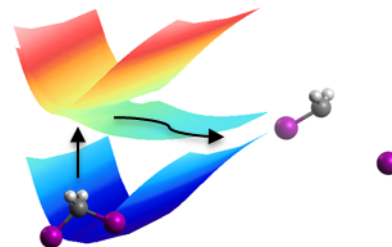
3.1 Abstract

The near-UV photodissociation dynamics of CH$_2$I$_2$ has been investigated using a combination of velocity-map (slice) ion imaging and *ab initio* calculations characterizing the excited states. Ground state I(^{2}P$_{3/2}$) and spin-orbit excited I*(^{2}P$_{1/2}$) atoms were probed using 2+1 resonance-enhanced multiphoton ionization (REMPI) or with single-photon VUV ionization. Two-color ion images were recorded at pump wavelengths of 355 nm, 266 nm and 248 nm, and one-color ion images at the REMPI wavelengths of ~304 nm and ~280 nm. Analysis of the ion images shows that, regardless of iodine spin-orbit state, ~20% of the available energy is partitioned into translation E_T at all excitation wavelengths indicating that the CH$_2$I co-fragment is formed highly internally excited. The translational energy distributions comprise a slow, "statistical" component that peaks near zero and faster components that peak away from zero. The slow component makes an increasingly large contribution to the distribution as the excitation wavelength is decreased. The C–I bond dissociation energy of D$_0$ = 2.155±0.008 eV is obtained from the trend in the E_T release of the faster components with increasing excitation energy. The I and I* ion images are anisotropic, indicating prompt dissociation, and are characterized by β parameters that become increasingly positive with increasing E_T. The decrease in β at lower translational energies can be attributed to deviation from

axial recoil. MRCI calculations including spin-orbit coupling have been performed to identify the overlapping features in the absorption spectrum and characterize one-dimensional cuts through the electronically excited potential energy surfaces. The excited states are of significantly mixed singlet and triplet character. At longer wavelengths, excitation directly accesses repulsive states primarily of B_1 symmetry, consistent with the observed $\langle \beta \rangle$, while shorter wavelengths accesses bound states, also of B_1 symmetry that are crossed by repulsive states.

3.2   **Introduction**

Diiodomethane (CH_2I_2) is one of the most important sources of iodine atoms in the marine boundary layer.[1,2] Tropospheric iodine chemistry exerts an influence on the oxidative capacity of the atmosphere and can also lead to new particle formation.[2] The reaction of iodine atoms with ozone forms iodine monoxide (IO), which can subsequently react with HO_2 or NO_2 to form photolabile products that may participate in catalytic ozone destruction[2,3] and accounts for $\sim$50% of the total ozone loss in the MBL.[4] The chemistry is initiated by photolysis. CH_2I_2 absorbs strongly at $\lambda <$ 360 nm[5,6] overlapping significantly with the solar spectrum and the large photolysis rate results in an atmospheric lifetime of only a few minutes.[6]   The photolysis products are predominantly iodomethyl radicals and either ground $I(^2P_{3/2})$ or spin-orbit excited $I(^2P_{1/2})$ atoms (henceforth labelled I and I*, respectively), with a combined quantum yield, Φ, of unity.[7–9]

$$CH_2I_2 \rightarrow CH_2I + I \qquad D_0 = 2.155 \pm 0.008 \text{ eV} \qquad (1)$$

$$CH_2I_2 \rightarrow CH_2I + I^* \qquad D_0 = 3.098 \pm 0.008 \text{ eV} \qquad (2)$$
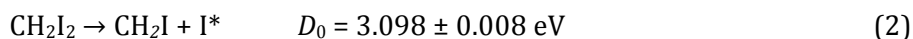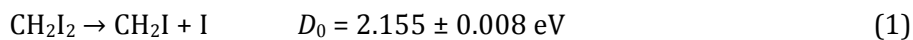
The bond dissociation energies have been derived from the results of this work (*vide infra*). An additional minor channel forming $CH_2 + I_2$ (Φ = 0.004) has been identified at an excitation

49

wavelength of 248 nm.[10]   Recently, diiodoalkanes have been widely used as iodoalkyl radical precursors used for laboratory production of atmospherically important carbonyl oxide biradicals, or Criegee intermediates by reaction with molecular oxygen.[11,12] Recently, we have reported preliminary evidence suggesting that the degree of internal excitation in the photolytically-generated CH_2I radical may affect the kinetics and product branching of the $CH_2I + O_2$ reaction.[13]   A major motivation for this work was characterization of the CH_2I internal energy distribution at common photolysis wavelengths, with a view to exploring its influence on kinetics.

The near-UV absorption spectrum of CH_2I_2 at 298 K, shown in

Figure 3-1, has typically been deconvolved into four Gaussian components, but is otherwise unstructured.[14] Assignments have been derived from an exciton model proposed by Kawasaki *et al.* that treats the molecule as a pair of weakly coupled chromophores. The model predicts six electronic states in C_{2v} symmetry, although transitions to the state of A_2 symmetry are electric dipole forbidden.[15]   The intense long wavelength band is assigned to two overlapping bands centered at 312 and 286 nm, both of B_1 symmetry. The weaker feature at 250 nm is attributed to unresolved transitions to B_2 and A_1 states. A state of A_1 symmetry is responsible for the intense short wavelength absorption band at 214 nm. Subsequent magnetic circular dichroism (MCD) measurements, however, suggest that the first absorption band corresponds to excitation to states of B_1 and B_2 symmetry and identify the state responsible for the band at 248 nm as A_1.[16] The MCD measurements also reveal a weak shoulder near the long-wavelength onset of the first absorption band that was attributed to a nominally forbidden transition, most probably a triplet state.[16] Electronic structure calculations on CH_2I_2 are limited and the predicted electronic state symmetries disagree with the exciton model. Zheng and Phillips used time-dependent density functional theory (TD-DFT) to characterize the first five singlet (and triplet) excited electronic states, resulting in assignments that agree with the interpretation of the MCD experiments.[17] More recent calculations

have characterized the electronic states using the CASPT2 method[18] and TD-DFT,[19] although only the former study included spin-orbit coupling. Unsurprisingly for a molecule with two iodine atoms many of the excited states have strongly mixed singlet and triplet character. An apparent discrepancy between the CASPT2 and earlier TD-DFT results in the identification of the excited valence states can be attributed to the choice of coordinate system, which switches the B_1 and B_2 labels. Here we adopt the convention established first, in which the C_2 symmetry axis is defined as the z-axis and the y-axis is normal to the heavy atom plane.

Several groups have investigated the photodissociation dynamics of CH_2I_2 in the gas phase and the band assignments derived from the exciton model have formed the basis of almost all interpretation of the experimental data. Photofragment translational spectroscopy (PTS) experiments with mass spectrometric detection of photoproducts were performed by Kawasaki *et al.* using broadband excitation centered at 310 nm, and spanning the first absorption band. Analysis of the angular distribution of the photofragments resulted in an anisotropy parameter of β = 0.9, indicative of prompt dissociation after excitation to states of B_1 symmetry, consistent with the results of their exciton model. Similar experiments at a shorter photolysis wavelength of 266 nm measured angular distributions in excellent accord with Kawasaki *et al.*, and also photofragment flight times that indicated the production of highly-internally excited CH_2I.[20] Baughcum and Leone observed strong infrared emission across the range 590–4100 cm^{-1} after photolysis at 308 and 248 nm, concluding that CH_2I radicals are produced with internal excitation corresponding to a quasi-continuum density of states. Strong distinct emission features were observed in the CH stretch (up to four quanta), CH_2 bending and combination regions.[7]

The branching between I and I* depends strongly upon the excitation wavelength. The quantum yield for I* over the wavelength range 248–366 nm has been independently measured by atomic

emission spectroscopy.[7,8] and photoacoustic yield spectroscopy.[9] While the latter technique resulted in slightly smaller I* yields, both measurements agree that the quantum yield for I* is effectively zero at 355 nm and monotonically increases towards shorter wavelength, approaching $\Phi = 0.5$ at 248 nm. When scaled by the absorption cross section, the I* yield apparently maps the second Gaussian component representing excitation to the second electronic state, as shown in Figure 3-1 suggesting that this state correlates with spin-orbit excited I* atoms. The observation that I atoms are also formed was attributed to a curve crossing mechanism.[9]
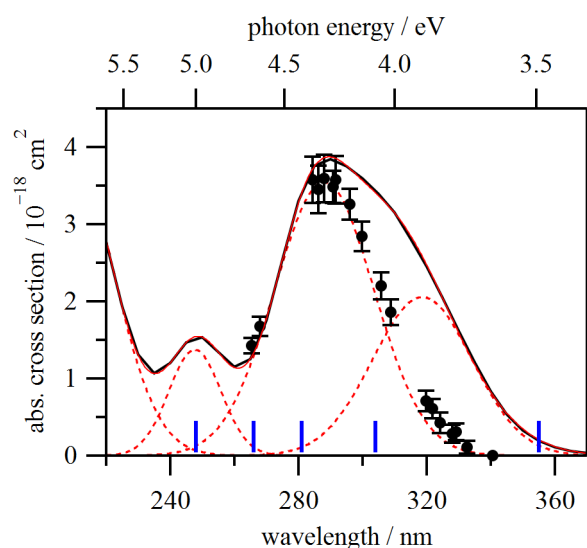
Figure 3-1. Absorption spectrum for CH_2I_2 (black) measured by Roehl et al., overlaid with individual Gaussian components (red). The black symbols indicate relative I* quantum yields weighted by the absorption cross section, as measured by Koffend and Leone. The vertical blue lines indicate the pump wavelengths used in this work.

2+1 REMPI spectroscopy has also been used to detect I and I* photoproducts, exploiting probe transitions with wavelengths falling within the first absorption band of CH_2I_2. Jung *et al.* used time-of-flight mass spectrometry to measure product velocity distributions, dissociating CH_2I_2 and probing I and I* near 304 nm. I* atoms were found to be the minor product, with $\Phi = 0.25$, the low recoil velocities confirmed extensive internal excitation of the CH_2I radical fragment. The anisotropy parameters of 0.4 and 0.55 for formation of I and I* atoms, respectively, are generally smaller than the earlier PTS experiments, and the limiting value, but still consistent with a transition to a dissociative B_1 state.[21] A similar one-color dissociation and ionization approach was

taken by Xu *et al*. who used several wavelengths between 277 and 304 nm with velocity-map imaging (VMI) detection of I and I*.[22] The total translational energy distributions obtained probing I atoms were deconvolved into two major Gaussian components, each of which showed a positive β. In contrast, translational energy distributions obtained after imaging I* were dominated by a single component that shared the value β of the slower I atom component. Following the exciton model state assignments, the 1^1B_1 state correlates with CH_2I + I and produces I atoms exclusively. The higher-lying 2^1B_1 state correlates adiabatically with CH_2I + I* atoms, but may also produce I atoms by non-adiabatic coupling to the lower 2^1A_1 state. More recently, Lehman *et al.* used two-color VMI experiments to examine the photochemistry of CH_2I_2 at 248 nm, using 2+1 REMPI at 313 nm to probe I* atoms.[23] The probe wavelength is strongly absorbed by the parent molecule and resulted in intense one-color signals. After subtraction, the translational energy distributions were again consistent with highly internally excited CH_2I fragments but showed some evidence of bimodality. The measured β = 0.81±0.05 is consistent with prompt dissociation after a transition to a B_1 state, and is not in accord with either the exciton model or the MCD assignment.[23] Some consistent trends in the photodissociation dynamics emerge over the photolysis wavelength range 248–310 nm. The average fraction of the available energy partitioned into the internal modes of the CH_2I radical is consistently $f_{INT} \approx 0.8$–0.9, regardless of the iodine atom spin-orbit level. The dissociation appears to be prompt and the angular anisotropy at all excitation wavelengths suggests parallel transitions, predominantly to states of B_1 symmetry. Neither the initially excited electronic state nor changes in total energy available appear to significantly change the photodissociation dynamics. The characters of the electronically excited states, however, remain the subject of some uncertainty.

In this paper we report new experimental measurements that systematically examine the photodissociation dynamics of CH_2I_2 following excitation at five wavelengths spanning the near-UV absorption spectrum. DC slice velocity-map imaging (VMI) has been combined with state-selective

resonance-enhanced multiphoton ionization (REMPI) or vacuum ultraviolet ionization (VUV) to probe I and I* atoms. The experimental measurements are complemented by electronic structure calculations, including the effects of spin-orbit coupling, which characterize the electronically excited states responsible for the absorption spectrum and the photochemistry.

3.3   Experiment

Experiments were performed in a recently constructed DC slice velocity-map imaging (VMI) spectrometer.   The apparatus consists of source, ionization and drift/detection regions, each evacuated by dedicated turbomolecular pumps (Leybold 1100C, Pfeiffer 700M and Leybold 360) backed by an oil-free Roots pumps (Adixen one ACP28G, and two ACP15G) to base pressures of $\sim 4 \times 10^{-7}$ Torr. A liquid sample of CH_2I_2 (Sigma-Aldrich, 99% purity) was stored in a stainless-steel bubbler. Ar carrier gas at a pressure of ~ 1 atm passed over the sample and was supersonically expanded into the source region using a solenoid pulsed valve (General Valve Series 9).   The expansion was skimmed (Beam Dynamics Inc.) between the source and ionization regions to form a molecular beam, directed along the time-of-flight axis. Based on the vapor pressure of CH_2I_2 at 295 K, we estimate that the molecular beam comprised $\sim 0.15\%$ CH_2I_2. The pressure in the source region increased to 2×10^{-6} Torr during valve operation.

The CH_2I_2/Ar molecular beam was intersected by counter-propagating pump (photolysis) and probe laser beams, λ_{pump} and λ_{probe} in the center of a stack of velocity-mapping electrodes, optimized for DC slicing of the ion cloud. The pump beam spans the range 248–355 nm and is generated using a tunable mid-band optical parametric oscillator (OPO) pumped by the third harmonic of a Nd:YAG laser (Continuum Horizon II and Surelite EX). The pump beam was focused using a fused silica lens (f = 300 mm). Pulse energies were typically < 1 mJ, which coupled with the relatively broad OPO

bandwidth of ~5 cm^{-1} give a low peak intensity and reduces the likelihood of driving (resonant) multiphoton dissociation processes. Iodine atoms formed in the dissociation were probed approximately 10–20 ns after photolysis using both single-photon VUV ionization and 2+1 REMPI. The VUV beam at λ_{probe} = 118.2 nm was generated by frequency tripling the third harmonic of a Nd:YAG laser (Continuum Surelite II-10) in a low pressure static gas cell containing a phase-matched mixture of Xe and Ar (1:50 ratio at P < 50 Torr). The attenuated 355 nm beam (< 8 mJ) was gently focused into the cell by an external fused silica lens (f = 500 mm) while an internal MgF$_2$ lens (f = 200 mm), which also acts as a window to separate the mixing cell from the high-vacuum ionization region, focused the VUV into the molecular beam and approximately re-collimates the residual 355 nm. Optimization of phase-matching was achieved while monitoring VUV ionization of the CH$_2$I$_2$ parent molecule. The REMPI probe beam was generated by frequency doubling in β-barium borate (BBO) the fundamental output of a Nd:YAG-pumped dye laser (Lambda-Physik Scanmate 2 and Continuum Surelite II-10) operating with either Rhodamine 590 or 640 dyes.

The laser sources generate horizontally polarized radiation, while the experiment requires both pump and probe pulses to be vertically polarized. The polarization of the pump radiation from the OPO was rotated using a combination of a variable phase retardation wave plate (Alphalas GmbH) set to act as a half-wave plate and a Rochon polarizer (MgF$_2$, Edmund Optics). The fixed-frequency VUV polarization was controlled by placing a 355 nm half-wave plate in the beam path of the Nd:YAG third harmonic. The REMPI probe polarization was rotated using a photo-elastic modulator (PEM) and delay pulse generator (Hinds Instruments PEM-100 and DPG-5000), capable of performing arbitrary phase retardation of laser pulses. The delay pulse generator synchronizes the intrinsic 50 kHz oscillation frequency of the PEM crystal with the 10 Hz repetition rates of other components, by externally triggering an eight-channel digital delay generator (Quantum Composers 9528) at 10 Hz, which in turn controls the synchronization of all other components.

The velocity-mapping ion optics stack comprises five electrodes optimized for DC slicing[24] of the expanded ion cloud and the construction follows an established design.[25] Velocity-mapping is obtained with an extractor-to-repeller voltage ratio of 0.87. The detector comprises a pair of 40 mm diameter chevron-stacked microchannel plates (MCPs) coupled to a P46 phosphor screen (Photonis). A fast high voltage switch (Photek GM-MCP-2) was used to pulse the voltage applied to the rear MCP, which limited the effective gain to only 22 ns. The arrival time of the I^+ ions was stretched to 135 ns, hence only 16% of the full ion packet is detected, satisfying the requirements for a narrow central slice.[24]

Images were acquired at the 10 Hz repetition rate of the lasers using a CCD camera (Basler a312f, 782× 582 pixels) and transferred to the data acquisition (DAQ) PC for pre-processing in real time. Event counting was performed in software, using both spot size and intensity to discriminate between genuine ion strikes and background counts. Sub-pixel precision was achieved by calculating the centroid of each ion strike and is used to upscale a native 512×512 pixel region of interest chosen, by a factor of two to 1024×1024. During image acquisition, the total phosphorescence emitted by the detector screen, and the pump and probe laser pulse energies are monitored by a silicon photomultiplier (SenSL, MicroSL 10020-X18) and a photodiode (Thorlabs, DET-10A), respectively. These signals are acquired by an oscilloscope (Teledyne Lecroy, HDO4054), which is also interfaced to the DAQ PC.

Automated routines are implemented in the data acquisition software (National Instruments, Labview 2013) to maximize the robustness of data acquisition and minimize the impact of long-term variations in experimental conditions. Images are acquired in sets, each of which involves cycling (typically for 2500 shots) over several different pump wavelengths while the probe laser is repeatedly scanned across the Doppler profile. In addition to two-color [pump + probe] images,

[pump only] and [probe only] images were also acquired to allow removal of one-color background signals. The process was repeated until the desired signal-to-noise ratio was achieved. Individual measurement sets (~300,000 laser shots/image) were repeated three times. Where appropriate, the one-color background signals were subtracted prior to any further image analysis.

3.3.1   Spectrometer Calibration

Photofragment speeds, v, are related to the image radius, R (in pixels), by

$$v = NR/t \tag{3}$$

where N is a calibration factor that must be determined empirically, and t is the flight time of the detected photofragment. The well-studied photodissociation of OCS was used to provide images to calibrate the VMI spectrometer:[26]

$$OCS \rightarrow CO + S(^1D) \qquad D_0 = 4.2908 \pm 0.0030 \text{ eV} \tag{4}$$
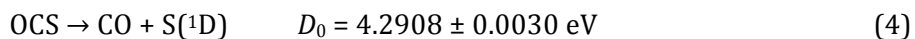
Excitation in the wavelength range 222–250 nm leads to prompt dissociation, forming predominantly CO $X^1\Sigma^+(v = 0, J)$ and S(^{1}D), which was probed using 2+1 REMPI via the $^1F_3$ state at a one-photon probe wavelength of 288.18 nm. The calibration set is based on the photodissociation of OCS at λ_{pump} = 222, 235 and 250 nm. The calibration factor was adjusted to best match the resolved high-J levels of the CO(v=0) fragment to a rotational comb calculated using previously reported spectroscopic constants for CO.[27] The accuracy of the scaling factor was cross-checked using published data from several previous studies of OCS photodissociation.[26,28–30]

3.4 **Theory**

The electronic ground state geometry of CH_2I_2 was optimized at the explicitly correlated coupled cluster with single, double and perturbative triple excitations [CCSD(T)-F12b] level of theory,[31,32] using the correlation consistent cc-pVQZ-F12 basis sets for carbon and hydrogen,[33] and the cc-pVQZ-PP-F12 basis set paired with the small-core relativistic pseudopotential (PP) ECP28MDF for iodine.[34,35] The density fitting of the Fock and exchange matrices used the cc-pVQZ/JKFit and def2-QZVPP/JKFit auxiliary basis sets,[36,37] while the aug-cc-pwCV5Z/MP2Fit and cc-pVQZ-PP-F12/MP2Fit sets were used in the density fitting of the remaining two-electron integrals.[34,38] The many-electron integrals arising in explicit correlation theory were accurately and efficiently approximated using the resolution-of-the-identity method with cc-pVQZ-F12/OptRI and cc-pVQZ-PP-F12/OptRI used in the complementary auxiliary basis set (CABS) approach.[34,39,40] The geminal Slater exponent was set to 1.0 a_0^{-1} in all cases. Such combinations of basis sets and pseudopotentials will be referred to as cc-pVnZ-F12 herein. Initial testing demonstrated that CCSD(T)-F12b/cc-pVDZ-F12 produced an almost identical geometry as explicitly correlated internal contracted multi-reference configuration interaction with the Davidson correction (MRCI-F12+Q),[41–43] hence the more computationally tractable coupled cluster method was used for geometry optimization with larger basis sets. The vertical excitations energies of the first 19 excited states ($3 \times {}^1A_1$, $2 \times {}^1B_1$, $2 \times {}^1B_2$, $2 \times {}^1A_2$, $3 \times {}^3A_1$, $3 \times {}^3B_1$, $2 \times {}^3B_2$, and $2 \times {}^3A_2$) were obtained at the MRCI-F12+Q/cc-pVQZ-F12 level based on a full-valence complete-active-space self-consistent field (CASSCF) reference. The CABS singles correction was applied to the CASSCF reference energies.[44] In order to calibrate the error in the MRCI-F12+Q vertical excitation energies, the adiabatic excitation energy to the first triplet excited state was compared to that obtained from the composite coupled cluster approach of Peterson *et al.*[45] This protocol includes corrections for basis set incompleteness, core-valence effects, scalar relativity and higher order correlation, thus it

should provide almost exact Born-Oppenheimer approximation results in the absence of spin-orbit coupling. The MRCI-F12+Q results were found to overestimate the excitation energy by 0.09 eV, indicating that resulting calculated absorption spectra may be slightly blue-shifted relative to experiment. Spin-orbit coupling was conducted on the 19 spin-free states at the MRCI level using the cc-pVQZ-PP basis and PP for iodine and the cc-pVQZ basis for all other elements.[35,46] For iodine the spin-orbit operator defined in the pseudopotential was used, while the Breit-Pauli operator was used for lighter atoms. The energy eigenvalues computed in the preceding MRCI/cc-pVQZ calculation were replaced by those precomputed at the MRCI-F12+Q/cc-pVQZ-F12 level, hence only the spin-orbit matrix elements are computed at the lower level of theory.

Potential energy curves were computed by scanning along a single C–I bond distance and keeping all other internal coordinates fixed at the equilibrium geometry. The reduction in symmetry from C_{2v} to C_s necessitated that these calculations were carried out at the MRCI-F12+Q/cc-pVDZ-F12 level of theory, including the first 17 spin-free states ($5 \times {}^1A'$, $4 \times {}^1A''$, $4 \times {}^3A'$, and $4 \times {}^3A''$, these states were selected based on an inspection of the contributions of the spin-free states to the composition of the spin-orbit eigenvectors at the equilibrium geometry). This resulted in a total of 33 spin-orbit coupled levels calculated at the MRCI level with cc-pVDZ-PP for iodine and cc-pVDZ for all other elements. Again, the energy eigenvalues of the spin-free states were replaced by those computed at the MRCI-F12+Q/cc-pVDZ-F12 level.

All calculations were performed using the MOLPRO 2012.1 quantum chemistry package.[47,48]

3.5 **Results**

DC sliced velocity-map ion images of I and I* atom products have been recorded following excitation of CH_2I_2 at pump wavelengths of 355 nm, 266 nm and 248 nm. Single photon VUV ionization was used to detect ground state I atoms, while 2+1 REMPI at one-photon wavelengths

near 281 nm and 304 nm was used to detect both I and I*. Since CH_2I_2 absorbs strongly at the REMPI probe wavelengths, one-color probe only images provide data at these additional wavelengths. Extraction of the two-color signal, however, requires a careful background subtraction procedure when using the REMPI detection schemes. The energy available E_{AVL} to the photofragments after cleavage of a C–I bond is

$$E_{AVL} = h\nu - D_0 = E_{INT} - E_{SO} - E_T \tag{5}$$

where $h\nu$ is the pump photon energy and D_0 is the bond dissociation energy. E_{AVL} can be partitioned into internal excitation (rotation and vibration) of the CH_2I radical E_{INT}, spin-orbit excitation of the iodine atom E_{SO} (zero for I and 0.9426 eV for I*) and relative translation E_T, which is derived from the images. It is assumed that the CH_2I_2 parent has near-zero internal energy prior to absorption of the pump photon as a result of cooling in the supersonic expansion.

VUV ionization provides an effectively state selective means of detecting ground state I atoms. Iodine has an ionization potential of 10.45126 eV, which is marginally less than the 10.49 eV VUV photons generated by frequency tripling the Nd:YAG 3rd harmonic. At 118.2 nm, an accidental resonance with an autoionizing Rydberg state results in 19.2 times greater sensitivity for I over I*.[49,50] The I* quantum yield increases monotonically from zero at 355 nm to a maximum of around 0.46 at 248 nm. Consequently, I* atoms account for at most ~2% of the total ion counts in the images acquired using the VUV probe.[8] CH_2I can also be ionized at 118.2 nm, but the CH_2I^+ signal in the mass spectrum was around an order of magnitude weaker than that of I^+ this product was not pursued for imaging studies. Ion images recorded using VUV detection of I atoms formed from the photodissociation of CH_2I_2 at 355 nm, 266 nm and 248 nm are shown in Figure 3-2. Relatively minor pump-only and probe-only contributions have been subtracted. At all pump

wavelengths, the maximum observed I atom speed is significantly slower than the maximum possible. At 355 nm, the anisotropic ring shown in Figure 3-2 corresponds to formation of I atoms with speeds of ~450 m s–1. The radius of the ring increases at 266 nm and 248 nm, indicating speeds of >600 ms–1, and becomes more diffuse. A slower component in the center of the image is evident at 266 nm and increases in intensity at 248 nm.
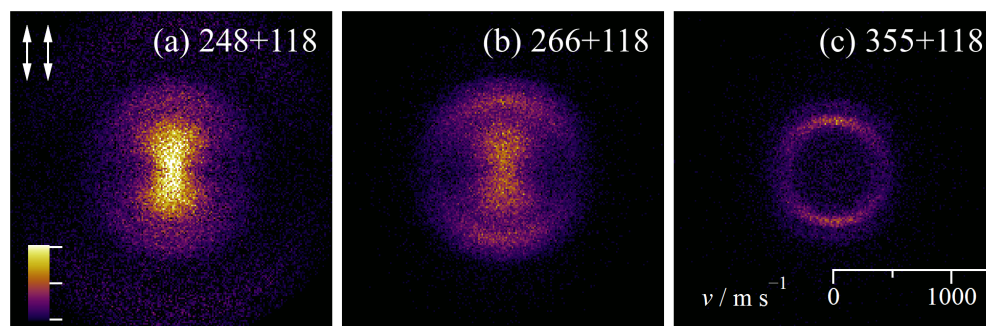
Figure 3-2. Ion images of I atom products of the photodissociation of CH2I2 for λpump + λprobe (in nm): (a) 248 + 118, (b) 266 + 118 and (c) 355 + 118. Small background pump-only and probe-only signals have been subtracted.

2+1 REMPI was also used to probe atomic iodine products. Ground state I atoms were probed *via* the $(^3P_1)6p[0]_{1/2}$ and $(^3P_2)6p[1]_{1/2}$ states at λ_{probe} = 279.71 nm and 303.69 nm. Spin-orbit excited I* atoms were probed *via* the $(^1D_2)6p[3]_{5/2}$ and $(^3P_1)6p[1]_{1/2}$ states at nearby λ_{probe} = 281.73 nm and 304.03 nm.[21] Use of 2+1 REMPI to detect I and I* is complicated by strong absorption of the CH2I2 parent at the probe wavelengths, which are near the first absorption maximum (see

Figure 3-1). Strong one-color, probe-only signals where $\lambda_{pump} = \lambda_{probe}$ are unavoidable. Figure 3-3 shows typical one-color ion images probing I* atoms at both REMPI probe wavelengths alongside the equivalent two-color images recorded using a photolysis wavelength of 266 nm and the images resulting from a scaled subtraction procedure (described below). The one-color images [Figure 3-3(a) and (d)] are dominated by an intense outermost ring, and a slower component that makes a relatively larger contribution at 282 nm. The radii of the outer rings depend upon photolysis

wavelength and correspond to I atom speeds of 395 m s^{-1} at 304 nm and ~465 m s^{-1} at 282 nm. The two-color images [Figure 3-3(b) and (e)] are dominated by the exclusively probe-induced signal, but weak additional contributions are present at both larger and smaller radii. Under typical experimental conditions, the desired pump-induced two-color signal accounts for only ~15% of the total image intensity.
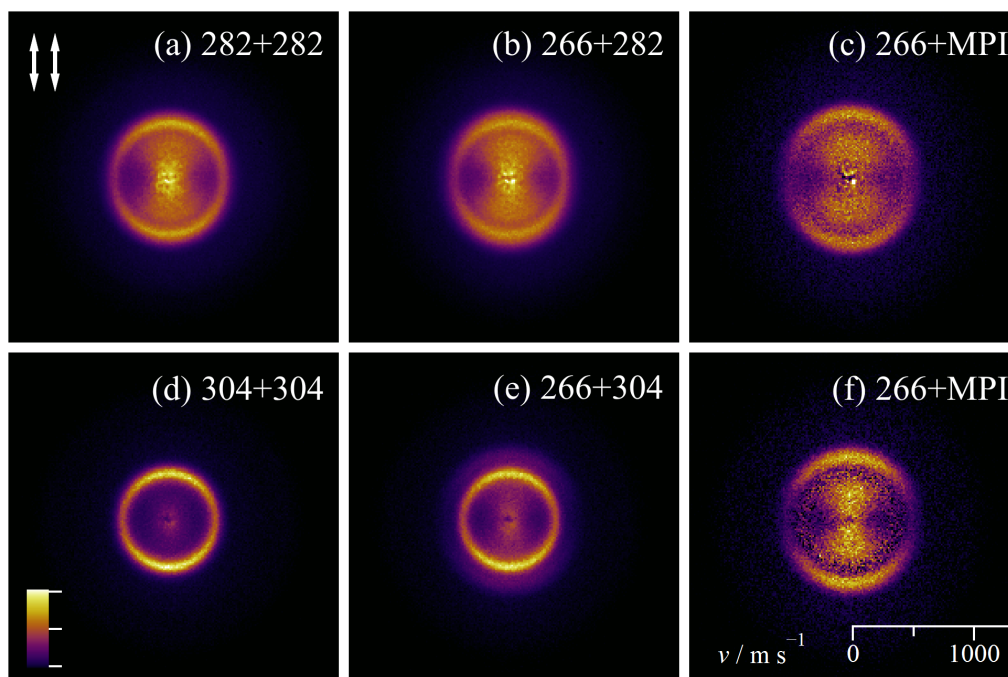
Figure 3-3. Ion images of I* products detected with REMPI after the photodissociation of CH$_2$I$_2$ at $\lambda_{pump} + \lambda_{probe}$ (in nm). Top row: (a) 282 + 282, (b) 266 + 282, (c) 266 + MPI difference image obtained from scaled subtraction i.e. (b) – f(a). Bottom row: (d) 304 + 304, (e) 266 + 304, (f) 266 + MPI difference image obtained from scaled subtraction i.e. (e) – f(d)

The magnitude of the one-color signal makes subtraction from the two-color signal challenging. The translational energy distributions derived from two-color and one-color images recorded back-to-back were used to isolate the desired pump-induced distributions i.e. [pump + probe] – [probe only]. Unscaled subtraction invariably led to bleaching at values of E_T that coincide with the λ_{probe}-

dependent maxima in the one-color distributions. This could be a consequence of CH_2I_2 parent

depletion in the molecular beam when the pump beam is present. The $P(E_T)$ arising from pump-

induced dissociation should, however, be independent of the choice of probe wavelength and can be

recovered by minimizing the deviation between the difference distributions measured at each

independent probe wavelength by scaling the probe-only contributions i.e. [pump + probe] −

f[probe only], where f is a scaling factor. After deriving the scaling factor, the scaled one-color

images can be subtracted from the two-color images, as shown in Figure 3-3(c) and (f). The

procedure is illustrated in Figure 3-4 for detection of ground state I atoms at a photolysis

wavelength of 266 nm, for which we have independent measurements of the $P(E_T)$ from the VUV

ionization experiments. The agreement between the distributions obtained from the REMPI and

VUV data, shown in Figure 3-4, is excellent at E_T < 1 eV. The similarity of these distributions also

demonstrates that the VUV probe does not drive dissociative ionization of highly internally excited

CH_2I radicals to from CH_2 + I^+ to any significant extent. The small, fast and broad shoulder that

appears between ∼1–2 eV in the REMPI difference distribution is absent in the VUV data but is

attributed to a small amount of multiphoton dissociation induced by the probe laser.
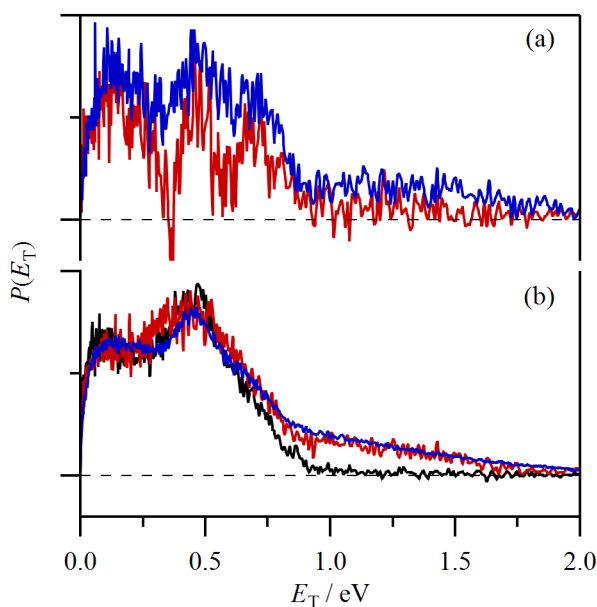
Figure 3-4. Illustration of subtraction procedure for REMPI measurements at a pump wavelength of 266 nm and probing ground state I atoms. (a) unscaled [pump+probe]–[probe] ET distributions obtained probing at 280 nm (blue) and 304 nm (red). The dips occur where the one-color distributions have maxima. (b) ET distributions after subtracting scaled one-color distributions as described in the text. The ET distribution obtained independently using VUV ionization (black) is shown for comparison.

Translational energy distributions at each pump wavelength obtained from images probing I atoms are presented in Figure 3-5. The distributions labelled "+MPI" are composites obtained from data acquired using two different REMPI transitions, as described above. The conversion from speed to translational energy assumed that CH_2I was the co-fragment. The $P(E_T)$ at pump wavelengths of 355 nm, 266 nm and 248 nm were obtained from two-color ion images recorded using VUV ionization, while those at 280 nm and 304 nm were derived from one-color images using the REMPI probe scheme. Excitation at 355 nm leads exclusively to ground state I + CH_2I, although I* atoms are also energetically accessible and results in an E_T distribution that can be fit by a single Gaussian function centered at ~0.25 eV. The E_T distribution cuts off well before the total available energy, E_{AVL} = 1.34 eV, at this excitation wavelength. At the shorter pump wavelengths of 304 nm, 280 nm and 266 nm, the $P(E_T)$ can be broadly described by three components and are fit to an exponentially modified Gaussian function (EMG), which describes the slow statistical-like component that peaks near E_T = 0, and two Gaussian functions (G1 and G2), which represent the two faster components. The maximum observed E_T is < 1 eV at all pump wavelengths despite E_{AVL} ranging from 1.93–2.51

64

eV, indicating significant internal excitation of the CH$_2$I radical co-fragment. The slow component, which is first apparent at 304 nm, makes increasingly large contributions to the total $P(E_T)$ at shorter pump wavelengths. The G1 and G2 components are most distinct at 304 nm; G2 is reduced to a shoulder at 280 nm and 266 nm, and can no longer be resolved at 248 nm. The centers of G1 and G2 both move to higher E_T as E_{AVL} increases. The fraction of E_{AVL} partitioned into translational energy, $f_T = \langle E_T \rangle / E_{AVL}$, is 0.23±0.06 at 355 nm and decreases to only 0.15±0.02 at 248 nm.
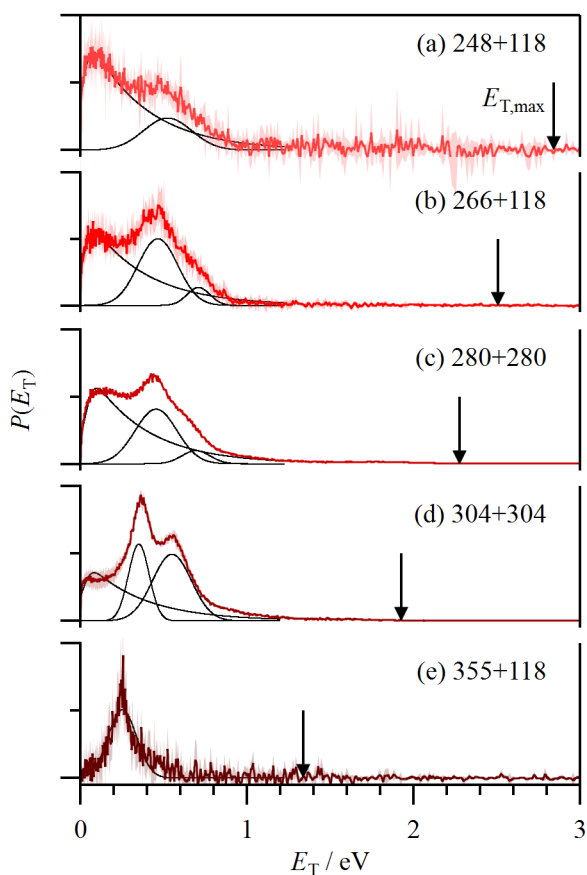
Figure 3-5. Translational energy distributions derived from I atom images following photodissociation of CH$_2$I$_2$ for combinations of $\lambda_{pump} + \lambda_{probe}$ (in nm). (a) 248 + 118, (b) 266 + 118, (c) 280 + 280, (d) 304 +304 and (e) 355 +118. All distributions are normalized to the same area and displayed on the same vertical scale. The thin black lines indicate components of the fits, which are described in the text.

Figure 3-6 shows translational energy distributions obtained probing I* atoms using 2+1 REMPI. The $P(E_T)$ at pump wavelengths of 266 nm and 248 nm are determined from two-color images using the scaled subtraction procedure described above. The scaled subtraction procedure results in excellent agreement between the $P(E_T)$ obtained from REMPI and VUV data for I atoms, shown in

Figure 4, and provides confidence that it will also be reliable when probing I* atoms. The data at 304 nm and 282 nm are derived from one-color images. Qualitatively, the E_T distributions obtained probing I* shown in Figure 6 are similar to those shown in Figure 3-5. At all pump wavelengths, the E_T cutoff lies far below E_{AVL} and a slow component peaking near $E_T = 0$ makes an increasing contribution as the pump wavelength decreases. There is, however, only a single obvious faster component. The E_T distributions are again deconvolved by fitting to an exponentially modified Gaussian function to describe the slower component (EMG*) and a Gaussian function (G1*) to describe the faster component. At 304 nm, G1* is centered at 0.19 eV with FWHM of 0.10 eV. This feature shifts to greater E_T and broadens as E_{AVL} increases. At 248 nm, G1* is centered at $E_T = 0.35$ eV and has an equivalent FWHM. Similar fractions of the available energy are partitioned in to translational energy for I* atom products for which $f_T = 0.23\pm0.01$ at 304 nm, decreasing to 0.19 ± 0.01 at 248 nm.
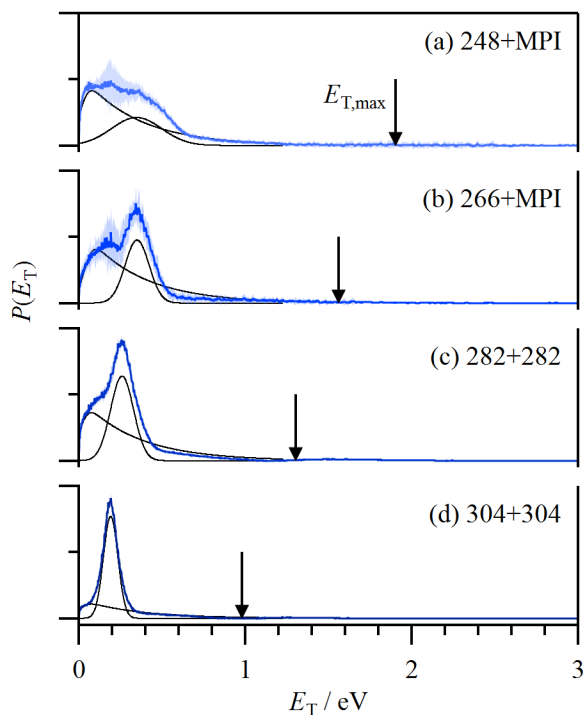
Figure 3-6. Translational energy distributions derived from I* atom images following photodissociation of CH_2I_2 for combinations of $\lambda_{pump} + \lambda_{probe}$ (in nm). (a) 248 + REMPI, (b) 266 + REMPI, (c) 280 + 280 and (d) 304 + 304. REMPI probe refers to the average distribution obtained from two independent probe transitions. All distributions are normalized to the same area and displayed on the same vertical scale. The thin black lines indicate components of the fits, which are described in the text.

The peak centers obtained from the fits of the faster moving G1, G2 and G1* components shift to higher energy linearly with increasing excitation energy. Figure 3-7 shows the peak centers, E_{peak}, plotted against ($E_{pump} - E_{SO}$), the difference between the pump photon energy and the spin-orbit energy of the iodine atom. For spin-orbit excited I* atoms, $E_{SO} = 0.9426$ eV. The G1 and G1* components appear to fall on the same line and are distinct from G2. The C–I bond dissociation energy, D_0, can be determined from a linear fit to the data in Figure 3-7 assuming a linear increase in peak positions with increasing E_{AVL} beyond D_0. From the fit to the larger, combined G1+G1* data set, we obtain $D_0 = 2.155\pm0.008$ eV, where the quoted uncertainty represents the uncertainty in the fit. This result is in excellent agreement with $\Delta H = 2.24\pm0.06$ eV determined from thermochemical data at 298 K. A linear fit to the more limited G2 data returns a value of D_0 that is in agreement, although with significantly greater uncertainty ($D_0 = 2.17\pm0.18$ eV). Bailleux et al.[51] have inferred spin-orbit coupling constant of 1400 cm^{-1} (0.17 eV) for CH$_2$I. The common intercept suggests either that no spin-orbit excited CH$_2$I is formed in the dissociation or that the spin-orbit splitting is significantly smaller.
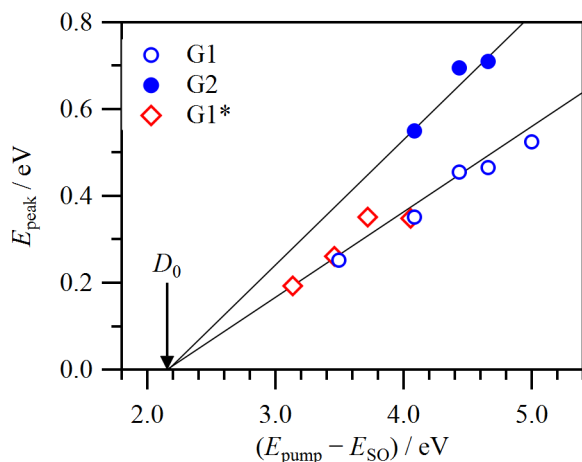
Figure 3-7. Peak centers of intermediate (G1/G1*) and fast (G2) Gaussian components of the E_T distributions plotted as a function of the difference between the pump photon energy and the spin-orbit energy of the probed I (blue) or I* (red) atom.

Speed-dependent, and ultimately E_T-dependent, anisotropy parameters, $\beta(E_T)$, were determined by radially integrating the sliced ion images and fitting the angular distributions to the usual expression

$$I(\theta) \propto 1 + \beta P_2(\cos\theta) \tag{6}$$

where P_2 is the second Legendre polynomial and θ is the polar angle. In general, the observed values of β are positive at all ET for all pump wavelengths and tends to increase from near zero, indicating a near-isotropic distribution, at low E_T. Inclusion of higher order Legendre polynomials did not improve the fit. For each pump wavelength, the variation of the anisotropy parameter with the translational energy is represented in Figure 3-8. The shaded area represents the uncertainty in β arising from fitting to equation (6) and repeated measurements. At longer pump wavelengths, the faster moving fragments dominate the distribution and are characterized by $\beta > 0$. At shorter wavelengths the slower component increases in importance, and the anisotropy is reduced. While the individual components are heavily overlapped at all pump wavelengths, it seems unlikely that there is any significant variation. At 304 nm, where the G1 and G2 components are most readily distinguished, the values of β are effectively the same. ET-averaged values of the anisotropy parameter, $\langle\beta\rangle$, are reported in Table 3-1. $\langle\beta\rangle$ varies somewhat with pump wavelength, being most anisotropic at 266 nm and decreasing slightly at both longer and shorter pump wavelengths, largely due to the increasing contribution of the near-isotropic EMG component. Spin-orbit excited I* atoms show slightly more anisotropic angular distributions than ground state I atoms, but the wavelength-dependent trends are the same.
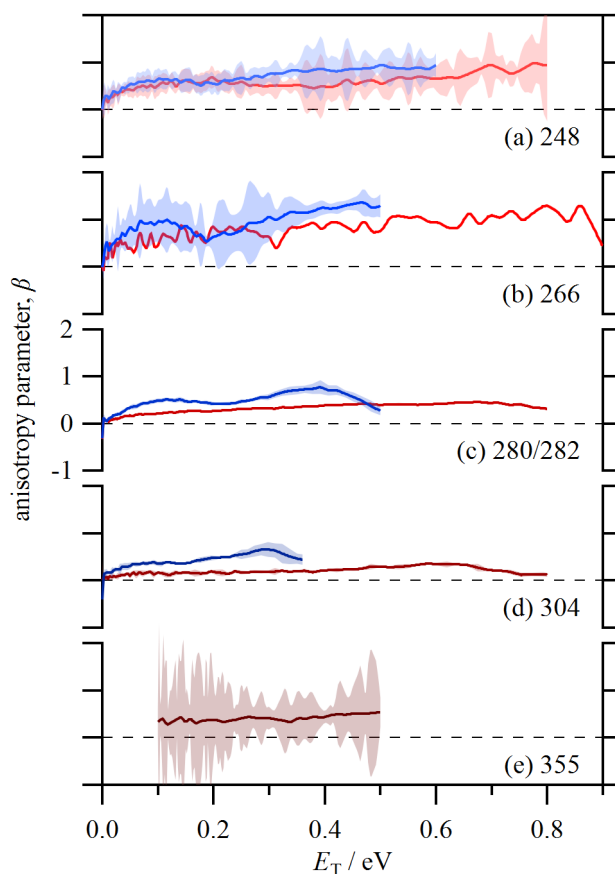
Figure 3-8. E_T-dependent anisotropy parameters derived from ion images probing I (red) and I* (blue) at the excitation wavelengths (a) 248 nm, (b) 266 nm, (c) 280/282 nm, (d) 304 nm, and (e) 355 nm.

The absorption spectrum calculated from spin-orbit MRCI calculations at the quadruple-zeta level is compared to experiment in Figure 9, with the calculated data shifted red by 27 nm and each transition broadened by 30 nm FWHM Gaussian. It can be seen that this leads to excellent agreement with experiment, especially in the region 265–360 nm. At shorter wavelengths, the weaker feature at ~250 nm is not reproduced by the calculations and the intensity of the band at 214 nm is overestimated, suggesting that larger active spaces and the inclusion of Rydberg states may be necessary for quantitatively correct results in this region, but such calculations are computationally intractable on currently available resources. Figure 9 also shows the major

contributing peaks to the spectrum and it is evident that the long wavelength band is generally dominated by B_1 states. The weak shoulder near the long-wavelength onset of this band can be assigned to a B_2 state at roughly 355 nm. All of the excited states possess significant triplet character, which is presented as contributions to the spin-orbit eigenvectors in Table 2 along with vertical excitation energies and transition dipole moments.
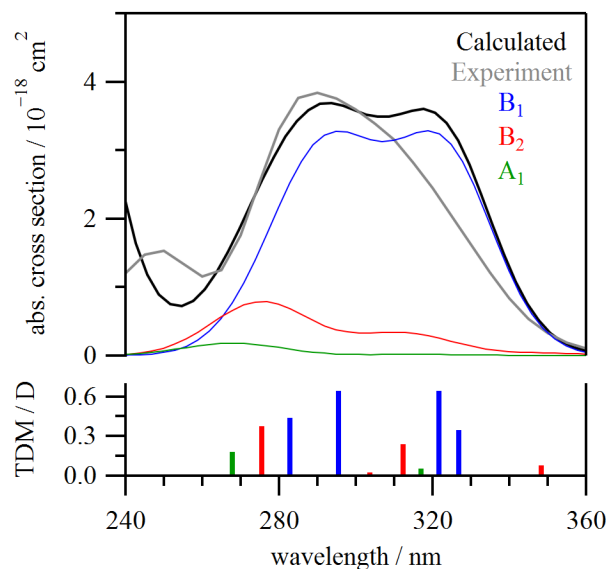
Figure 3-9. Upper panel: calculated absorption spectrum (shifted red by 27 nm) compared to experiment. Each vertical transition, shown in the lower panel, has been broadened by a 30 nm FWHM Gaussian function.

The spin-orbit coupled potential energy curves (double-zeta level) calculated for the stretching of the C–I bond are shown in Figure 10. For clarity, only the first 16 spin-orbit states (out of the 33 resulting from the 17 spin-free electronic states) are shown, with all excluded higher energy states leading to higher energy dissociation products than those depicted. Technical difficulties meant that MOLPRO reverted to C_1 symmetry in many of the spin-orbit coupling calculations, yet assignment of states to A′ or A″ was straightforward from inspection of transition dipole moments. Calculations at the equilibrium geometry allowed each curve to be also assigned in C_{2v}-like symmetry, which is shown in the Figure legend, and the eight excited states with the greatest oscillator strengths at the equilibrium geometry are emboldened. The electronically excited states shown in Figure 3-10 can be divided into four distinct groups (see Table 3-2), each similar in nature and leading to a different

set of asymptotic products. Group I and II states are essentially repulsive and correlate with the first two product asymptotes, $CH_2I + I$ and $CH_2I + I^*$. The energy gap between group I and II states is ~0.84 eV at 4.2 Å, which is in excellent agreement with the energy difference between the ground $^2P_{3/2}$ and spin-orbit excited $^2P_{1/2}$ levels of iodine at this level of theory (0.86 eV). This is in agreement with the CASPT2 study of Liu *et al.*[18] The group III and IV states, which make increasingly important contributions to the absorption spectrum at shorter excitation wavelengths, are bound and correlate asymptotically with the formation of electronically excited $CH_2I + I/I^*$. Excited radical products are inaccessible at the excitation energies used in the current experiments; we note that the product asymptotes of the PECs show no splitting arising from spin-orbit coupling in the CH_2I radical.
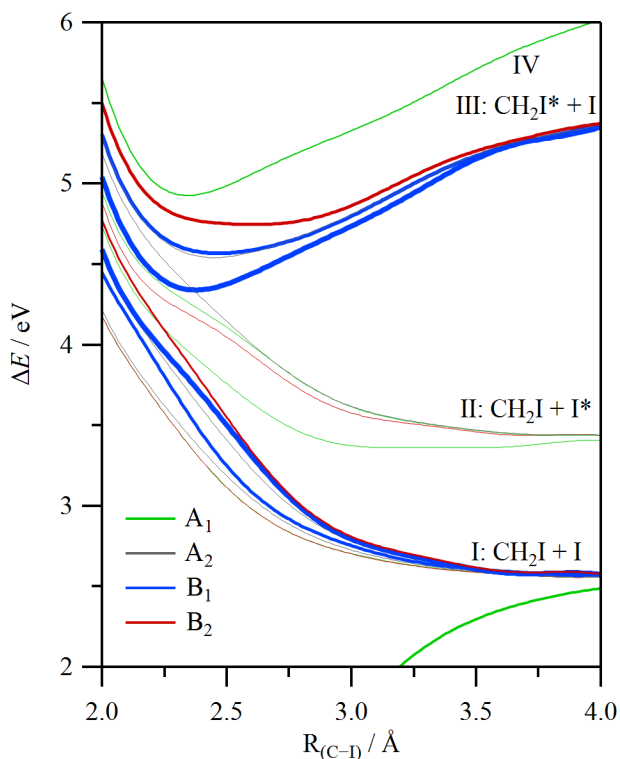
Figure 3-10. Potential energy curves with respect to the C–I bond coordinate including spin-orbit coupling. States corresponding to excitations with significant transition dipole moments have thicker lines and symbols.

3.6 **Discussion**

The translational energy distributions and anisotropy parameters measured in this work are in excellent agreement with previous one-color time-of-flight measurements by Jung *et al.* probing both I and I* at 304 nm. The ion imaging results of Xu *et al.*[22] agree at best qualitatively with the results of this work. Xu *et al.* derive values of $\beta > 1$ and show E_T distributions that are essentially invariant across the 277–304 nm range of excitation wavelengths. The tabulated peak positions derived from the decomposition of the E_T distributions disagree with the figures, suggesting an error in the presentation. In contrast, we find that $\langle \beta \rangle < 1$ generally. At pump wavelengths where the data are most directly comparable, our measurements indicate G1* components that are centered at E_T = 0.19 eV and 0.26 eV at at 304 nm and 282 nm, respectively, while Xu *et al.* report 0.24 eV and 0.25 eV. An analogous slow component that increased in magnitude at shorter pump wavelengths was also observed by Xu *et al.*, although it remained a minor component.

Lehman *et al.* used VMI to study the photodissociation of CH_2I_2 at 248 nm, but probed only I* using a REMPI probe transition near 313 nm, which also generated strong one-color signals.[23] The E_T distribution derived from difference images appeared bimodal, and showed a pronounced dip at E_T ≈ 0.15 eV (coinciding with the peak of the one-color E_T distributions) that is not present in the current measurements. While we agree that the translational energy distribution at a pump wavelength of 248 nm is bimodal, the dip in the earlier measurement of Lehman *et al.* may be an artifact of over-subtraction of the one-color signal. The anisotropy parameter of β = 0.81 ± 0.05, however, is in reasonable agreement with our E_T-averaged value of $\langle \beta \rangle$ = 0.74 ± 0.03 at the same pump wavelength.

The results of our measurements support the consensus view that dissociation of CH_2I_2 after

72

excitation in the near UV is prompt and that the bulk of the excess energy is partitioned into internal excitation of CH_2I. The translational energy distributions generally contain two distinct features – a slow component peaking near zero translational energy that increases in relative intensity at shorter wavelengths and faster non-zero peaking component(s). The slow component has been observed in previous imaging studies. We discount the possibility of three-body fragmentation to $CH_2 + I + I$ or unimolecular dissociation of internally excited CH_2I as the origin of the slow component on the basis of thermochemical data, which suggests a threshold wavelength of $\lambda_{pump} < 245$ nm. Furthermore, secondary dissociation of CH_2I photofragments by absorption of an additional photon is expected to lead to products with significant translational energy.[20] We have considered the effects of slicing on slow fragments, and tests using polar onion-peeling[52] to analyze unsliced images return near-identical speed distributions. The degree of translational energy release can be rationalized by the application of a simple impulsive model. In the "pure impulsive" model of Busch and Wilson,[53] the fraction of E_{AVL} partitioned into translation depends upon the ratio of the reduced masses of the atoms between which the bond breaks, μ_b, and the final photofragments, μ_f.

$$f_T = \mu_b/\mu_f \qquad (7)$$

The model assumes an instantaneous repulsion between the departing I atom and the CH_2 moiety, which is treated as a pseudo-atom, while the I atom that remains bound to C is initially a spectator. The model predicts $f_T = 0.19$, which is in reasonably good agreement with the 0.15–0.24 range observed experimentally. The wavelength-dependence of the translational energy release, however, cannot be accounted for using this model. The fractions of the available energy partitioned in to CH_2I vibration and rotation also depend on the kinematics, attenuated by the bond angle:

$$f_V = (1 - \mu_b/\mu_f)\cos^2 \alpha_0 \tag{8}$$

$$f_R = (1 - \mu_b/\mu_f)\sin^2 \alpha_0 \tag{9}$$

Using the experimental bond angle determined from microwave spectroscopy, $\alpha_0 = \angle(\text{ICI}) = 114.0°$,[54] the pure impulsive model predicts $f_V = 0.13$ and $f_R = 0.68$. The partitioning between vibrational and rotational excitation of the CH_2I fragments is not determined at the resolution obtainable in the VMI experiments. IR emission measurements after excitation at 248 nm and 308 nm by Baughcum and Leone indicate very high levels of vibrational excitation. Prominent features were observed in spectral regions corresponding to the C–H stretch (~ 3000 cm^{-1}), the CH_2 bend (~ 1300 cm^{-1}) and combinations of these two modes.[7] Emission in the region of the C–I stretch (~ 600 cm^{-1}) was also observed and resonance Raman studies have established that bond fission occurs following initial symmetric stretching of both C–I bonds.[17,55] Although not explicitly identified, it seems likely that the low frequency out-of-plane bend (~ 375 cm^{-1}) would also be excited as a result of the pyramidal-to-planar geometry change about the C atom following dissociation. The high degree of vibrational excitation observed in earlier experiments suggests that the impulsive model likely overstates the fraction of available energy partitioned into rotation of the CH_2I fragment.

At all excitation wavelengths, the photofragment angular distributions are anisotropic. In general, the anisotropy parameters derived from the images have values of $\beta > 0$, and generally increase steadily with increasing translational energy release. The limiting anisotropy parameter for a prompt dissociation is given by

$$\beta = 2P_2(\cos \chi) \tag{10}$$

where χ is the angle between the transition dipole moment of the parent molecule and the recoil velocity vector ($\boldsymbol{\mu} \cdot \boldsymbol{v}$). CH_2I_2 has C_{2v} symmetry, and transitions to states of A_1, B_1 and B_2 symmetry (with transition dipole moments oriented along the z, x, and y-axes, respectively) are electric dipole allowed. Following Demyanenko *et al.*,[56] axial recoil is defined as motion along the Jacobi coordinate $\boldsymbol{R}$, the vector between the departing I atom and the center of mass of the CH_2I radical, rather than along the C–I bond axis, which has been adopted by some authors.[22,23] The angle δ defines the orientation of the transition dipole moment to this vector ($\boldsymbol{\mu} \cdot \boldsymbol{R}$). Within the axial recoil limit, $\delta = \chi$ and the anisotropy parameters can be readily predicted using the geometry of CH_2I_2 determined from microwave spectroscopy.[54] For transition dipole moments corresponding to excitation to B_1, B_2 and A_1 states δ takes values of 3.6°, 90.0° and 86.4°, respectively and the limiting anisotropy parameters are predicted to be +1.99, –1 and –0.99. Only transitions to states of B_1 symmetry can result in $\beta > 0$.

The observation of photofragment anisotropy is indicative of prompt dissociation on a timescale less than the rotational period of the parent molecule. Slower dissociation could lead to the "statistical", isotropic components observed in the E_T distributions where $\beta(E_T) \approx 0$ after excitation at shorter wavelengths. For the faster moving components, $\beta > 0$ is consistent with dissociation on a repulsive surface of B_1 symmetry, although the anisotropy is significantly smaller than predicted for axial recoil following excitation to a pure B_1 state. One possible explanation is simultaneous excitation to states of A_1 or B_2 symmetry, both of which are predicted to result in $\beta \approx -1$, and would reduce the observed value of β. The difficulty of isolating individual components in the E_T distributions would suggest that the topology of the repulsive A_1 or B_2 surfaces contributing to the dissociation be similar to the B_1 state and lead to similar energy partitioning. This interpretation is broadly and qualitatively consistent with the results of the *ab initio* calculations. The calculated absorption spectrum is indeed dominated by transitions to states of B_1 symmetry (see Figure 3-9),

75

accompanied by far weaker transitions to a few states of A_1 and B_2 symmetry. The contribution to the absorption cross section of the lowest energy 1 B_2 (1 A″) excited state is very small and absorption is dominated by the 1 B_1 (3 A′) and 2 B_1 (4 A′) states at the longest excitation wavelengths. All three of these states are repulsive and lead directly to CH_2I + I products. At shorter wavelengths, the absorption is dominated by transitions to higher lying *bound states* of B_1 symmetry, specifically the 3 B_1 (7 A′) and 4 B_1 (8 A′), with a smaller contribution from the bound 3 B_2 (8 A″) state. Absorption to bound states at shorter wavelengths could be responsible for the near-isotropic slow component in the $P(E_T)$ distributions, indicating some degree of trapping on the excited surface. The bound states are crossed by repulsive states that correlate to I* products. None of the states correlating with CH_2I + I* products is strongly absorbing; the most significant is the 3 A_1 (5 A′) state, which has a transition dipole moment an order of magnitude smaller than the 1 B_1 and 2 B_1 states that dominate the long-wavelength absorption. However, the generally larger values of $\langle \beta \rangle$ observed when probing I* suggest that direct excitation to the 3 A_1 (5 A′) state does not make a major contributor to the dissociation dynamics. The *ab initio* results imply that essentially all I* is produced via non-adiabatic transitions to one of the four repulsive surfaces that correlate to the spin-orbit excited product asymptote.

The overall reduction and the general increase in β with increasing fragment translational energy may additionally be a consequence of transverse recoil. Following the simple classical model of Demyanenko *et al.*,[56] the deflection angle α between the recoil velocity **v** and the Jacobi coordinate **R_c** at some critical distance at which the fragment angular momenta are established can be calculated using conservation of energy and angular momentum:

$$\sin \alpha = \sqrt{I_{CH_2I} f_R / I_c f_T} \tag{11}$$

Here I_{CH_2I} is the moment of inertia of the CH$_2$I fragment, approximated as a pseudo-diatomic classical rotor, and I_c is the moment of inertia of the total system, evaluated at the distance R_c. In addition to the critical distance, rotation of the Jacobi coordinate in the laboratory frame can be accounted for by inclusion of a critical angle, α_c. Together, R_c and α_c define a geometry at which the final angular momenta of the separating fragments are determined. In general they are not known *a priori*, but can be used as fitting parameters. The variables f_R and f_T are the fractions of ($E_{AVL}-E_V$) partitioned into rotation and translation, respectively. The anisotropy parameter can be calculated using equation (10) where $\chi = \alpha_c + \alpha$. Transverse recoil, characterized by large values of α, will be important when f_R is large relative to f_T and the moment of inertia of the system at the critical distance and angle is comparable to that of the nascent CH$_2$I radical fragment. As a limiting case we assume impulsive dissociation, that is, the angular momenta are established immediately and the critical distance and angle are determined by the parent molecule geometry. In this case, R_c = 3.4 Å and $\alpha_c = \delta = 3.6$ for a transition to a B$_1$ state. Using the energy partitioning predicted by the impulsive model (f_R = 0.68, f_T=0.19) results in a deflection angle of α = 31.1° and an anisotropy parameter of β = 1.03, which is in reasonably good agreement with the experimental results. Increasing the fraction of the available energy partitioned into vibration (or equivalently, reducing f_R while holding f_T constant) causes β to increase. With f_V = 0.26 and f_R = 0.55, the predicted anisotropy parameter is β = 1.19. While a more quantitative approach using R_c and α_c as fitting parameters to model the E_T-dependent anisotropy parameter, is in principle possible, it is unfeasible because the vibrational population distribution is unknown.

The photochemistry of CH$_2$I$_2$ can be compared to that of other iodine-containing molecules. CH$_3$I has been extensively studied and its photochemistry has been recently been summarized by Gardiner et al.[50] The first absorption band results from excitation to states, labeled $^1Q_1$, $^3Q_0$ and $^3Q_1$, that are dissociative along the C–I coordinate. Parallel transition to the $^3Q_0$ state is predominantly

responsible for the absorption spectrum and correlates with $CH_3 + I^*$, although the photochemistry is complicated by the existence of a conical intersection with the $^1Q_1$ state. In general, the excess energy is partitioned almost entirely into relative translation and a strong preference for production of spin-orbit excited I^* atoms is observed, in marked contrast to CH_2I_2. Larger fractions of the available energy are partitioned into the alkyl radical fragments following photodissociation of larger alkyl iodides, although the propensity for production of I^* over I remains and the analogous electronic states determine the photochemistry.[50,57] The long-wavelength photochemistry of CH_2BrI is perhaps more directly comparable to CH_2I_2.[58] At 248 nm, dissociation to form $CHBr + I$ dominates and the behavior is generally similar to CH_2I_2; specifically, the transitions are predominantly parallel in character, the majority of the available energy is partitioned into the radical fragment, and the I/I^* spin-orbit branching also favors the ground state.

Finally, we consider the implications for kinetics studies which use photolysis of CH_2I_2 as a source of CH_2I radicals. CH_2I is formed in conjunction with both I and I^* atoms at all but the longest pump wavelengths. The translational energy releases are in general similar and relatively small, resulting in E_{INT} distributions for CH_2I that depend primarily on the spin-orbit state formed. Overall E_{INT} distributions are constructed by weighting the distributions obtained probing either I or I^* by the appropriate quantum yields.[8] The resulting distributions are shown in Figure 3-11 for λ_{pump} = 355 nm, 266 nm, and 248 nm, corresponding to laser wavelengths (Nd:YAG 3rd and 4th harmonic or KrF excimer) that are commonly used to prepare CH_2I radicals for kinetics studies. At 355 nm, CH_2I radicals are formed only in conjunction with ground state I atoms resulting in a unimodal internal energy distribution with $\langle E_{INT} \rangle$ = 1.03±0.08 eV. At shorter wavelengths, the E_{INT} distributions for the CH_2I radicals extend to even higher energy and contain two distinct components corresponding to formation of I and I^* atoms. For example, at 248 nm, where the branching to I and I^* is similar, an approximately equal amount of CH_2I radicals will be formed with $\langle E_{INT} \rangle$ = 2.42±0.02 eV in

conjunction with I atoms, and $\langle E_{INT} \rangle$ = 1.55±0.02 eV for those formed with I*.
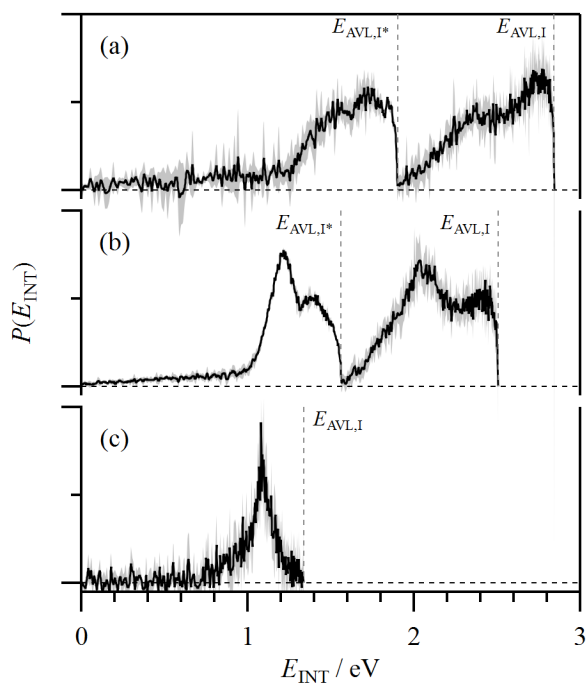
Figure 3-11. Overall CH$_2$I internal energy distributions, constructed from I and I* measurements weighted by respective quantum yields at pump wavelengths of (a) 248 nm, (b) 266 nm, and (c) 355 nm.

Recently, we have investigated the kinetics of the reaction between CH$_2$I and O$_2$ using cavity ring-down spectroscopy to probe IO radical products, using 355 nm photolysis of CH$_2$I$_2$ to generate iodomethyl radicals.[13] IO radicals were found to be produced in both v = 0 and v = 1, the latter with a significantly larger bimolecular rate constant, but a far smaller yield. It was proposed that the photolytically-generated hot CH$_2$I* radicals react with O$_2$ to form IO(v = 0,1) directly and promptly prior to thermalization, while the majority of IO(v = 0) production occurs more slowly via the CH$_2$OO + I reaction. Photolysis of CH$_2$I$_2$ at 266 nm and 248 nm produces CH$_2$I radicals with even greater internal excitation. Caution is necessary in the interpretation of kinetics studies that use photolysis as a means to generate reactive radicals for kinetics studies, particularly if performed at low pressures where the assumption of thermalization prior to reaction may not be valid.

3.7 Conclusions

The photodissociation dynamics of CH_2I_2 following excitation over a range of wavelengths has been examined experimentally using velocity-map ion imaging, using both state-selective REMPI and single-photon VUV ionization to detect I and I* products. The images show only modest translational energy release, indicating significant partitioning of the available energy into the internal modes of the CH_2I radical co-fragment. Analysis of the photofragment anisotropy results in weakly speed-dependent positive anisotropy parameters, suggesting excitation to B_1 states. The reduction from the limiting value of +2 is attributed to both weak contributions to the absorption from states of A_1 and B_2 symmetry and transverse recoil. The experimental observations are supported by complementary high-level *ab initio* calculations that have mapped out the spin-orbit coupled electronically excited states responsible for the first absorption bands. The calculations indicate that the absorption spectrum is dominated by transitions to states of B_1 symmetry and all states have significant triplet character; the lower energy states accessed at longer wavelengths are purely repulsive, but excitation at shorter wavelengths accesses bound states that dissociate by rapid non-adiabatic coupling to nearby repulsive surfaces.

3.8 Acknowledgements

3.9 References

1. Carpenter, L. J. Iodine in the Marine Boundary Layer. *Chem. Rev.* **103,** 4953–4962 (2003).
2. Saiz-Lopez, A. *et al.* Atmospheric Chemistry of Iodine. *Chem. Rev.* **112,** 1773–1804 (2012).
3. Chameides, W. L. & Davis, D. D. Iodine: Its possible role in tropospheric photochemistry. *J.*

Geophys. Res. **85,** 7383–7398 (1980).

4. Read, K. A. *et al.* Extensive halogen-mediated ozone destruction over the tropical Atlantic Ocean. *Nature* **453,** 1232–1235 (2008).

5. Roehl, C. M., Burkholder, J. B., Moortgat, G. K., Ravishankara, A. R. & Crutzen, P. J. Temperature dependence of UV absorption cross sections and atmospheric implications of several alkyl iodides. *J. Geophys. Res.* **102,** 12819–12829 (1997).

6. Mössinger, J. C., Shallcross, D. E. & Cox, R. A. UV-VIS absorption cross-sections and atmospheric lifetimes of CH_2Br_2, CH_2I_2 and CH_2BrI. *J. Chem. Soc., Faraday Trans.* **94,** 1391–1396 (1998).

7. Baughcum, S. L. & Leone, S. R. Photofragmentation infrared emission studies of vibrationally excited free radicals CH_3 and CH_2I. *J. Chem. Phys.* **72,** 6531–6545 (1980).

8. Koffend, J. B. & Leone, S. R. Tunable laser photodissociation: quantum yield of $I^*(^2P_{1/2})$ from CH_2I_2. *Chem. Phys. Lett.* **81,** 136–141 (1981).

9. Hunter, T. F. & Kristjansson, K. S. Yield of $I(^2P_{1/2})$ in the photodissociation of CH_2I_2. *Chem. Phys. Lett.* **90,** 35–40 (1982).

10. Chen, S.-Y. *et al.* I_2 molecular elimination in single-photon dissociation of CH_2I_2 at 248 nm by using cavity ring-down absorption spectroscopy. *J. Chem. Phys.* **134,** 034315 (2011).

11. Taatjes, C. A., Shallcross, D. E. & Percival, C. J. Research frontiers in the chemistry of Criegee intermediates and tropospheric ozonolysis. *Phys. Chem. Chem. Phys.* **16,** 1704–1718 (2014).

12. Osborn, D. L. & Taatjes, C. A. The physical chemistry of Criegee intermediates in the gas phase. *Int. Rev. Phys. Chem.* **34,** 309–360 (2015).

13. Foreman, E. S. & Murray, C. Kinetics of IO Production in the $CH_2I + O_2$ Reaction Studied by Cavity Ring-Down Spectroscopy. *J. Phys. Chem. A* **119,** 8981–8990 (2015).

14. Ito, M., Huang, P. C. & Kosower, E. M. Electronic absorption spectra of iodo- and bromomethanes. *Trans. Faraday Soc.* **57,** 1662–1673 (1961).

15. Kawasaki, M., Lee, S. J. & Bersohn, R. Photodissociation of molecular beams of methylene iodide and iodoform. *J. Chem. Phys.* **63,** 809–814 (1975).

16. Gedanken, A. & Rowe, M. D. Magnetic circular dichroism of iodoform and methylene iodide. *Chem. Phys.* **36,** 181–186 (1979).

17. Zheng, X. & Phillips, D. L. Density functional theory and resonance Raman investigation of the ultraviolet electronic excited states of CF2I2. *Chem. Phys. Lett.* **316,** 524–530 (2000).

18. Liu, Y.-J., De Vico, L., Lindh, R. & Fang, W.-H. Spin-Orbit Ab Initio Investigation of the Ultraviolet Photolysis of Diiodomethane. *ChemPhysChem* **8,** 890–898 (2007).

19. Mandal, A., Singh, P. J., Shastri, A. & Jagatap, B. N. Electronic state spectroscopy of diiodomethane (CH2I2): Experimental and computational studies in the 30 000–95 000 cm−1 region. *J. Chem. Phys.* **140,** 194312 (2014).

20. Kroger, P. M., Demou, P. C. & Riley, S. J. Polyhalide photofragment spectra. I. Two-photon two-step photodissociation of methylene iodide. *J. Chem. Phys.* **65,** 1823–1834 (1976).

21. Jung, K.-W., Ahmadi, T. S. & El-Sayed, M. A. Photofragment Translational Spectroscopy of CH_2I_2 at 304 nm: Polarization Dependence and Energy Partitioning. *B. Korean Chem. Soc.* **18,** 1274–1280 (1997).

22. Xu, H. *et al.* Photodissociation dynamics of CH_2I_2 molecules in the ultraviolet range studied by ion imaging. *J. Chem. Phys.* **117,** 5722–5729 (2002).

23. Lehman, J. H., Li, H. & Lester, M. I. Ion imaging studies of the photodissociation dynamics of CH_2I_2 at 248 nm. *Chem. Phys. Lett.* **590,** 16–21 (2013).

24. Townsend, D., Minitti, M. P. & Suits, A. G. Direct current slice imaging. *Rev. Sci. Instrum.* **74,** 2530–2539 (2003).

25. Livingstone, R. A. *et al.* Time-resolved photoelectron imaging of excited state relaxation dynamics in phenol, catechol, resorcinol, and hydroquinone. *J. Chem. Phys.* **137,** 184304 (2012).

26. Lipciuc, M. L. & Janssen, M. H. M. Slice imaging of quantum state-to-state photodissociation dynamics of OCS. *Phys. Chem. Chem. Phys.* **8,** 3007–3016 (2006).

27. Guelachvili, G., de Villeneuve, D., Farrenq, R., Urban, W. & Verges, J. Dunham coefficients for seven isotopic species of CO. *J. Mol. Spectrosc.* **98,** 64–79 (1983).

28. Suzuki, T., Katayanagi, H., Nanbu, S. & Aoyagi, M. Nonadiabatic bending dissociation in 16 valence electron system OCS. *J. Chem. Phys.* **109,** 5778–5794 (1998).

29. Brouard, M., Green, A. V., Quadrini, F. & Vallance, C. Photodissociation dynamics of OCS at 248nm: The $S(^1D_2)$ atomic angular momentum polarization. *J. Chem. Phys.* **127,** 084304 (2007).

30. Lipciuc, M. L., Rakitzis, T. P., Meerts, W. L., Groenenboom, G. C. & Janssen, M. H. M. Towards the complete experiment: measurement of $S(^1D_2)$ polarization in correlation with single rotational states of CO(J) from the photodissociation of oriented OCS($v_2 = 1|JlM = 111$). *Phys. Chem. Chem. Phys.* **13,** 8549–8559 (2011).

31. Adler, T. B., Knizia, G. & Werner, H.-J. A simple and efficient CCSD(T)-F12 approximation. *J. Chem. Phys.* **127,** 221106 (2007).

32. Knizia, G., Adler, T. B. & Werner, H.-J. Simplified CCSD(T)-F12 methods: Theory and benchmarks. *J. Chem. Phys.* **130,** 054104 (2009).

33. Peterson, K. A., Adler, T. B. & Werner, H.-J. Systematically convergent basis sets for explicitly correlated wavefunctions: The atoms H, He, B–Ne, and Al–Ar. *J. Chem. Phys.* **128,** 084102 (2008).

34. Hill, J. G. & Peterson, K. A. Correlation consistent basis sets for explicitly correlated wavefunctions: Pseudopotential-based basis sets for the post-d main group elements Ga–Rn. *J. Chem. Phys.* **141,** 094106 (2014).

35. Peterson, K. A., Figgen, D., Goll, E., Stoll, H. & Dolg, M. Systematically convergent basis sets with relativistic pseudopotentials. II. Small-core pseudopotentials and correlation consistent basis sets for the post-d group 16–18 elements. *J. Chem. Phys.* **119,** 11113–11123 (2003).

36. Weigend, F. A fully direct RI-HF algorithm: Implementation, optimised auxiliary basis sets, demonstration of accuracy and efficiency. *Phys. Chem. Chem. Phys.* **4,** 4285–4291 (2002).

37. Weigend, F. Hartree–Fock exchange fitting basis sets for H to Rn †. *J. Comput. Chem.* **29,** 167–175 (2008).

38. Hättig, C. Optimization of auxiliary basis sets for RI-MP2 and RI-CC2 calculations: Core–valence and quintuple-ζ basis sets for H to Ar and QZVPP basis sets for Li to Kr. *Phys. Chem. Chem. Phys.* **7,** 59–66 (2005).

39. Valeev, E. F. Improving on the resolution of the identity in linear R12 ab initio theories. *Chemical Physics Letters* **395,** 190–195 (2004).

40. Yousaf, K. E. & Peterson, K. A. Optimized auxiliary basis sets for explicitly correlated methods. *J. Chem. Phys.* **129,** 184108 (2008).

41. Shiozaki, T., Knizia, G. & Werner, H.-J. Explicitly correlated multireference configuration interaction: MRCI-F12. *J. Chem. Phys.* **134,** 034113 (2011).

42. Shiozaki, T. & Werner, H.-J. Explicitly correlated multireference configuration interaction with multiple reference functions: Avoided crossings and conical intersections. *J. Chem. Phys.* **134,** 184104 (2011).

43. Davidson, E. R. & Silver, D. W. Size consistency in the dilute helium gas electronic structure. *Chemical Physics Letters* **52,** 403–406 (1977).

44. Shiozaki, T. & Werner, H.-J. Communication: Second-order multireference perturbation theory with explicit correlation: CASPT2-F12. *J. Chem. Phys.* **133,** 141103 (2010).

45. Peterson, K. A., Krause, C., Stoll, H., Hill, J. G. & Werner, H.-J. Application of explicitly correlated coupled-cluster methods to molecules containing post-3d main group elements. *Mol. Phys.* **109,** 2607–2623 (2011).

46. Dunning Jr., T. H. Gaussian basis sets for use in correlated molecular calculations. I. The atoms boron through neon and hydrogen. *J. Chem. Phys.* **90,** 1007–1023 (1989).

47. Werner, H.-J., Knowles, P. J., Knizia, G., Manby, F. R. & Schütz, M. Molpro: a general-purpose quantum chemistry program package. *Comput. Mol. Sci.* **2,** 242–253 (2012).

48. *MOLPRO, version 2012.1, a package of ab initio programs, H.-J. Werner, P. J. Knowles, G. Knizia, F. R. Manby, M. Schütz, P. Celani, T. Korona, R. Lindh, A. Mitrushenkov, G. Rauhut, K. R. Shamasundar, T. B. Adler, R. D. Amos, A. Bernhardsson, A. Berning, D. L. Cooper, M. J. O. Deegan, A. J. Dobbyn, F. Eckert, E. Goll, C. Hampel, A. Hesselmann, G. Hetzer, T. Hrenar, G. Jansen, C. Köppl, Y. Liu, A. W. Lloyd, R. A. Mata, A. J. May, S. J. McNicholas, W. Meyer, M. E. Mura, A. Nicklass, D. P. O'Neill, P. Palmieri, D. Peng, K. Pflüger, R. Pitzer, M. Reiher, T. Shiozaki, H. Stoll, A. J. Stone, R. Tarroni, T. Thorsteinsson, and M. Wang, , see http://www.molpro.net.*

49. Fan, H. & Pratt, S. T. Determination of Spin–Orbit Branching Fractions in the Photodissociation of Halogenated Hydrocarbons. *J. Phys. Chem. A* **111,** 3901–3906 (2007).

50. Gardiner, S. H., Lipciuc, M. L., Karsili, T. N. V., Ashfold, M. N. R. & Vallance, C. Dynamics of the A-band ultraviolet photodissociation of methyl iodide and ethyl iodide via velocity-map imaging with 'universal' detection. *Phys. Chem. Chem. Phys.* **17,** 4096–4106 (2015).

51. Bailleux, S. *et al.* Hyperfine Resolved Fourier Transform Microwave and Millimeter-Wave Spectroscopy of the Iodomethyl Radical, CH2I (X̃2B1). *J. Phys. Chem. A* **114,** 4776–4784 (2010).

52. Roberts, G. M., Nixon, J. L., Lecointre, J., Wrede, E. & Verlet, J. R. R. Toward real-time charged-particle image reconstruction using polar onion-peeling. *Rev. Sci. Instrum.* **80,** 053104–7 (2009).

53. Busch, G. E. & Wilson, K. R. Triatomic Photofragment Spectra. I. Energy Partitioning in NO2 Photodissociation. *J. Chem. Phys.* **56,** 3626 (1972).

54. Kisiel, Z., Pszczółkowski, L., Caminati, W. & Favero, P. G. First assignment of the rotational spectrum of a molecule containing two iodine nuclei: Spectroscopic constants and structure of CH_2I_2. *J. Chem. Phys.* **105,** 1778–1785 (1996).

55. Kwok, W. M. & Phillips, D. L. Gas and solution phase chloroiodomethane short-time photodissociation dynamics in the B-band absorption. *Chem. Phys. Lett.* **270,** 506–516 (1997).

56. Demyanenko, A. V., Dribinski, V., Reisler, H., Meyer, H. & Qian, C. X. W. Product quantum-state-dependent anisotropies in photoinitiated unimolecular decomposition. *J. Chem. Phys.* **111,** 7383–7396 (1999).

57. Liu, Y. *et al.* Photolysis of 1-C4H9I and 2-C4H9I at 266 nm: Direct Observation of the Effect of Branching on the Photodissociation Mechanism. *ChemPhysChem* **10,** 830–834 (2009).

58. Butler, L. J., Hintsa, E. J., Shane, S. F. & Lee, Y. T. The electronic state-selective photodissociation of CH_2BrI at 248, 210, and 193 nm. *J. Chem. Phys.* **86,** 2051–2074 (1987).

Table 3-1. Total available energy E_{AVL}, average translational energy $\langle E_T \rangle$, average CH_2I internal energy $\langle E_{INT} \rangle$, and E_T-averaged anisotropy parameters $\langle \beta \rangle$ obtained from analysis of ion images of I and I* atoms arising from CH_2I_2 photodissociation at several pump wavelengths.

λ_{pump} / nm	I				I*			
	E_{AVL} / eV	$\langle E_T \rangle$ / eV	$\langle E_{INT} \rangle$ / eV	$\langle \beta \rangle$	E_{AVL} / eV	$\langle E_T \rangle$ / eV	$\langle E_{INT} \rangle$ / eV	$\langle \beta \rangle$
248	2.844(11)	0.42(4)	2.42(4)	0.85(4)	1.902(5)	0.36(2)	1.55(2)	0.74(3)
266	2.506(10)	0.40(2)	2.10(2)	0.90(3)	1.563(4)	0.35(3)	1.21(3)	0.99(5)
280/282	2.278(9)	0.444(2)	1.83(1)	0.33(1)	1.304(4)	0.294(8)	1.01(1)	0.49(1)
304	1.927(7)	0.461(8)	1.47(1)	0.21(1)	0.981(3)	0.227(9)	0.75(1)	0.45(1)
355	1.338(5)	0.31(8)	1.03(8)	0.37(9)	0.395(1)	–	–	–

Table 3-2. Spin-orbit coupled (quadruple-zeta) vertical excitation energies (E–E_1), transition dipole moments (TDM) and major contributions to the spin-orbit eigenvectors at the equilibrium geometry.

State	Group	State number[a]	E–E_1 / eV	TDM / D	Major contributions (> 5%)		
X A$_1$ (X A′)		1	0.000		99% 1^{1}A$_1$		
1 B$_2$ (1 A″)	I	3	3.858	0.077	64% 1^{3}B$_2$	23% 1^{3}A$_2$	11% 2^{1}A$_1$
1 B$_1$ (3 A′)	I	5	4.136	0.346	82% 2^{1}A$_1$	10% 1^{3}B$_2$	
2 B$_1$ (4 A′)	I	7	4.207	0.643	69% 3^{1}A$_1$	14% 2^{3}B$_2$	9% 2^{3}A$_2$
3 A$_1$ (5 A′)	II	8	4.275	0.055	68% 3^{3}B$_1$	26% 2^{3}A$_2$	
2 B$_2$ (4 A″)	I	9	4.345	0.240	80% 2^{3}B$_2$	8% 3^{1}A$_1$	6% 2^{3}A$_2$
3 B$_1$ (7 A′)	III	12	4.617	0.641	48% 1^{3}A$_2$	35% 1^{1}B$_1$	17% 1^{3}A$_1$
4 B$_1$ (8 A′)	III	14	4.846	0.438	38% 1^{3}A$_1$	30% 1^{1}B$_1$	29% 1^{3}B$_2$
4 B$_2$ (8 A″)	III	16	4.990	0.374	62% 2^{1}B$_1$	37% 2^{3}A$_2$	
5 A$_1$ (9 A′)	IV	17	5.147	0.180	80% 2^{3}B$_1$	16% 3^{3}A$_1$	

[a] States 2, 10 and 11 (2 A$_1$, 3 B$_2$, and 4 A$_1$) have TDM < 0.05 D and are not listed. States 4, 6, 13, and 15 have A$_2$ symmetry.

4   Decomposing the First Absorption Band of OCS Using Photofragment

Excitation Spectroscopy
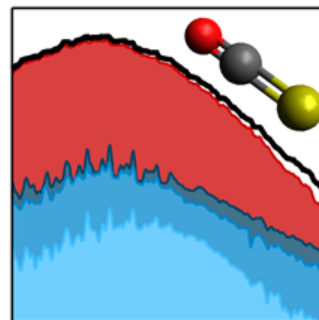
4.1 **Abstract**

Photofragment excitation spectra of carbonyl sulfide (OCS) have been recorded from 212–260 nm by state-selectively probing either electronically excited $S(^1D)$ or ground state $S(^3P)$ photolysis products via 2+1 resonance-enhanced multiphoton ionization. Probing the major $S(^1D)$ product results in a broad, unstructured action spectrum that reproduces the overall shape of the first absorption band. In contrast, spectra obtained probing $S(^3P)$ products display prominent resonances superimposed on a broad continuum; the resonances correspond to the diffuse vibrational structure observed in the conventional absorption spectrum. The vibrational structure is assigned to four progressions, each dominated by the C–S stretch, ν_1, following direct excitation to quasi-bound singlet and triplet states. The $S(^3P_J)$ products are formed with a near-statistical population distribution over the $J = 2$, 1 and 0 spin-orbit levels across the wavelength range investigated. Although a minor contributor to the S atom yield near the peak of the absorption cross section, the relative yield of $S(^3P)$ increases significantly at longer wavelengths. The experimental measurements validate recent theoretical work characterizing the electronic states responsible for the first absorption band by Schmidt and co-workers.

4.2 Introduction

Carbonyl sulfide (OCS) is the most abundant sulfur-containing compound in the atmosphere.[1] OCS is relatively unreactive in the troposphere, where it is present at near constant mixing ratios of ~500 ppt but concentrations drop off sharply in the stratosphere, as shorter wavelength photolysis becomes increasingly important.[2] As a source of atomic sulfur, photolysis of OCS makes a significant non-volcanic contribution to the stratospheric sulfate aerosol layer.[3,4] The first absorption band of OCS is responsible for its photochemistry in the stratospheric UV window and has been extensively studied.[5–16] The band appears as a broad, weak continuum spanning 190–260 nm and has diffuse vibrational structure superimposed. The diffuse structure was first observed by Breckenridge and Taube and assigned to four different progressions. One progression was identified as a hot band arising from bend-excited ground state molecules, which was later confirmed by Wu *et al.*[7,12] The red wing of the continuum absorption also depends strongly on temperature,[10,12,14–16] largely due to population in excited levels of the low frequency bend, ν_2, which significantly enhances the transition strength.[17] Additional diffuse structure has also been observed in the long wavelength tail of the absorption spectrum between 270–300 nm, where the cross section is around four orders of magnitude smaller than at the peak.[10]

The first absorption bands of OCS arise from (π,π^*) excitations and lead to $^{1,3}\Sigma^-$, $^{1,3}\Sigma^+$, and $^{1,3}\Delta$ states in linear geometries, while (σ,π^*) excitations lead to $^{1,3}\Pi$ states at higher energy.[18] The first absorption band primarily results from excitation to the $1^1\Delta$ and $1^1\Sigma^-$ states. Formally, electric dipole transitions to both states are forbidden in linear geometries because of the $\Delta\Lambda = \pm 1$ and $\Sigma^- \nleftrightarrow \Sigma^+$ selection rules. Bending deformation reduces the symmetry to C_s and splits the $1^1\Delta$ state into the $2^1A'$ and $2^1A''$ states, which form a Renner-Teller pair. The $1^1\Sigma^-$ state becomes the $1^1A''$ state and it has a bent minimum. All transitions are weakly allowed in C_s symmetry.

Several groups have performed electronic structure calculations to characterize the electronic structure, calculate the absorption spectrum and provide insight into the photodissociation dynamics.[17,19–25] Multi-reference configuration interaction (MRCI) calculations have shown that the $2^1A'$ ($1^1\Delta$) state predominantly and the $1^1A''$ ($1^1\Sigma^-$) state to a lesser extent are primarily responsible for the first absorption continuum.[17,20–22] In their more recent papers,[23,24] Schmidt and co-workers re-evaluated the transition dipole moment functions finding that the $1^1A''$ state made a significantly greater contribution to the absorption spectrum than previously thought. One-dimensional cuts through the potential energy surfaces along the Jacobi coordinate defining the distance between the S atom and the center of mass of the CO molecule are depicted in Figure 4-1. Other key characteristics of the states are summarized in Table 4-1. The topographies of the $2^1A'$ and $1^1A''$ states are very similar. Both are highly repulsive along the C–S bond in near-linear geometries, but have minima in bent geometries that lie below the $S(^1D)$ + CO product asymptote. These potential wells can support bound states and are responsible for the structure in the long-wavelength tail of the absorption band.[10,22] The diffuse vibrational structure near the peak of the absorption band was attributed to transitions to the bound $2^3A''$ ($1^3\Sigma^-$) state, which acquires transition strength via spin-orbit coupling to the strongly absorbing and near-degenerate $2^1A'$ state.[17,20–22] Inclusion of higher order correlation effects in the electronic structure calculations critically influence the potential energy surfaces (PESs) and transition dipole moment functions.[25]
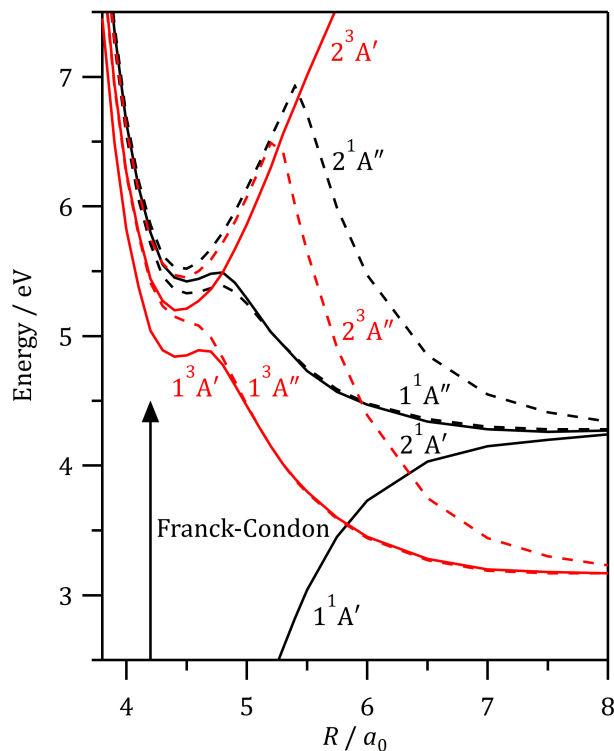
Figure 4-1. One-dimensional cuts along the Jacobi coordinate R for the lowest singlet (black) and triplet (red) states for $r = 2.2\ a_0$ and $\gamma = 5°$. Solid and dashed lines indicate states of A′ and A″ symmetry, respectively. Adapted from Schmidt *et al.* [*J. Chem. Phys.* 2012, *137* (5), 54313].

It has long been known[26] that excitation of OCS in the first absorption band leads to dissociation to form CO + S and the photodissociation dynamics has received significant attention.[20,27–40] Various groups have attempted to quantify the photodissociation quantum yield, Φ.[5,6,9,41] Although the earliest measurements, reported $\Phi \approx 1$, others suggested smaller values when probing the yield of CO.[6,9] The secondary reaction S + OCS → S_2 + CO was assumed to go to completion, leading to an anticipated total CO quantum yield of $\Phi = 2$. The current JPL evaluation[42] recommends a primary CO quantum yield of unity across the 220–254 nm wavelength range, based primarily on the tunable diode laser absorption measurements made by Zhao *et al.* probing CO concentration after photolysis at 248 nm.[41] Sulfur atoms are formed predominantly in the electronically excited [1]D state with a far smaller fraction produced in the [3]P ground state. Early measurements of the

branching between singlet and triplet S atom photoproducts inferred that S(^{1}D) accounted for around 75% of the total atomic sulfur yield,[6,43] although measurements in collisional environments were complicated by quenching. Two-photon LIF measurements by van Veen *et al.* probed the time-dependent formation of S(^{3}P) and S(^{1}D) atoms following photolysis at 248 nm.[44] While S(^{1}D) atoms were detected promptly, the S(^{3}P) fluorescence signal grew in over a millisecond timescale. However, the experiments lacked sufficient time resolution to demonstrate exclusive production of S(^{1}D). Sivakumar *et al.* suggested a S(^{3}P) branching fraction of 0.15 after 222 nm excitation, but subsequently revised this to <0.02.[27,28] Doppler profile measurements by Nan *et al.* using VUV laser induced fluorescence at a photolysis wavelength of 222 nm demonstrated the direct formation of S(^{3}P$_2$) radicals with a S(^{3}P$_2$)/S(^{1}D) branching ratio of 0.05.[29] Fully state-resolved velocity-map imaging measurements at 230 nm probed CO(J = 63) products and determined a S(^{3}P$_2$)/S(^{1}D) branching ratio of 0.038, consistent with the rotationally averaged result.[37]

In this work, photofragment excitation (PHOFEX) spectroscopy has been used to record action spectra of the first absorption band of OCS while probing ground state S(^{3}P$_J$) and electronically excited S(^{1}D) atoms by 2+1 resonance enhanced multiphoton ionization. The PHOFEX spectra are structureless when probing S(^{1}D) atoms, but show resonances corresponding to vibrational progressions in two different bound electronic states when probing S(^{3}P$_J$) atoms. The wavelength-dependence of the ground state fine-structure branching and the overall singlet-triplet branching fractions are determined.

4.3 Experimental methods

PHOFEX spectra were recorded in a velocity-map ion imaging mass spectrometer, previously described in detail.[45] In these experiments, however, it was operated as a conventional Wiley-McLaren time-of-flight mass spectrometer. Dilute mixtures of OCS (Matheson, >97% purity) in Ar

or He carrier gas were expanded into high vacuum from a stagnation pressure of 1 atm using a solenoid pulsed valve (Parker Series 9). The expansion was skimmed (Beam Dynamics) to form a molecular beam before being intersected by counter-propagating pump and probe laser beams that dissociated OCS and state-selectively ionized $S(^1D)$ or $S(^3P_J)$ products via well-known 2+1 resonance-enhanced multiphoton ionization (REMPI) transitions. Pump laser pulses spanning the 212–260 nm wavelength range were generated using a mid-band Nd:YAG-pumped optical parametric oscillator (OPO) (Continuum Surelite EX and Horizon II). The OPO generated a broadly tunable UV beam with a linewidth of 5–7 cm^{-1}. The pulse energy increased from 0.5 to 1.1 mJ across the scanned range. A frequency doubled Nd:YAG-pumped dye laser (Continuum Surelite II–10, Lambda Physik Scanmate) operating with Rhodamine 590 or 640 laser dyes generated the REMPI probe pulses with typical pulse energies of <1.5 mJ. The pump and probe beams, temporally separated by < 30 ns, were focused into the ionization region of the mass spectrometer with fused silica lenses of focal lengths f = 1000 mm and 300 mm, respectively. A stack of electrodes accelerates the resultant ions towards a time-gated MCP/phosphor assembly (Photonis).

The phosphorescence corresponding to selected features in the mass spectrum was monitored as a function of pump wavelength by a silicon photomultiplier (SenSL MicroSL 10020–X18) to generate PHOFEX spectra. Pump and probe laser pulse energies were monitored with a photodiode (Thorlabs DET10a) that had been calibrated against an energy meter (Gentec Maestro). Optogalvanic Ne spectra were recorded simultaneously using the visible OPO signal beam and calibrated against known line positions in PGOPHER.[46] A small wavelength offset provided satisfactory agreement across the entire spectral range with a standard deviation between the observed and reference line positions of < 3 cm^{-1}, indicating good scanning linearity. All signals were digitized by an oscilloscope (LeCroy HDO4054) interfaced to a data acquisition PC running custom written software (National Instruments LabVIEW).

4.4 **Results and Discussion**

PHOFEX action spectra of OCS were recorded by repeatedly scanning the pump wavelength from 212 nm to 260 nm, while monitoring the total $m/z = 32$ (S^+) signal with the probe laser wavelength tuned to be resonant with a known 2+1 REMPI transition of sulfur atoms. On its own, the pump laser induced background signals when tuned over sharp two-photon resonances of atomic sulfur. A weaker, broad background S^+ signal also appeared at pump wavelengths < 225 nm. This signal coincided with the observation of the OCS^+ parent ion at $m/z = 60$ and was attributed to dissociative ionization. The probe laser was held fixed at 288.17 nm to ionize $S(^1D)$ atoms via the $3p^34p$ $^1F_3$ level. $S(^3P_J)$ atoms were ionized via the $3p^34p$ ^3P_J levels at one-photon wavelengths of 308.20 nm, 310.09 nm and 310.96 nm, which probed the $J = 2,1$, and 0 levels, respectively. The trace amount of CS_2 present as a contaminant in the OCS sample (<0.2%) makes no significant contribution to the PHOFEX spectra in the wavelength range studied.

The PHOFEX spectrum of OCS obtained probing electronically-excited $S(^1D)$ atoms is shown in Figure 4-2. Background signal induced by the pump laser alone has been subtracted and the spectrum has been normalized for the wavelength-dependence of the pump laser power. The spectrum reproduces the overall shape of the absorption spectrum reasonably well, although some differences are evident. First, the diffuse vibrational structure in the absorption spectra is absent from the $S(^1D)$ action spectrum. Second, despite cooling in the supersonic expansion, the long-wavelength (λ > 235 nm) region of the PHOFEX spectrum is more similar to the absorption spectrum measured at 295 K than 170 K.[12] The maximum $S(^1D)$ yield appears red-shifted by ~2 nm relative to the maxima of the absorption spectra.
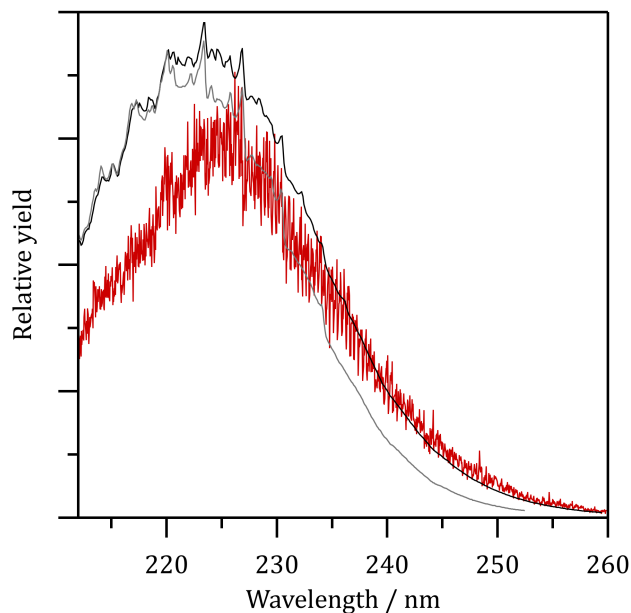
Figure 4-2. OCS PHOFEX spectrum recorded probing S(^{1}D) products via 2+1 REMPI at 288 nm (red). Conventional absorption spectra measured by Wu *et al.* [*J. Quant. Spectrosc. Rad. Trans.* 1999, *61* (2), 265] at 295 K (black) and 170 K (gray) are also shown.

Several groups have investigated the temperature-dependence of the absorption spectrum, finding that excitation in ν_2 in the ground electronic state is responsible for absorption in the red wing of the band.[10–12,16] Low frequency vibrational excitation, which greatly enhances the absorption cross section, appears not to be effectively relaxed in the expansion, as has been observed previously in ion imaging experiments.[36] Third, the relative S(^{1}D) yield measured in the PHOFEX spectrum deviates from the conventional absorption spectrum at shorter wavelengths ($\lambda < 225$ nm), where the absorption band is least affected by the temperature. The dissociation threshold to form CO + S(^{1}S) does not become energetically accessible until $\lambda < 211$ nm and the S(^{3}P) yield, described below, is too small to compensate for the apparent deviation between the S(^{1}D) yield and the OCS absorption spectrum. The deviation does coincide, however, with the appearance of OCS$^+$ and S$^+$ peaks in the mass spectrum induced by the pump laser alone. Multiphoton dissociative ionization likely competes with neutral dissociation at the typical pump energies used in the experiment,

reducing the apparent yield of neutral sulfur atoms in this wavelength range.

The action spectrum presented in Figure 2 differs somewhat from that measured previously by Suzuki *et al.*, who found a relatively smaller S(^{1}D) yield at longer wavelengths, although the Feshbach resonances predicted in the wavepacket calculations are not observed in our spectrum either.[20] The absence of structure in the PHOFEX spectrum is consistent with the theoretical view that the absorption spectrum is dominated by excitation to the repulsive 2^1A$'$ and 1^1A$''$ states.[17,22,23] The measurements reported here do not distinguish the relative contributions of each state to the S(^{1}D) yield, although previous measurements of the photofragment angular distributions indicate that both contribute significantly.[20,34,47]

In contrast to S(^{1}D), the equivalent PHOFEX spectra recorded when state-selectively probing S(^{3}P$_J$) atoms show distinct resonances superimposed on a similar broad continuum; pump-only background subtracted and pump power normalized spectra are shown in Figure 4-3. Aside from the relative yield of each S(^{3}P$_J$) spin-orbit level, the triplet PHOFEX spectra are qualitatively similar. The relative population in each spin-orbit level can be obtained directly from the REMPI signal intensity, since the line strengths for the transitions used to probe the J = 0, 1, and 2 spin-orbit levels are almost identical.[48,49] A correction is applied to account for incomplete sampling of the total REMPI spectrum at the fixed probe wavelengths. Each nominal transition probing S(^{3}P$_J$) comprises two or three partially resolved spectral lines due to the small spin-orbit splitting in the resonant electronically excited state.   Figure 4-4 shows S atom REMPI spectra following photodissociation of OCS at 225 nm. The fractional contribution made to the total REMPI signal at each fixed probe wavelength was used to scale the PHOFEX spectra in Figure 4-3 such that the intensity is proportional to the yield. The J = 2 spin-orbit level is the major triplet product, with progressively smaller yields of J = 1 and J = 0. The resonances account for <10% of the total S(^{3}P)

yield: the underlying continuum absorption is predominantly responsible for the production of S(^{3}P) atoms.
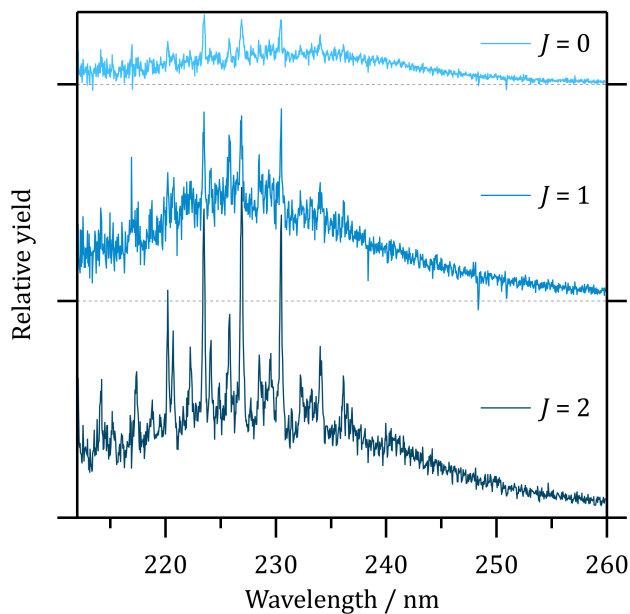
Figure 4-3. OCS PHOFEX spectra recorded probing S(^{3}P$_J$) products via 2+1 REMPI at wavelengths spanning 308–311 nm.
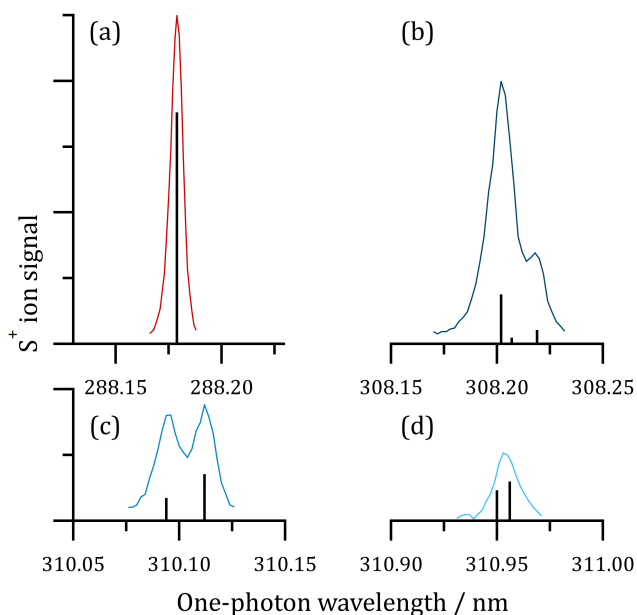
Figure 4-4. 2+1 REMPI spectra of (a) S(^{1}D); (b) S(^{3}P$_2$); (c) S(^{3}P$_1$); and (d) S(^{3}P$_0$) atoms arising from the photolysis of OCS at 225 nm. Sticks indicate the positions and relative intensities of the transitions.

The transition dipole moments for direct spin-forbidden excitation to the lowest dissociative triplet states, $1^3A'$ ($1^3\Sigma^+$) and $1^3A''$ ($1^3\Delta$), are likely too small to account for the S(^{3}P) yield.[17,22] We note, however, that revised transition dipole moments for these states were not reported in a more recent paper that identified problems with the calculations.[23] It seems likely, therefore, that the continuum observed in the triplet PHOFEX spectra results primarily from initial excitation to the repulsive $2^1A'$ or $1^1A''$ states, although intersystem crossing must occur to yield S(^{3}P) products. The continua in the triplet and singlet PHOFEX spectra have very similar shapes, suggesting the same underlying electronically excited states are primarily responsible. The dissociative $2^1A'$ and $1^1A''$ states are likely too short-lived for intersystem crossing in the Franck-Condon region to be important. One-dimensional cuts through the PESs (see Figure 4-1) show that the bound $2^3A''$ state becomes repulsive at longer range (Jacobi coordinate, $R > 5.2$ a_0) in linear geometries as a result of an avoided crossing with an unidentified repulsive surface (likely $^3\Sigma^-$), and the outer limb crosses both the repulsive $2^1A'$ and $1^1A''$ singlet surfaces. Alternatively, the products could be formed on the repulsive $1^3A''$ state, which lies very close in energy to the $2^1A'/1^1A'$ exit channel conical intersection at bend angles of ~60°.

The wavelength-dependence of the spin-orbit population distributions are more clearly observed in Figure 4-5, which shows the fractional contributions of each level to the total S(^{3}P) yield. Across the absorption band, the fractional populations in the $J = 2$, 1, and 0 spin-orbit levels are broadly at the ($2J + 1$) statistical limit (i.e. 5:3:1), albeit with some subtle deviations. First, the resonances appear distinctly in Figure 5 as peaks in the fractional population in the $J = 2$ level and dips in $J = 1$. The fractional yield of the $J = 0$ level appears to be unaffected by the resonances. Second, a slight reduction in the fractional $J = 2$ population across the center of the absorption band is compensated by local increases in $J = 1$, centered near 226 nm, and $J = 0$, centered near 238 nm. The wavelength-dependent enhancements in the fractional $J = 1$ and $J = 0$ populations match well the predicted

absorption spectra for excitation to the repulsive $1^1A''$ ($1^1\Sigma^-$) and $1^3A''$ ($1^3\Delta$) states, respectively.[17]
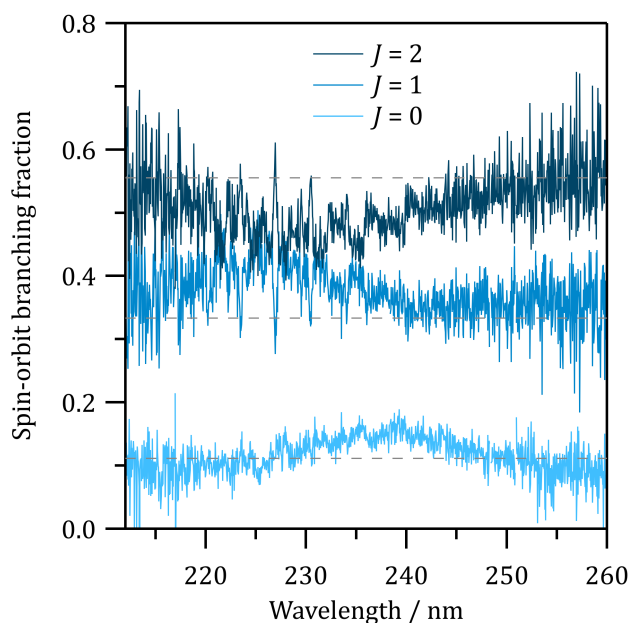
Figure 4-5. Spin-orbit branching fractions among $S(^3P_J)$ products. The dashed horizontal lines indicate the statistical limits.

It is not clear, however, why initial excitation to the $1^1A''$ and $1^3A''$ states would result in an increased propensity for production of $S(^3P_1)$ and $S(^3P_0)$, respectively. Brouard *et al.* identified an additional translationally fast (i.e. low-J' CO) component in $S(^3P_0)$ ion images that was not present for $S(^3P_2)$ or $S(^3P_1)$ at a photolysis wavelength of 248 nm.[39] The spin-orbit branching was also found to be weighted even more heavily in favor of the $J = 2$ level at 248 nm. While it is possible that the fast component could arise from direct excitation to the repulsive $1^3A''$ state, one-dimensional cuts through the PES suggest that it is highly anisotropic, which would lead to rotationally excited CO co-products.[23] The adiabatic model discussed by Brouard *et al.* shows that $S(^3P_0)$ does not correlate with the $1^3A''$ state, but rather to the higher-lying bound $2^3A''$ ($1^3\Sigma^-$) state in both bent and linear geometries. A more detailed understanding of the photodissociation mechanism is likely to require further theoretical work, in particular, calculation of the fully spin-

orbit coupled PESs.

The wavelengths and relative intensities of the resonances in the triplet PHOFEX spectra shown in Figure 3 reproduce the diffuse vibrational structure observed in conventional absorption measurements and indicate excitation to bound, or rather quasi-bound, states. Dissociation to form $S(^3P)$ + CO must be faster than the timescale of the experiment i.e. < 30 ns, the time delay between the pump and probe laser pulses, to produce the action spectrum. Prompt predissociation is also supported by anisotropy in the photofragment angular distributions.[39] Figure 4-6 shows a higher resolution OCS PHOFEX spectrum of the structured region between 216 nm and 238 nm that was obtained probing $S(^3P_2)$ products. Lorentzian functions were used to fit the resonances and obtain band centers and relative intensities, which are summarized in Table 4-2. The resonances in progression I all have FWHM of $\sim$50 cm^{-1}, significantly broader than the OPO bandwidth of $\sim$7 cm^{-1}. PGOPHER simulations suggest that the rotational contour of each band would be expected to span only $\sim$10 cm^{-1} at 30 K, the estimated temperature of the molecular beam. The resonances are sharper in the PHOFEX spectrum than in conventional absorption spectra, where unresolved rotational structure will contribute to the width. Assuming that homogeneous lifetime broadening is responsible for the width of the resonances, the lifetimes of the quasi-bound excited states are expected to be $\sim$100 fs. The resonances dissociate exclusively to form $S(^3P)$ products – no structure is identifiable within our signal-to-noise in the PHOFEX spectrum when probing $S(^1D)$.
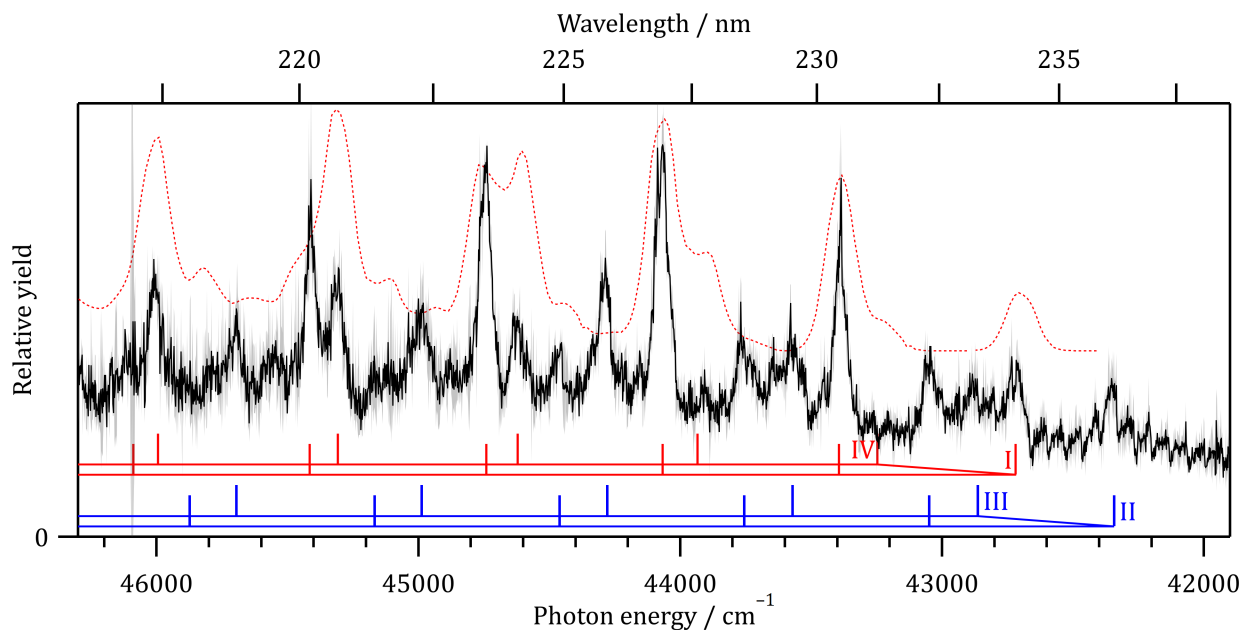
Figure 4-6. High-resolution PHOFEX spectrum of OCS probing $S(^3P_2)$ atoms. Progressions I and IV (red comb) are assigned to $n\nu_1$ and $n\nu_1+2\nu_2$ in the $2^3A''$ ($1^3\Sigma^-$) state.   Progressions II and III (blue combs) are assigned to $n\nu_1$ in the $2^1A''$ ($1^1\Delta$) state, the former originating from bend excited ground state molecules.   The predicted absorption spectrum for excitation to the $2^3A''$ ($1^3\Delta$) state from Schmidt *et al.* [*J. Chem. Phys.* 2012, *137* (5), 54313] is also shown, offset by 3 nm (dashed red).

Previously, Hishikawa *et al*. measured PHOFEX spectra of the $2^1\Sigma^+-1^1\Sigma^+$ transition in the vacuum ultraviolet region (144–158 nm), probing electronically excited $S(^1S)$ atoms by laser-induced fluorescence.[50]   A vibrational progression was observed with spacing of ~800 cm^{-1}. Across the progression, the peaks had varying Lorentzian linewidths and asymmetric Fano lineshapes,[51] that furthermore displayed a reversal in the q parameter. In contrast to the $2^3A''$ state, which is bound, the electronically excited $2^1\Sigma^+$ state is purely dissociative along the C–S coordinate, but features a broad plateau associated with C–O bond extension.   Wavepacket calculations allowed the progression to be assigned to transient Feshbach resonance states associated with in-phase C–O and C–S stretching motion, that is, motion perpendicular to the dissociation coordinate.   The resonances observed in the PHOFEX spectrum probing $S(^3P)$ shown in Figure 4-6, have a different

99

physical origin, arising from excitation to a bound state, and do not display any variation in linewidth or evidence of asymmetric Fano lineshapes.

The diffuse vibrational structure in the conventional absorption spectrum has been assigned to four progressions (labeled here as I–IV), one of which was found to be a hot band arising from bend-excited ground state molecules.[7,12] The four strongest transitions in the spectrum shown in Figure 4-6 are evenly spaced and identified as progression I. The weak feature at 234.09 nm (42719 cm^{-1}) also appears to be associated with this progression and is presumed to be the origin band. The average separation of 673±7 cm^{-1} is close to the predicted harmonic C–S stretch (ν_1) frequency in the bound $2^3A''$ ($1^3\Sigma^-$) state of 688 cm^{-1}. The positions and intensities are in excellent agreement with the calculated spectrum for direct excitation to the bound $2^3A''$ ($1^3\Sigma^-$) state, which also is shown in Figure 6, offset by 3 nm.[17]

The transition to the $2^3A''$ state gains intensity through spin-orbit coupling with the neighboring $2^1A'$ state and it is predicted to undergo electronic predissociation by recoupling with a lifetime of ~300 fs.[24] The calculated lifetime is in reasonable agreement with the ~100 fs lifetime estimated from the homogeneous broadening of the resonances. Once on the $2^1A'$ state, dissociation could proceed as described for the continuum S(^3P) yield as described above. However, this mechanism would suggest that the vibrational resonances should be present in the PHOFEX spectrum obtained probing S(^1D), since some fraction of the molecules that began on the $2^3A''$ surface would not undergo the second transition required to reach triplet products. The relative yields of S(^1D) and S(^3P) suggest that the likelihood of forming triplet products starting from the repulsive singlet surfaces is small. Since the S(^1D) yield is dominated by direct excitation to the $2^1A'$ and $1^1A''$ surfaces, the signature of the resonances may be lost in the noise. Alternative interpretations are that the dissociation occurs exclusively within the triplet system. The $2^3A''$ state could

predissociate by tunneling through the barrier to form S(^{3}P), although inspection of the potential energy surface does not show any geometries for which the barrier is lower than ~1 eV. A tunneling mechanism may be expected to lead to a decrease in the excited state lifetime following excitation to bound states higher in the $2^3A''$ well. While the range of excitation energies is somewhat limited, no variation in the homogeneous broadening is observed. The bound $2^3A''$ state can interact with the dissociative $1^3A''$ state via nonadiabatic coupling, although the strength of this interaction is not known and the states remain reasonably well separated in the Franck-Condon region. Elucidating the details of the dissociation mechanism will require additional experimental and theoretical work.

The weak and longest wavelength feature at 236.12 nm (42352 cm^{-1}) was previously assigned to a hot band[7,12] and is the first member of progression II with average separations of 705±11 cm^{-1}, which is also close to that expected for ν_1. All of the bands in progression II match those identified as hot bands in temperature-dependent measurements of the absorption cross section,[7,12] where the hot bands were significantly reduced in intensity. The –367 cm^{-1} offset from the first member of progression I, however, is inconsistent with the frequency of 520 cm^{-1} for the bending vibration, ν_2, in the electronic ground state.[52] A third progression (labeled III) with an effectively identical average separation of 708±9 cm^{-1} and origin at 233.27 nm (42868 cm^{-1}) can also be identified. Progression III is red-shifted by 516±9 cm^{-1} from the first band in progression II, consistent with the frequency of ν_2 in the ground state. The slight increase in the average separation of the bands and small 149 cm^{-1} shift of the apparent origin band relative to progression I suggests that progressions II and III involve excitation to a different quasi-bound and near degenerate electronic state.

The $2^1A''$ ($1^1\Delta$) and $2^3A'$ ($1^3\Delta$) states, which are the Renner-Teller partners of the $2^1A'$ and $1^3A''$ states, are also predicted to be bound.[17,22-24] Progressions II and III are unlikely to be attributable to the $2^3A'$ state for two reasons. First, the transition dipole moment was calculated to be an order of magnitude smaller than that of the $2^3A''$ state, albeit with the caveat that these values come from the earlier work of Schmidt *et al.* and were not updated using the improved methods reported in McBane *et al.*[23] Secondly, the predicted absorption spectrum appears to be significantly broader, with structure extending to longer wavelengths. Excitation to the $2^1A''$ state on the other hand is predicted to have a transition dipole moment of comparable magnitude and lie much closer in energy to the $2^3A''$ state. The bound $2^1A''$ state can dissociate by nonadiabatic coupling to the dissociative $1^1A''$ state, but this pathway would lead to predominantly singlet products. Intersystem crossing to the $2^3A''$ state, which is nearly degenerate could lead to dissociation within the triplet system via the mechanisms suggested above.

The remaining bands in the spectrum are relatively intense and form progression IV with a characteristic spacing of 686 ± 12 cm^{-1}, similar to that observed for progression I. The first band in this progression lies at 224.11 nm (44621 cm^{-1}), which corresponds to an offset of $+1902$ cm^{-1} from the origin band of progression I. The C–O stretch, ν_3, is predicted to have a frequency of only 1711 cm^{-1} in the $2^3A''$ state and a possible assignment to $n\nu_2+\nu_3$ is rejected.[17] The average peak separation suggests additional bands should be observable near 227.6 nm and 231.2 nm; the latter would be offset from the origin band by 539 cm^{-1}, which is close to the predicted wavenumber of 522 cm^{-1} for two quanta of ν_2 in the $2^3A''$ state and suggests an assignment to a combination band $n\nu_1+2\nu_2$.[17] Reassuringly, a very weak band is indeed visible in the PHOFEX spectrum at 227.7 nm but the predicted longest wavelength band is not observed, presumably on Franck-Condon overlap grounds.

The $n\nu_1$ and combination band $n\nu_1+2\nu_2$ vibrational progressions (I and IV) associated with the $2^3A''$ state have different C–S stretch frequencies, indicating that coupling between the C–S stretch and the bend occurs. Anharmonic coupling constants are extracted by fitting the progressions to an anharmonic oscillator expression:

$$E'_v = \left(v_1+\frac{1}{2}\right)\omega_1 + \left(v_2+\frac{1}{2}\right)\omega_2 + \left(v_1+\frac{1}{2}\right)^2 x_{11} + \left(v_2+\frac{1}{2}\right)^2 x_{22} + \left(v_1+\frac{1}{2}\right)\left(v_2+\frac{1}{2}\right)x_{12}$$
$$-\frac{\omega_1+\omega_2}{2} - \frac{x_{11}+x_{22}+x_{12}}{4}$$

E'_v is the vibrational energy in cm^{-1} above that of the electronic origin, which is assumed to be 42719 cm^{-1}, the position of the first identified band in progression I. ω_1 and ω_2 are the zero-order frequencies of the C–S stretch and bend, while x_{ii} and x_{ij} are the diagonal and off-diagonal anharmonicity constants. No significant progression is observed in the bend and consequently x_{22} is held at zero. Spectroscopic constants derived from the fit are summarized in Table 4-3. The average deviation between the fit and the experimental peak positions is < 5 cm^{-1}.

Finally, we turn to the wavelength-dependence of the quantum yield of S(^{3}P). The REMPI detection sensitivity of S(^{1}D) relative S(^{3}P) is unknown and must be characterized. S atom REMPI spectra, equivalent to those shown in Figure 4, were recorded at a photolysis wavelength of 222 nm. After normalization for variations in pump and probe fluences the S(^{1}D) signal was approximately 61 times greater than that of S(^{3}P$_2$). Using the ^{3}P$_2$/^{1}D$_2$ branching ratio of 0.05 at 222 nm measured by Nan *et al.*,[29] the relative REMPI detection sensitivity for S(^{1}D) is 3.1±0.8 times that of S(^{3}P$_2$). The PHOFEX spectra can be used to estimate the wavelength-dependence of the S(^{3}P) product yield, as shown in Figure 4-7. Enhanced production of S(^{3}P) is observed when the wavelength coincides

with the vibrational progressions observed in the OCS absorption and PHOFEX spectra. At wavelengths <230 nm, the S(^{3}P) quantum yield is consistently around 0.1, but increases steadily with increasing wavelength. Hot bands arising from residual vibrationally excited OCS molecules in the ground electronic state may affect this trend.
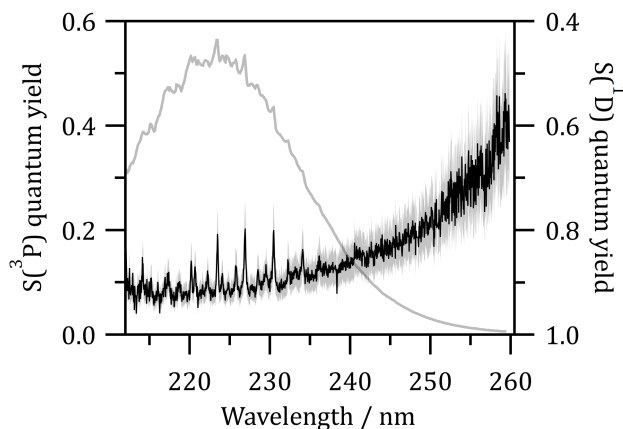
Figure 4-7. Wavelength dependence of the S(^{3}P) and S(^{1}D) photolysis quantum yields (black) and the OCS absorption cross section measured by Wu *et al.* [*J. Quant. Spectrosc. Rad. Trans.* 1999, *61* (2), 265] at 295 K (gray). A total photolysis quantum yield of unity is assumed.

4.5 **Conclusions**

Photofragment excitation action spectroscopy has been used to decompose the first absorption band of OCS. The PHOFEX spectrum obtained probing the major S(^{1}D) products is consistent with the prompt dissociation following excitation to the repulsive $2^1A'$ ($1^1\Delta$) and $1^1A''$ ($1^1\Sigma^-$) states, which dominate the absorption spectrum. In contrast, PHOFEX spectra obtained probing S(^{3}P) products display prominent resonances superimposed on a broad continuum. The resonances correspond to the diffuse vibrational structure observed in the conventional absorption spectrum and can be assigned to progressions in the C–S stretch, following direct excitation to the quasi-

bound $2^3A''$ ($1^3\Sigma^-$) and $2^1A''$ ($1^1\Delta$) states. These states have been predicted to rapidly predissociate via spin-orbit coupling to the $2^1A'$ ($1^1\Delta$) state or nonadiabatic transitions to the $1^1A''$ ($1^1\Sigma^-$) states, respectively, although subsequent intersystem crossing would be required to form S(^{3}P) products. Alternative mechanisms for dissociation within the triplet system may involve nonadiabatic transitions between the bound $2^3A''$ state and the repulsive $1^3A''$ state; further experimental and theoretical work is needed to clarify the detailed photodissociation mechanism. Direct absorption to the dissociative $1^3A''$ ($1^3\Delta$) state may contribute near the red-edge of the band, leading to changes in the spin-orbit branching and an increase in relative importance of S(^{3}P) products.

4.6   Acknowledgements

4.7   References

1.   Watts, S. F. The Mass Budgets of Carbonyl Sulfide, Dimethyl Sulfide, Carbon Disulfide and Hydrogen Sulfide. *Atmos. Environ.* **2000**, *34* (5), 761–779.
2.   Chin, M.; Davis, D. D. A Reanalysis of Carbonyl Sulfide as a Source of Stratospheric Background Sulfur Aerosol. *J. Geophys. Res.* **1995**, *100* (D5), 8993–9005.
3.   Crutzen, P. J. The Possible Importance of CSO for the Sulfate Layer of the Stratosphere. *Geophys. Res. Lett.* **1976**, *3* (2), 73–76.
4.   Brühl, C.; Lelieveld, J.; Crutzen, P. J.; Tost, H. The Role of Carbonyl Sulphide as a Source of Stratospheric Sulphate Aerosol and Its Impact on Climate. *Atmos. Chem. Phys.* **2012**, *12* (3), 1239–1253.
5.   Forbes, G. S.; Cline, J. E. The Photolysis and Extinction Coefficients of Gaseous Carbonyl Sulfide. *J. Am. Chem. Soc.* **1939**, *61* (1), 151–154.
6.   Sidhu, K. S.; Csizmadia, I. G.; Strausz, O. P.; Gunning, H. E. The Reactions of Sulfur Atoms. VII. The Ultraviolet Spectrum, the Photolysis, and the Mercury Sensitization of Carbonyl Sulfide. *J. Am. Chem. Soc.* **1966**, *88* (11), 2412–2417.
7.   Breckenridge, W. H.; Taube, H. Ultraviolet Absorption Spectrum of Carbonyl Sulfide. *J. Chem. Phys.* **1970**, *52* (4), 1713–1715.
8.   Ferro, B. M.; Reuben, B. G. Temperature Dependence of Absorption Spectrum of Carbonyl Sulphide in Quartz Ultra-Violet. *Trans. Faraday Soc.* **1971**, *67* (0), 2847–2851.

9. Rudolph, R. N.; Inn, E. C. Y. OCS Photolysis and Absorption in the 200- to 300-nm Region. *J. Geophys. Res.* **1981**, *86* (C10), 9891–9894.

10. Molina, L. T.; Lamb, J. J.; Molina, M. J. Temperature Dependent UV Absorption Cross Sections for Carbonyl Sulfide. *Geophys. Res. Lett.* **1981**, *8* (9), 1008–1011.

11. Locker, J. R.; Burkholder, J. B.; Bair, E. J.; Webster, H. A. Thermally Excited Vibrational Components of the A ← X$^1\Sigma^+$ System of Carbonyl Sulfide. *J. Phys. Chem.* **1983**, *87* (11), 1864–1868.

12. Wu, C. Y. R.; Chen, F. Z.; Judge, D. L. Temperature-Dependent Photoabsorption Cross Sections of OCS in the 2000–2600 Å Region. *J. Quant. Spectrosc. Rad. Trans.* **1999**, *61* (2), 265–271.

13. Colussi, A. J.; Leung, F.; Hoffmann, M. R. Electronic Spectra of Carbonyl Sulfide Sulfur Isotopologues. *Environ. Chem.* **2004**, *1* (1), 44–48.

14. Hattori, S.; Danielache, S. O.; Johnson, M. S.; Schmidt, J. A.; Kjaergaard, H. G.; Toyoda, S.; Ueno, Y.; Yoshida, N. Ultraviolet Absorption Cross Sections of Carbonyl Sulfide Isotopologues OC^{32}S, OC^{33}S, OC^{34}S and O^{13}CS: Isotopic Fractionation in Photolysis and Atmospheric Implications. *Atmospheric Chemistry and Physics* **2011**, *11* (19), 10293–10303.

15. Limão-Vieira, P.; Silva, F. F. da; Almeida, D.; Hoshino, M.; Tanaka, H.; Mogi, D.; Tanioka, T.; Mason, N. J.; Hoffmann, S. V.; Hubin-Franskin, M.-J.; et al. Electronic Excitation of Carbonyl Sulphide (COS) by High-Resolution Vacuum Ultraviolet Photoabsorption and Electron-Impact Spectroscopy in the Energy Region from 4 to 11 eV. *J. Chem. Phys.* **2015**, *142* (6), 64303.

16. Grosch, H.; Fateev, A.; Clausen, S. UV Absorption Cross-Sections of Selected Sulfur-Containing Compounds at Temperatures up to 500 °C. *J. Quant. Spectrosc. Rad. Trans.* **2015**, *154*, 28–34.

17. Schmidt, J. A.; Johnson, M. S.; McBane, G. C.; Schinke, R. The Ultraviolet Spectrum of OCS from First Principles: Electronic Transitions, Vibrational Structure and Temperature Dependence. *J. Chem. Phys.* **2012**, *137* (5), 54313.

18. Rabalais, J. W.; McDonald, J. R.; Scherr, V. M.; McGlynn, S. P. Electronic Spectroscopy of Isoelectronic Molecules. II. Linear Triatomic Groupings Containing Sixteen Valence Electrons. *Chem. Rev.* **1971**, *71* (1), 73–108.

19. Clementi, E. Ground State SCF-LCAO-MO Wave Function for the Carbonyl Sulfide Molecule. *J. Chem. Phys.* **1962**, *36* (3), 750–752.

20. Suzuki, T.; Katayanagi, H.; Nanbu, S.; Aoyagi, M. Nonadiabatic Bending Dissociation in 16 Valence Electron System OCS. *J. Chem. Phys.* **1998**, *109* (14), 5778–5794.

21. Danielache, S. O.; Nanbu, S.; Eskebjerg, C.; Johnson, M. S.; Yoshida, N. Carbonyl Sulfide Isotopologues: Ultraviolet Absorption Cross Sections and Stratospheric Photolysis. *J. Chem. Phys.* **2009**, *131* (2), 24307.

22. Schmidt, J. A.; Johnson, M. S.; McBane, G. C.; Schinke, R. Communication: Multi-State Analysis of the OCS Ultraviolet Absorption Including Vibrational Structure. *J. Chem. Phys.* **2012**, *136* (13), 131101.

23. McBane, G. C.; Schmidt, J. A.; Johnson, M. S.; Schinke, R. Ultraviolet Photodissociation of OCS: Product Energy and Angular Distributions. *J. Chem. Phys.* **2013**, *138* (9), 94314.

24. Schmidt, J. A.; Johnson, M. S.; Hattori, S.; Yoshida, N.; Nanbu, S.; Schinke, R. OCS Photolytic Isotope Effects from First Principles: Sulfur and Carbon Isotopes, Temperature Dependence and Implications for the Stratosphere. *Atmos. Chem. Phys.* **2013**, *13* (3), 1511–1520.

25. Schmidt, J. A.; Olsen, J. M. H. Photodissociation of OCS: Deviations between Theory and Experiment, and the Importance of Higher Order Correlation Effects. *J. Chem. Phys.* **2014**, *141* (18), 184310.

26. Lochte-Holtgreven, W.; Bawn, C. E. H. The Heat of Formation and Structure of the Carbon-Oxygen and Carbon-Sulphur Linkages. *Trans. Faraday Soc.* **1932**, *28* (0), 698–704.

27. Sivakumar, N.; Burak, I.; Cheung, W. Y.; Houston, P. L.; Hepburn, J. W. State-Resolved Photofragmentation of Carbonyl Sulfide (OCS) Monomers and Clusters. *J. Phys. Chem.* **1985**,

89 (17), 3609–3611.

28. Sivakumar, N.; Hall, G. E.; Houston, P. L.; Hepburn, J. W.; Burak, I. State-resolved Photodissociation of OCS Monomers and Clusters. *J. Chem. Phys.* **1988**, *88* (6), 3692–3708.

29. Nan, G.; Burak, I.; Houston, P. L. Photodissociation of OCS at 222 nm. The Triplet Channel. *Chem. Phys. Lett.* **1993**, *209* (4), 383–389.

30. Katayanagi, H.; Mo, Y.; Suzuki, T. 223 nm Photodissociation of OCS. Two Components in $S(^1D_2)$ and $S(^3P_2)$ Channels. *Chem. Phys. Lett.* **1995**, *247* (4–6), 571–576.

31. Sato, Y.; Matsumi, Y.; Kawasaki, M.; Tsukiyama, K.; Bersohn, R. Ion Imaging of the Photodissociation of OCS Near 217 and 230 nm. *J. Phys. Chem.* **1995**, *99* (44), 16307–16314.

32. Mo, Y.; Katayanagi, H.; Heaven, M. C.; Suzuki, T. Simultaneous Measurement of Recoil Velocity and Alignment of $S(^1D_2)$ Atoms in Photodissociation of OCS. *Phys. Rev. Lett.* **1996**, *77* (5), 830–833.

33. Sugita, A.; Mashino, M.; Kawasaki, M.; Matsumi, Y.; Bersohn, R.; Trott-Kriegeskorte, G.; Gericke, K.-H. Effect of Molecular Bending on the Photodissociation of OCS. *J. Chem. Phys.* **2000**, *112* (16), 7095–7101.

34. Katayanagi, H.; Suzuki, T. Non-Adiabatic Bending Dissociation of OCS: The Effect of Bending Excitation on the Transition Probability. *Chem. Phys. Lett.* **2002**, *360* (1–2), 104–110.

35. van den Brom, A. J.; Rakitzis, T. P.; Heyst, J. van; Kitsopoulos, T. N.; Jezowski, S. R.; Janssen, M. H. M. State-to-State Photodissociation of OCS (v_2=0,1|JlM). I. The Angular Recoil Distribution of CO ($X^1\Sigma^+$;v=0|J). *J. Chem. Phys.* **2002**, *117* (9), 4255–4263.

36. Kim, M. H.; Li, W.; Lee, S. K.; Suits, A. G. Probing of the Hot-Band Excitations in the Photodissociation of OCS at 288 nm by DC Slice Imaging. *Can. J. Chem.* **2004**, *82* (6), 880–884.

37. Lipciuc, M. L.; Janssen, M. H. M. Slice Imaging of Quantum State-to-State Photodissociation Dynamics of OCS. *Phys. Chem. Chem. Phys.* **2006**, *8* (25), 3007–3016.

38. Brouard, M.; Green, A. V.; Quadrini, F.; Vallance, C. Photodissociation Dynamics of OCS at 248 nm: The $S(^1D_2)$ Atomic Angular Momentum Polarization. *J. Chem. Phys.* **2007**, *127* (8), 84304.

39. Brouard, M.; Quadrini, F.; Vallance, C. The Photodissociation Dynamics of OCS at 248 nm: The $S(^3P_2)$ Atomic Angular Momentum Polarization. *J. Chem. Phys.* **2007**, *127* (8), 84305.

40. Lipciuc, M. L.; Rakitzis, T. P.; Meerts, W. L.; Groenenboom, G. C.; Janssen, M. H. M. Towards the Complete Experiment: Measurement of $S(^1D_2)$ Polarization in Correlation with Single Rotational States of CO(J) from the Photodissociation of Oriented OCS(v_2 = 1|JlM = 111). *Phys. Chem. Chem. Phys.* **2011**, *13* (18), 8549–8559.

41. Zhao, Z.; Stickel, R. E.; Wine, P. H. Quantum Yield for Carbon Monoxide Production in the 248 nm Photodissociation of Carbonyl Sulfide (OCS). *Geophys. Res. Lett.* **1995**, *22* (5), 615–618.

42. J. B. Burkholder, S. P. Sander, J. Abbatt, J. R. Barker, R. E. Huie, C. E. Kolb, M. J. Kurylo, V. L. Orkin, D. M. Wilmouth, and P. H. Wine "Chemical Kinetics and Photochemical Data for Use in Atmospheric Studies, Evaluation No. 18," JPL Publication 15-10, Jet Propulsion Laboratory, Pasadena, 2015 Http://jpldataeval.jpl.nasa.gov.

43. Breckenridge, W. H.; Taube, H. Some Reactions of Ground-State (^3P) and Electronically Excited (^1D) Sulfur Atoms. *J. Chem. Phys.* **1970**, *53* (5), 1750–1767.

44. van Veen, N.; Brewer, P.; Das, P.; Bersohn, R. The Adiabatic and Diabatic Reactions of $S(^1D)$ Atoms with OCS: Internal State Distribution of the S_2 Products. *J. Chem. Phys.* **1983**, *79* (9), 4295–4301.

45. Toulson, B. W.; Alaniz, J. P.; Hill, J. G.; Murray, C. Near-UV Photodissociation Dynamics of CH_2I_2. *Phys. Chem. Chem. Phys.* **2016**, *18* (16), 11091–11103.

46. PGOPHER, a Program for Simulating Rotational Structure, C. M. Western, University of Bristol, Http://pgopher.chm.bris.ac.uk; PGOPHER, a Program for Simulating Rotational Structure, C. M. Western, University of Bristol, http://pgopher.chm.bris.ac.uk.

47. van den Brom, A. J.; Rakitzis, T. P.; Janssen, M. H. M. Photodissociation of Laboratory Oriented Molecules: Revealing Molecular Frame Properties of Nonaxial Recoil. *J. Chem. Phys.* **2004**, *121*

(23), 11645–11652.

48. Hsu, C.-W.; Liao, C.-L.; Ma, Z.-X.; Tjossem, P. J. H.; Ng, C. Y. A Study of the $S(^3P_{2,1,0};^1D_2)$ Production in the 193 nm Photodissociation of $CH_3S(\check{X})$. *J. Chem. Phys.* **1992**, *97* (9), 6283–6290.

49. Rose, R. A.; Orr-Ewing, A. J.; Yang, C.-H.; Vidma, K.; Groenenboom, G. C.; Parker, D. H. Photodissociation Dynamics of the $A^2\Sigma^+$ State of SH and SD Radicals. *J. Chem. Phys.* **2009**, *130* (3), 034307–034314.

50. Hishikawa, A.; Ohde, K.; Itakura, R.; Liu, S.; Yamanouchi, K.; Yamashita, K. Femtosecond Transition-State Dynamics of Dissociating OCS on the Excited $^1\Sigma^+$ Potential Energy Surface. *J. Phys. Chem. A* **1997**, *101* (4), 694–704.

51. Fano, U. Effects of Configuration Interaction on Intensities and Phase Shifts. *Phys. Rev.* **1961**, *124* (6), 1866.

52. Morino, Y.; Nakagawa, T. Least-Squares Determination of the Anharmonic Potential Constants of Carbonyl Sulfide. *J. Mol. Spectrosc.* **1968**, *26* (4), 496–523.

Table 4-1. Summary of OCS electronically excited states. E is the vertical excitation energy. Adapted from Schmidt *et al. J. Chem. Phys.* **2012**, *137* (5), 54313.

Label	C_s	$C_{\infty v}$	E / eV	Type
X	$1^1A'$	$1^1\Sigma^+$	0	Bound
A	$2^1A'$	$1^1\Delta$	5.82	Dissociative
B	$1^1A''$	$1^1\Sigma^-$	5.73	Dissociative
C	$2^1A''$	$1^1\Delta$	5.88	Bound
a	$1^3A'$	$1^3\Sigma^+$	5.05	Dissociative
b	$1^3A''$	$1^3\Delta$	5.42	Dissociative
c	$2^3A''$	$1^3\Sigma^-$	5.76	Bound
d	$2^3A'$	$1^3\Delta$	5.45	Bound

Table 4-2. Band progressions identified in the $S(^3P_2)$ PHOFEX spectrum of OCS. The uncertainty (1σ) in the reported band centers is ±3 cm⁻¹ and the values in parentheses are the FWHM of the Lorentzian fits.

Progression	$\bar{\nu}$ / cm⁻¹	λ / nm	Intensity	Assignment
I	42719 (61)	234.09	0.24	$2^3A''$ ($1^3\Delta$)
	43389 (43)	230.47	0.70	$n\nu_1$
	44071 (56)	226.91	1.00	
	44745 (51)	223.49	0.90	
	45411 (46)	220.21	0.62	
II	42352 (77)	236.12	0.18	hot bands $2^1A'$($1^1\Delta$)
	43045 (51)	232.31	0.25	$n\nu_1$
	43755 (68)	228.55	0.25	
	44468 (52)	224.88	0.16	
III	42868 (123)	233.27	0.14	$2^1A'$ ($1^1\Delta$)
	43588 (105)	229.42	0.24	$n\nu_1$
	44292 (65)	225.78	0.45	
	44992 (101)	222.26	0.28	
	45701 (65)	218.81	0.21	
IV	44621 (50)	224.11	0.27	$2^3A''$ ($1^3\Delta$)
	45314 (50)	220.68	0.41	$n\nu_1+2\nu_2$
	46007 (55)	217.36	0.40	
	46679 (74)	214.23	0.30	

Table 4-3. Spectroscopic constants from anharmonic oscillator fit to the $2^3A''$ state

Parameter	Value / cm^{-1}
E_0	42719
ω_1	679 ± 6
ω_2	244 ± 6
x_{11}	−2.4 ± 1.2
x_{22}	0
x_{12}	11.6 ± 1.9

5   Competing Pathways in the Near-UV Photochemistry of Acetaldehyde

Toulson, B. W., Kapnas, K. M., Fishman, D.A. & Murray, C. *in preparation.*

5.1   **Introduction**

Studies of organic carbonyl photochemistry have an extensive history, dating back to work by Norrish.[1] Multiple products channels and mechanisms that depend on excitation wavelength have been identified, including the roaming mechanism,[2] shortly after it was first observed in formaldehyde.[3] Carbonyls and ketones are sufficiently abundant that photo-tautomerization to enols may produce considerable quantities of organic acids in the atmosphere.[4] The evolving view of acetaldehyde photochemistry suggests much more remains to be uncovered.

The first electronic absorption band of acetaldehyde arises from excitation of an electron from the oxygen lone pair to the lowest unoccupied CO π^* orbital. The absorption spectrum appears as a broad continuum spanning 240–336 nm with diffuse vibrational structure superimposed. Jet cooled emission spectra reveal the 0_0^0 origin band of the $S_1 \leftarrow S_0$ electronic transition to be at 335.9 nm.[5] The spectra show that the hydrogen-wagging and methyl-torsion modes are strongly active, consistent with a large geometric rearrangement towards the S_1 minimum, with the methyl group rotating from an eclipsed to staggered conformation, and the aldehyde functional group distorting to a pyramidal arrangement.[5–9] Laser induced phosphorescence excitation spectra put the 0_0^0 origin band of the $T_1 \leftarrow S_0$ at 367.1 nm.[10] Rovibrational state-dependent quantum beats in the fluorescence emission from acetaldehyde are observed for $\lambda > 319$ nm, and have been assigned to coherent excitation of S_1-T_1 states.[11]

Four sets of products, each accessible by multiple pathways are energetically allowed in the near-ultraviolet photochemistry of acetaldehyde

$$CH_3CHO + h\nu \quad \rightarrow CH_4 + CO \qquad\qquad \text{any } \lambda \qquad\qquad\qquad\qquad (I)$$

$$\rightarrow CH_3 + HCO \qquad\qquad \lambda < 345 \text{ nm} \qquad\qquad\qquad (IIa)$$

$$\rightarrow CH_3CO + H \qquad\qquad \lambda < 325 \text{ nm} \qquad\qquad\qquad (IIb)$$

$$\rightarrow CH_3 + CO + H \qquad\qquad \lambda < 294 \text{ nm} \qquad\qquad\qquad (III)$$
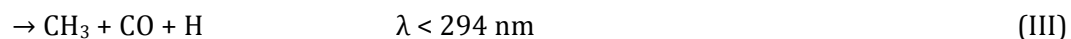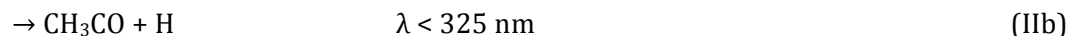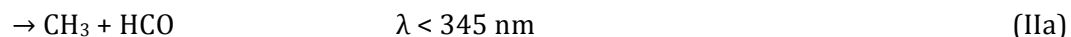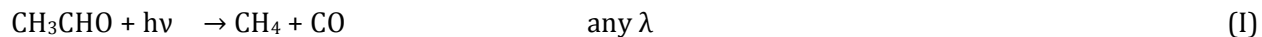
Threshold wavelengths for the thermochemical formation of fragments are calculated from values reported in the active thermochemical tables (ATcT) at 0K.[12] Figure 5-1 illustrates important stationary points on the S_0, S_1 and T_1 electronic surfaces of acetaldehyde.
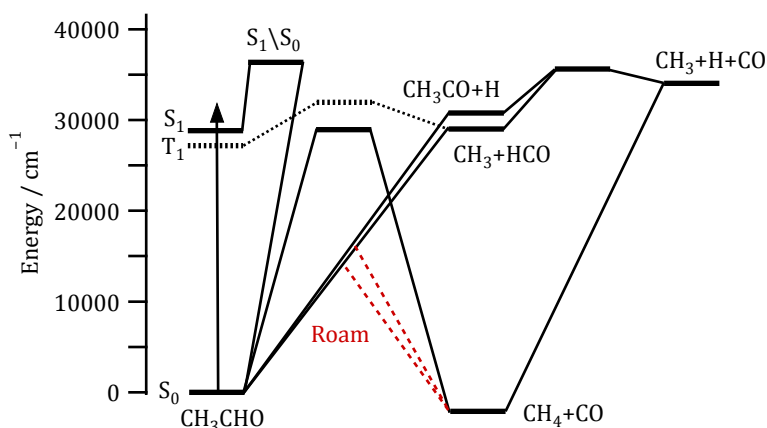
Figure 5-1. Schematic of important stationary points on the S_0, S_1 and T_1 electronic surfaces of acetaldehyde

Multiple pathways to molecular products have been identified by inspection of the CH_4+CO product state distribution, internal conversion (IC) to S_0 is followed by either: dissociation over a transition state (TS), or by roaming, which could occur as frustrated abstraction reaction of CH_3+HCO or

H+CH$_3$CO. Dissociation over a conventional tight TS leads to CO products with large rotational energy, while the repulsive potential after the barrier imparts significant translational energy in the products. Acetaldehyde was the second molecule confirmed to exhibit the roaming mechanism[2] after formaldehyde;[3] 15% of CO products following photolysis at 308 nm were formed with minimal vibrational, rotation and translational energy. Quasi-classical trajectory calculations on *ab initio* surfaces indicate that CH$_3$+HCO radicals access a broad plateau and roam prior to a unimolecular abstraction reaction leading to CH$_4$+CO.[13] 84±10% of molecular products were suggested to form *via* the CH$_3$ roaming mechanism,[14] this result was significant in that it showed roaming was not restricted to H atoms, and could be the dominant molecular pathway. New experiments suggest that two types of roaming occur: CH$_3$ and H atom roaming,[15] the latter being the source of CH$_4$+CO(low *J*) between 308 and 322 nm, first identified by Houston and Kable. CH$_3$ roaming was suggested to instead produce CO with modest translation and rotational excitation.

Two pathways to radical CH$_3$+HCO products have been identified, barrierless dissociation on S$_0$ or dissociation over a barrier on T$_1$, with the former only detected recently. Involvement of the T$_1$ surface in forming CH$_3$+HCO products was proposed and confirmed by Horowitz and coworkers.[16,17] The fluorescence emission of acetaldehyde declines precipitously for λ < 319 nm, coinciding with surmounting a barrier to forming CH$_3$+HCO on the T$_1$ surface.[9,11,18] CH$_3$ and HCO products from acetaldehyde have been detected using laser induced fluorescence (LIF),[19–22] and indicate substantial rotation excitation of the HCO fragment owing to the transition state geometry.[23] Ion imaging experiments probing CH$_3$ and HCO photoproducts show that essentially all available energy is partitioned into translational energy release in the vicinity above the T$_1$ barrier.[24] At shorter pump wavelengths the degree of internal excitation is observed to increase. Threshold wavelengths for dissociation on T$_1$ have been estimated as: 320.5 nm,[24] between 318.3–323.0 nm,[25] 318.5(5) nm[26] and 319.5(5) nm.[27] A change in the rotational population of HCO above

and below ~319 nm was noted by Heazlewood and coworkers.[25] A modest yield of HCO products was still observed at photolysis wavelengths as long as 331 nm, and could be modeling by a state distribution consistent with dissociation occurring on S_0, whereas previously it was thought only radiative relaxation was active. Subsequent ion imaging experiments at photolysis wavelengths between 318–321 nm have confirmed slow CH_3 fragments are formed.[26,27]

At shorter photolysis wavelengths slow CH_3 fragments are evident, however attributing the source is difficult as the three-body fragmentation pathway becomes energetically accessible. Shubert and Pratt have reported ion images of CH_3 and HCO products at a pump wavelength of 266 nm using VUV ionization at 119.46 nm (10.379 eV).[28] The similarity of the translational energy distributions for CH_3 and HCO suggests dissociation to CH_3+H+CO is minor, however definitive assignment of the slow fragments to S_0 photochemistry was precluded as the T_1 distribution is expected to be broad at shorter pump wavelengths. Ion imaging at pump wavelengths of 276 and 283 nm have shown the slow CH_3 component is more prominent in the umbrella mode excited $CH_3(v_2=1)$ than the ground $CH_3(v_2=0)$, which could suggest that different mechanisms are responsible for the fast and slow CH_3 fragments.[27]

Quasi-classical trajectory calculations on *ab initio* potential energy surfaces have been used extensively to provide insight into the photodissociation dynamics of acetaldehyde. Trajectories equivalent to photolysis at 230 nm suggest many different products channels are active: CH_3+HCO (45%), CH_4+CO (20%), CH_3+CO+H (15%) and CH_3CO+H (10%), while the remaining 10% were products that are yet to be observed experimentally.[29] Energy disposal of fragments and vector correlations in CH_4+CO products have been explored for conventional TS and roaming mechanisms.[13,30] Trajectories incorporating surface hopping between have explored the role of ISC from $S_1 \rightarrow T_1$ and $T_1 \rightarrow S_0$ in forming CH_3+HCO products.[31]

In this paper, we report ion imaging measurements of CH_3 fragments that reveal multiple pathways to the same set of products. By systematically exploring product formation over a timescale of picoseconds to nanoseconds, and wavelengths between 265-328 nm, an evolving picture of the dynamics is found. Evidence to suggest that the three-body CH_3+CO+H pathway remains closed at all wavelengths is presented.

5.2 Experimental methods

Experiments were performed in a velocity-map ion imaging mass spectrometer, previously described in detail.[32] Ion images were recorded using direct-current (DC) slice velocity map imaging.[33] Photofragment excitation (PHOFEX) spectra were recorded with the mass spectrometer operating in a conventional Wiley-McLaren time-of-flight arrangement.

Acetaldehyde (Sigma-Aldrich >99.5% purity) was cooled in an ice bath to minimize the amount of acetaldehyde vapor entrained when flowing Ar carrier gas over the sample. The mixture was expanded into high vacuum from a stagnation pressure of 1 atm using a solenoid pulsed valve (General Valve, Series 9). The expansion was skimmed (Beam Dynamics) to form a molecular beam before being intersected by counter-propagating photolysis and ionization laser beams. A stack of custom electrodes accelerates the resultant ions towards a MCP/phosphor assembly (Photonis) fitted with a fast high voltage gate module (Photek GM-MCP-2). The phosphorescence corresponding to fragments in the mass spectrum was monitored as a function of pump wavelength by a silicon photomultiplier (SenSL) to generate PHOFEX spectra. Ion images were acquired while gating the detector to obtain the central ~20 ns of the ion packet. Photolysis and probe laser pulse energies were monitored with a photodiode (Thorlabs DET10a) that had been calibrated against an

115

energy meter (Gentec Maestro). Signals were digitized by an oscilloscope (LeCroy HDO4054) and camera (Basler a312f) interfaced to a data acquisition PC running custom written software (National Instruments LabVIEW).

Pump laser pulses spanning the 260–328 nm wavelength range were generated using a mid-band Nd:YAG-pumped optical parametric oscillator (OPO) (Continuum Surelite EX and Horizon II). The OPO generated a broadly tunable UV beam with a linewidth of 5–7 cm^{-1}. The pulse energy varied from 1.1 to 2 mJ across the wavelength range. The pump was loosely focused into the ionization region of the mass spectrometer with an uncoated fused silica lens of focal length $f = 1000$ mm. Products were detected using single photon VUV ionization. VUV radiation at 118.2 nm (10.49 eV) was produced by 3rd harmonic generation of the frequency tripled output of a Nd:YAG laser (Continuum Surelite II–10, <20 mJ) in a static gas cell containing a Xe/Ar mixture (10:1) at a total pressure of ~80 Torr.[34] The gas cell was separated from the ionization chamber by a MgF$_2$ lens that focused the VUV into the molecular beam while re-collimating residual 355 nm light. Unless otherwise indicated, photolysis and probe beams were temporally separated by 40 ns. A digital delay generator (Quantum Composers, 9528) was used to control the time delay between the photolysis and ionization pulses.

Time-resolved measurements were made using a Nd:YAG laser (Eskpla PL2143) generating pulses of 28 ps duration at a repletion rate of 10 Hz. UV pulses at wavelengths of 266 nm and 355 nm were directed to the spectrometer, 0.5 mJ of the former is used to dissociate acetaldehyde while 2.1 mJ of the latter was used to generate picosecond VUV pulses in the same Xe/Ar gas cell. The time delay between the photolysis and ionization pulses was stepped over a 2 ns range using a computer-controlled delay line.

5.3 **Results**

The photolysis pulse is intended to dissociate CH_3CHO and the VUV probe pulse is intended to ionize nascent CH_3 (IE = 9.843 eV), HCO (IE = 8.12 eV) and CH_3CO (IE = 7–8 eV) radical products. CH_3 and HCO radicals have been detected using single photon ionization at similar VUV wavelengths following CH_3CHO dissociation at 266 nm.[28] The ionization cross-sections of both CH_3 and HCO are small at 118 nm, but likely insensitive to the rotational or vibrational state distribution of the product and we assume that ionization of both fragments is universal.[35] Within our signal to noise we did not see any significant signal that could be attributed to CH_3CO. The molecular products, CH_4 and CO, have ionization energies greater than the 10.49 eV probe photon energy (CH_4 has an IE = 12.61 eV, CO = 14.01 eV) and were not observed in the mass spectrum. The measurements are complicated slightly, however, by efficient ionization of the parent CH_3HCO (IE = 10.23 eV), causing a significant background problem when the time ordering of the pump and probe are reversed (but made alignment easy). A slow component appears in CH_3 ion images at all pump λ in the presence of clusters; the component was removed after optimizing pulse valve tension, timing, sample temperature and Ar carrier gas pressure. The absence of clusters was monitored on a daily basis by photolysis at 308 nm. The primary focus of this work is exploring CH_3 photolysis products.

5.3.1 **Nanosecond ion imaging**

DC sliced velocity-map ion images of CH_3 products were recorded following excitation of CH_3CHO at over the range 265–328 nm. Images were recorded at 1 nm intervals; Figure 5-2 shows ion images at a few selected wavelengths that excite to above the T_1 barrier. An ion image "movie" showing images acquired at all wavelengths photolysis wavelengths is available as supplementary material.

A small signal induced by the ionization laser alone was observed and has been subtracted from the images shown in Figure 5-2. No CH_3^+ signal resulted from the photolysis laser alone. In the ion images an isotropic ring is apparent for pump $\lambda < \sim318$ nm, corresponding to fast CH_3 fragments. This behavior is consistent with dissociation requiring sufficient energy to scale the barrier to CH_3+HCO on the T_1 surface, after the barrier the surface is repulsive leading to substantial kinetic energy in the products. A slow component, not due to clusters, appears in the ion images at $\lambda < \sim277$ nm, the relative contribution of which gradually increases towards shorter wavelengths.
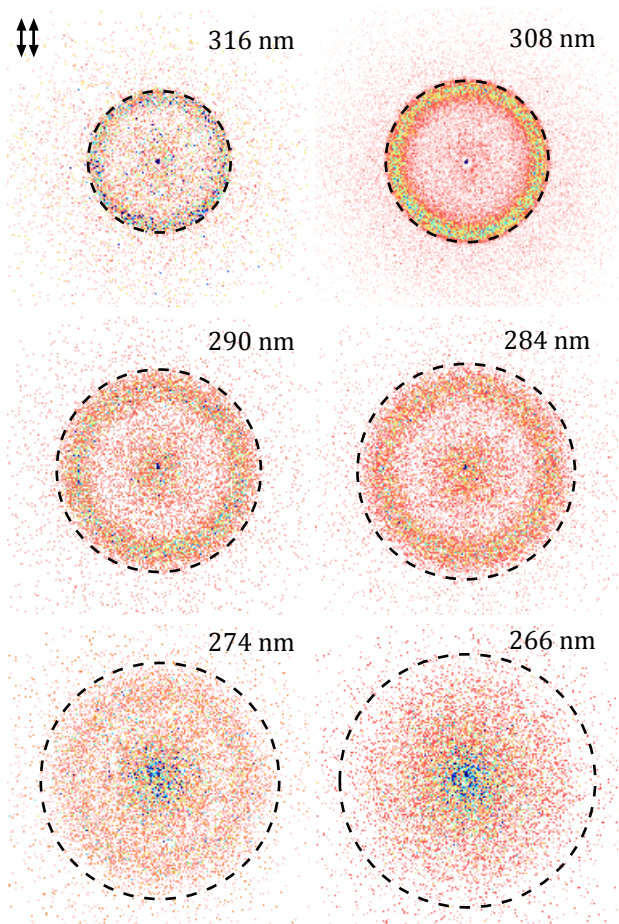
Figure 5-2. Ion images of CH_3 products from the photodissociation of CH_3CHO at 316, 308, 290, 284, 274 and 266 nm. Dashed lines mark the maximum recoil speed for fragments.

CH$_3$ fragment speed distributions were extracted from ion images at each pump wavelength and used to construct an image of the CH$_3$ speed distributions as a function of pump wavelength in Figure 5-3(a), where color scaling is used to represent the population. The speed distributions have been normalized at each discrete pump wavelength. Figure 5-3(a) shows a fast CH$_3$ component first appears as the T$_1$ barrier is exceeded at $\lambda \sim 318$ nm, with a narrow distribution of speeds peaking near to the maximum velocity (v_{max}) allowed by conservation of energy for a pump induced dissociation. The distribution the speed distribution changes gradually, broadening and shifting to values modestly smaller than the v_{max} at shorter pump wavelengths.
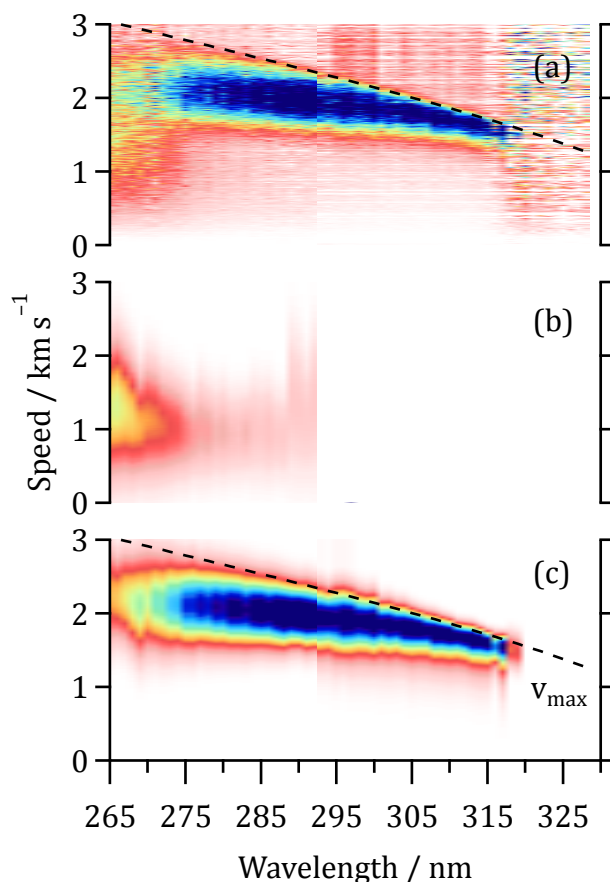
Figure 5-3. (a) Image constructed from CH$_3$ speed distributions from the photolysis of acetaldehyde between 265–328 nm. The color represents the population. The speed distribution was fit to the

sum of two Gaussian functions for (b) a fast component near ~2000 ms^{-1} and (c) a slow component near ~1200 ms^{-1}. The slow component is absent at longer pump wavelengths.

Speed distributions of CH_3 at selected pump wavelengths are shown Figure 5-4 to emphasize: at pump λ just in excess of the T_1 barrier a relatively asymmetric CH_3 speed distribution is observed, that becomes increasingly diffuse and symmetric as the pump λ is decreased. At pump λ <277 nm a slow component near 1200 ms^{-1} grows in both absolute ion count and relative contribution with respect to the fast component.
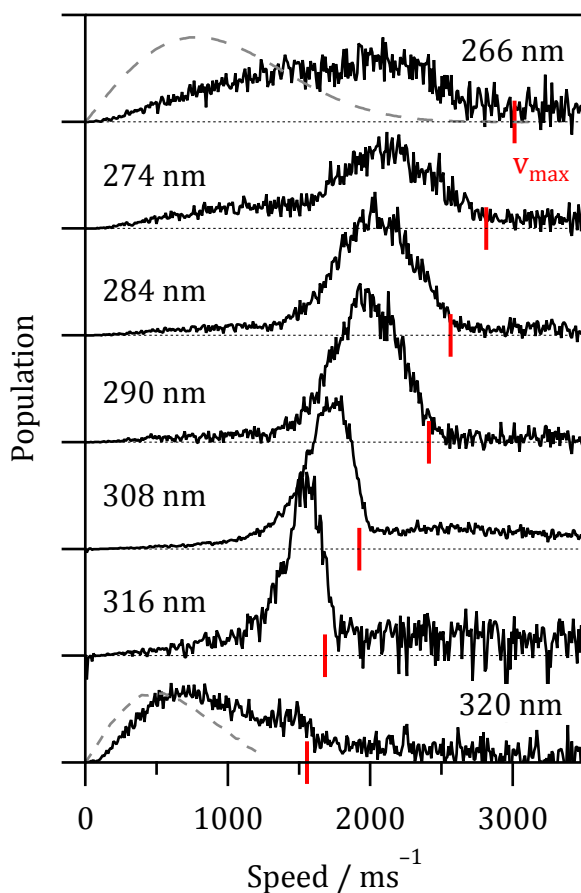
Figure 5-4. Speed distributions of CH_3 from the photolysis of acetaldehyde at selected wavelengths between 266–320 nm. Dashed lines show predictions for unimolecular dissociation from a Separate Statistical Ensembles calculation.

Pump wavelengths of 317 and 320 nm access just above and below the T_1 barrier, the CH_3 product distribution changes dramatically in this vicinity. Ion images of CH_3 products were recorded as a function of pump – probe delay, as the time Δt was stepped between 30–210 ns in 30 ns increments. CH_3 speed distributions at 317 nm are shown in Figure 5-5(a), the fast and isotropic T_1 component at $\sim$1500 ms^{-1} appears promptly; more rapidly than the $\sim$7 ns laser pulses. At longer time delay, more ions are observed in the images along the propagation direction of the pump and probe lasers, indicative that fragments 'fly-out' of the probe volume. Figure 5-5(b) shows a small residual of the fast component remains in speed distributions of CH_3 at 320 nm, placing the T_1 barrier at $\lambda > 320$ nm. The distribution following photolysis at 320 nm is dominated by two time-dependent components, a slow component centered at $\sim$650 ms^{-1} and an extra component at speeds $> v_{max}$. The population of each component was extracted and is shown in Figure 5-5(c), the former grows in with a time constant of 61(10) ns, and the later decays with a time constant of 70(10) ns. The absolute yield of CH_3 ions is reduced by at least a factor of 2 between photolysis at 317 and 320 nm, as radiative relaxation mechanisms are expected to compete with dissociation.
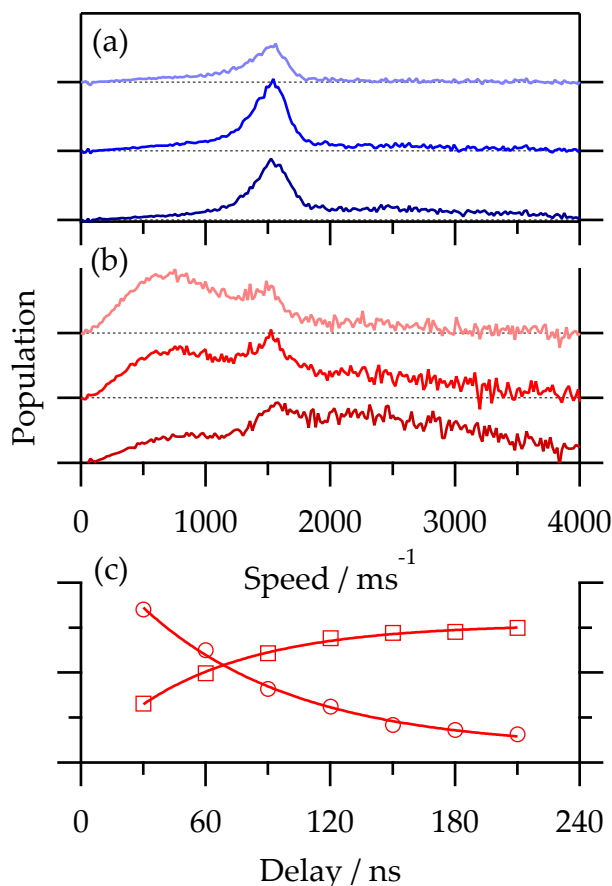
Figure 5-5. Speed distributions of CH_3 from the photolysis of acetaldehyde at (a) 317 nm and (b) 320 nm for pump – probe delays of 210, 90 and 30 ns (top to bottom). The time-dependent population (c) of the growing slow component at 650 ms^{-1} (squares) and decaying component at $\sim$2500 ms^{-1} (circles) seen in (b) have been extracted.

5.3.2 PHOFEX spectroscopy

PHOFEX action spectra of CH_3CHO were recorded by repeatedly scanning the photolysis wavelength between 260–328 nm while monitoring the total ion signals corresponding to CH_3 and HCO, which were the only fragments that depended on both the photolysis and probe lasers. The PHOFEX spectra are shown in Figure 5-6 alongside the conventional room temperature absorption spectrum. Only CH_3 and HCO signals induced by the probe laser were observed by applying two

narrow gates to the detector, ensuring the signal is free from pump-only contributions that occur ~40 ns earlier. A surprising observation is that for all pump wavelengths the yields of CH_3 and HCO are equal, strongly suggesting that each CH_3 fragment is formed in conjunction with a HCO fragment and that even when energetically accessible, dissociation pathways to CH_3+H+CO remain inactive. The action spectra coarsely reproduce the room temperature acetaldehyde absorption spectrum. The band shape of the jet cooled action spectra is slightly narrower than the acetaldehyde absorption spectrum, the intensity of the vibrational progression remains comparable despite the cooling of the sample by preparation in a molecular beam, and is observed to blue shift by ~0.5 nm. The structure in the long λ part of the PHOFEX spectrum reported here agrees with the PHOFEX spectrum reported by Cruse and Softley that probed exclusively ground state CH_3 and HCO fragments using resonance enhanced multiphoton ionization.[24] The structure has been attributed to Franck-Condon active vibrational modes of the $S_0 \rightarrow S_1$ excitation.[36]
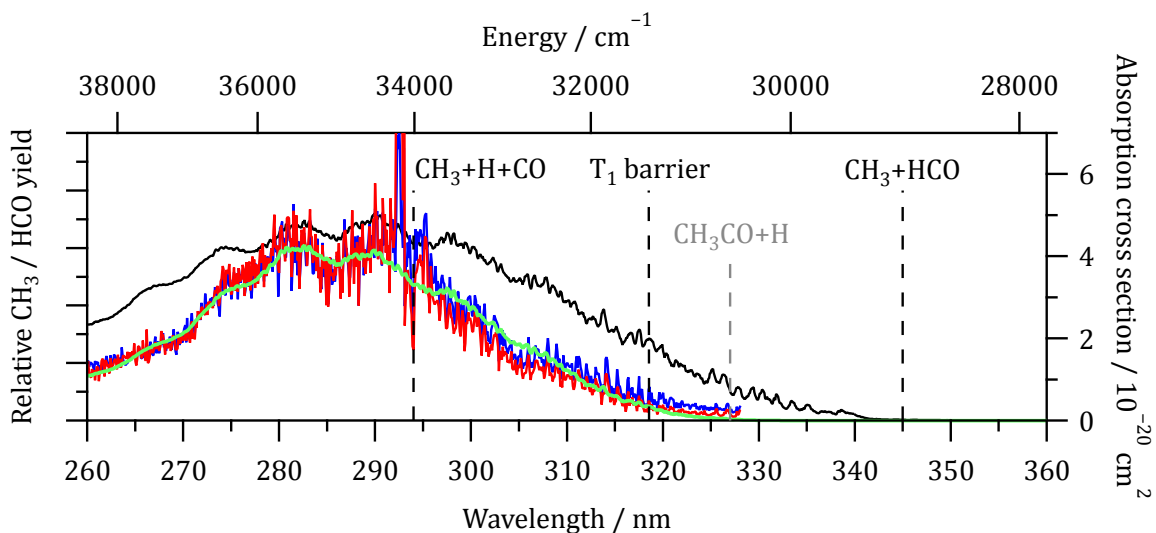
Figure 5-6. Acetaldehyde PHOFEX spectrum recorded probing CH_3 (blue) and HCO (red) products *via* VUV ionization at 118 nm. Conventional absorption spectra $\sigma(\lambda)$ measured by Schneider and Moortgat at 294 K (black), and the anticipated product yield $\sigma(\lambda)\Phi_{CH3+HCO}(\lambda)$ (green) is also shown.

5.3.3 Picosecond time-resolved ion imaging

Picosecond time-resolved DC sliced velocity-map ion images of CH_3 products have been recorded following excitation of CH_3CHO at a pump wavelength of 266 nm. The time delay Δt is defined as $t_{118} - t_{266}$ i.e. positive delays correspond to the 266 nm pump pulse preceding the 118.2 nm ionization pulse. The CH_3^+ at $\Delta t > 0$ arises from dissociation of the neutral. Ion images were recorded for $\Delta t > 0$ at a range of time delays spanning 1360 ps, the total ion count increased by ~35% between the shortest and longest time delay. The pump 266 nm alone did not produce any CH_3^+ ions, however a small contribution was observed that depended on the presence of probe 118.2 nm. Speed distributions extracted from the picosecond pump – probe ion images are shown in Figure 5-7. The nanosecond experiments guide our expectation; two components in the CH_3 speed distribution are indeed present. The speed distribution at the longest picosecond pump – probe delay is identical to the nanosecond result reported by Shubert and Pratt.[28] In addition, a weak time-independent tail at speeds exceeding energy conservation for the pump-induced photodissociation are observed (>3000 ms^{-1}).
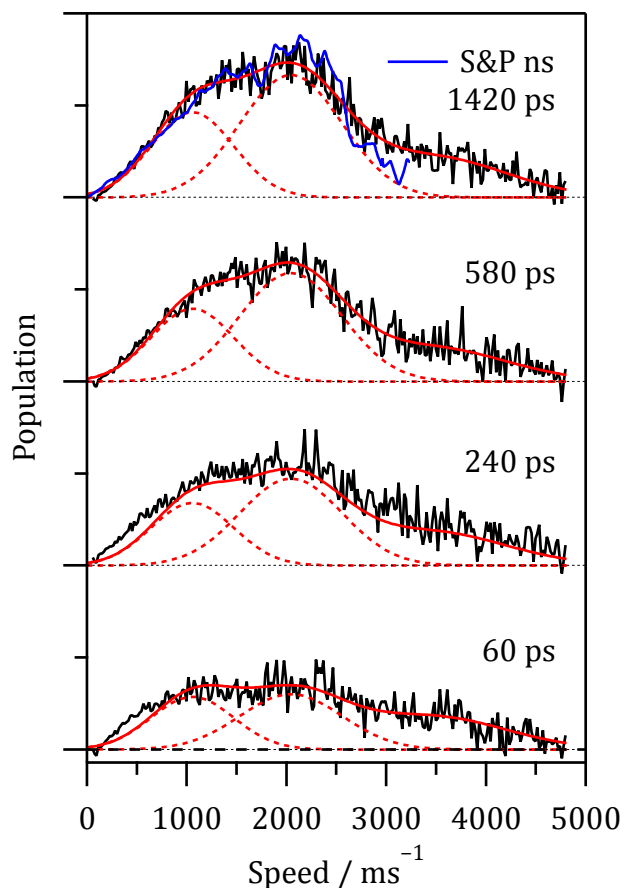
Figure 5-7. Speed distributions of CH_3 from the photolysis of acetaldehyde at 266 nm, obtained as a function of delay time between pump and probe picosecond pulses.

To extract the evolution with time of each CH_3 component, the speed distributions were fitted to the sum of three Gaussians. An initial fit at the longest time delay was used to constrain the position and width of each Gaussian, in the remaining fits the Gaussian heights were allowed to vary. The overall fit and the individual Gaussians are overlaid on the experimental speed distributions in Figure 5-7. The contribution of each CH_3 component from the Gaussian fit is shown in Figure 5-8 as a function of picosecond pump – probe delay. The kinetics of the slow component at ~1000 ms^{-1} and faster component at ~2000 ms^{-1} are different, an exponential fit to the former indicates a time constant of 560(90) ps, while the later is formed substantially faster with a time constant of 240(50) ps.
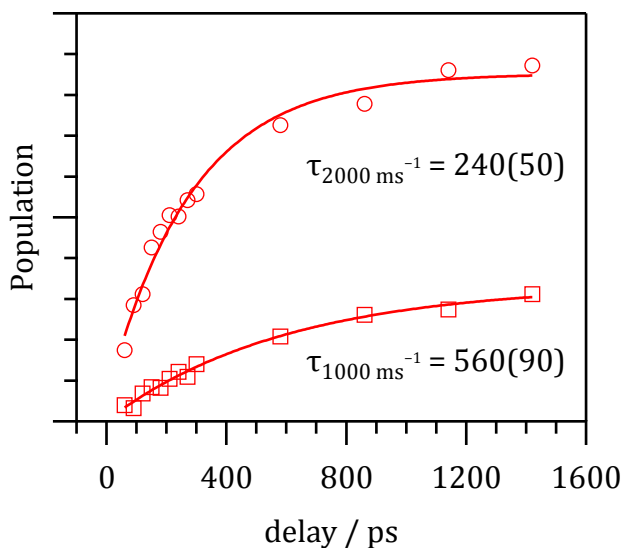
Figure 5-8. Time dependence of slow and fast components in CH_3 speed distribution obtained at a photolysis wavelength of 266 nm

5.4 Discussion

CH_3+HCO products from the photolysis of acetaldehyde in the near UV can form on both the T_1 and S_0 surfaces. Several potential routes have been presented in the literature, ISC from $S_1 \rightarrow T_1$ followed by prompt dissociation over a barrier on T_1 leads to products, while routes to S_0 include: IC from $S_1 \rightarrow S_0$ or by ISC from $S_1 \rightarrow T_1 \rightarrow S_0$. Spin-orbit coupling constants will determine the extent of the later route, and have been estimated to be 10 cm^{-1} and 65 cm^{-1}, respectively.[31] The large magnitude of the $T_1 \rightarrow S_0$ spin-orbit coupling indicates that products forming on S_0 might be expected at all wavelengths that the T_1 surface becomes populated. While dissociation over a barrier on T_1 leads to substantial translational energy release in the fragments, dissociation on S_0 is barrierless and therefore is expected to lead to a statistical distribution of energy amongst rotation, vibration and translation.

5.4.1 Long wavelength region: $\lambda > 317$ nm

The CH_3 speed distributions obtained at 317 nm just exceed the barrier to dissociation on T_1, fast CH_3 component moving with a speed of $\sim$1500 ms^{-1} near v_{max} dominates the speed distribution. CH_3 is formed on a timescale shorter than the nanosecond pump and probe duration, i.e. product formation is prompt. Lee and Chen have observed biexponential fluorescence decays of acetaldehyde at nearby pump wavelengths, one component corresponds to a rapid $\sim$15 ns process dominant at $\lambda < 317$ nm and a slower process that was reported to have a lifetime of 144 ns at 320.31 nm.[18] The slower process exponential decay from the fluorescence of CH_3CHO, and the fluorescence measured from HCO product formation have equal and opposite time constants between 312–319 nm, indicating that the dissociation rate is restricted by the rate of ISC.[18]

In contrast the CH_3 speed distribution at a pump wavelength of 320 nm is dominated by a slow component at $\sim$650 ms^{-1}, the shape of which is consistent with a statistical distribution of energy amongst fragments and reproduces prior reports.[26,27] The slow component appears on a timescale of 68(12) ns. Similar lifetimes have been calculated using variational transition state theory (TST), 100 ns for CD_3+HCO at 323 nm,[37] and 76 ns for CH_3+DCO of at 329 nm.[4] An extra component at speeds in excess of v_{max} is apparent at short pump – probe delays in Figure 5-5(a) and (b), the component delays with a time constant of 70(10) ns following photolysis at 317 and 320 nm. Transient absorption by electronically excited $CH_3CHO(S_1)$ could explain this feature as the fluorescence lifetime of CH_3CHO after excitation at 318.9 nm has been reported as 142 ns.[18] Quantum beats in the fluorescence provide evidence that population initially transferred to T_1 has insufficient energy to surmount the barrier to products, and may return to S_1 to subsequently fluoresce.[11] It has been suggested that internal conversion from $S_1 \rightarrow S_0$ followed by barrierless unimolecular dissociation leads to the $\sim$650 ms^{-1} CH_3 component,[26] however no argument against

ISC from T_1 to S_0 was presented. The agreement of the transient CH_3 decay and the rise of CH_3 products on S_0 suggest the dissociation rate is restricted by the rate of ISC and highlights competition between radiative and non-radiative relaxation mechanisms.

To model the product distribution for unimolecular dissociation quantitatively Phase Space Theory (PST) and Separate Statistical Ensembles (SSE) calculations have been performed at energies equivalent to above and below the T_1 barrier at 317 nm ($E_{AVL} = 2600$ cm^{-1}) and 320 nm ($E_{AVL} = 2300$ cm^{-1}). Rotational and vibrational constants for CH_3 and HCO were taken from de Wit and coworkers.[38] CH_3 was approximated as an oblate symmetric top, and HCO as a prolate symmetric top. Acetaldehyde has 15 vibrational modes, while CH_3 and HCO have 6 and 3 vibrational modes, leading to 6 disappearing vibrational modes that weight the vibrational state distribution. Reproducing work of Wittig and coworkers validated the code.[39] PST and SSE both predict similar distributions, with modest translational energy release. SSE restricts the density of states that contribute the fragment vibrational distribution to the vibrational modes that disappear upon breaking the bond, so necessarily predicts larger vibrational (and so smaller rotational and translational) excitation in the products than PST. The translational energy distributions predicted by SSE have been converted to speed to avoid making the assumption that the experimental CH_3 speed distribution corresponds to CH_3+HCO. Figure 5-4 shows SSE reasonably reproduces the slow component of the CH_3 speed distribution following photolysis at 320 nm.

5.4.2 Intermediate wavelength region: 277 < λ < 317 nm

The fast component of the CH_3 speed distribution arising from dissociation on T_1 is asymmetric following excitation near the T_1 barrier, however as the excess energy is increased the fast component becomes symmetric, pump wavelengths of 290 and 284 nm illustrate this in Figure 5-4.

Classical trajectories leading to CH_3+HCO on the T_1 surface by Thompson and co-workers sought to rationalize experimental observations of the CH_3 and HCO distribution shapes changing with wavelength.[40] Their calculations show that of an impulsive model captures the dynamics near the T_1 threshold dissociation at ~318 nm as the late transition state leads to the majority of energy available being released as translation, with only a narrow range of vibrational and rotational states populated. As the photolysis energy is increased the product distributions shift to larger translational energy and broaden. Energy below the barrier is partitioned impulsively, while energy above the barrier is apportioned statistically, with a more equitable distribution of energy into rotation, vibration and translation, i.e. the fraction of energy partitioned into translation decreases, though the absolute translational energy does indeed increase as the pump wavelength is decreased. At the shortest pump wavelength the rotational and vibrational distributions for CH_3 and HCO are described as symmetrical and Gaussian, while at λ ~318 nm the distributions are characterized as asymmetrical, consistent with the results reported here.

Fu and coworkers have calculated quasi-classical trajectories on *ab initio* surfaces; the trajectories were initialized on S_1 with spin-orbit coupling between S_1/T_1 of 5–10 cm^{-1} and T_1/S_0 of 65–70 cm^{-1}. Dissociation to CH_3+HCO occurred after surface hopping to T_1 and also after undergoing a second hop to S_0, producing fast and slow CH_3 respectively. In contrast with experimental results, CH_3+HCO products on S_0 are not observed below the T_1 barrier in the trajectory calculations. The fraction of CH_3+HCO products that form on S_0 over T_1 increases at shorter wavelengths. Branching between S_0:T_1 at 286 nm in the trajectory calculations was 0.3 using the authors preferred implementation of a soft constraint to satisfy zero-point energy (ZPE) requirements, while experiments suggest the onset for S_0 product (re)occurs at λ = 277 nm. Total translational energy distributions for CH_3+HCO from the photolysis of acetaldehyde at 286 nm obtained by probing CH_3 with VUV ionization are compared to distributions for CH_3+HCO formation on S_0 and T_1 surfaces

from trajectory calculations at an equivalent energy in Figure 5-9. The trajectory calculations underestimate the translational energy release associated with the T_1 surface.
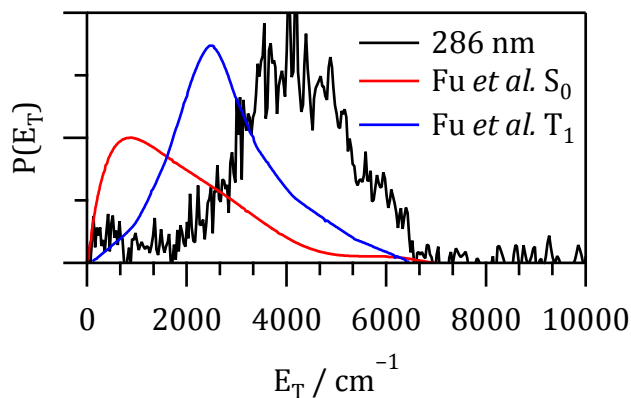
Figure 5-9. Translational energy distributions for CH_3+HCO from the photolysis of acetaldehyde at 286 nm probing CH_3 with VUV ionization are compared to trajectory calculations for products forming on S_0 and T_1 *ab initio* surfaces by Fu *et al.*

5.4.3   Short wavelength region: $\lambda < 277$ nm

A slow component becomes evident in the CH_3 speed distribution at $\lambda < 277$ nm, as the fast component becomes increasingly diffuse. The presence of two mechanisms forming CH_3 at shorter wavelengths is readily discerned from the evolution of the speed distributions with wavelength, and the presence of a small 'dip' between the fast and slow components resolved in the ion images reported here at 266 nm. The slow and fast CH_3 components have been extracted using a fit of two Gaussian functions at each pump wavelength, the resulting distributions are shown in Figure 5-3(b) and Figure 5-3(c). The branching between slow and fast CH_3 components from the fit is shown in Figure 5-11, the slow component increases in importance at shorter pump wavelengths to contribute ~0.5 at 266 nm.

Three-body dissociation is an alternative source of slow CH$_3$, thermodynamically accessible for pump $\lambda < 294$ nm. The dissociation could occur in either a concerted or stepwise manner. Stepwise decomposition of products from the molecular and radical pathways (I, IIa, IIb): *CH$_4$*+CO, CH$_3$+*HCO* or *CH$_3$CO*+H to form CH$_3$+H+CO will depend on the internal excitation of the fragments. Stepwise decomposition in acetone has been observed, and suggested to occur in formaldehyde.[41,42]

Highly internally excited CH$_4$* and cold CO have been identified as roaming photoproducts in acetaldehyde. The decomposition of CH$_4$ on S$_0$ is barrierless,[43,44] so a statistical energy disposal amongst fragments would be anticipated. However the experimental data indicate a rapid increase in slow CH$_3$ for $\lambda < 277$ nm whereas the onset for barrierless decomposition of CH$_4$* would be anticipated near the thermochemical threshold at $\lambda = 294$ nm. Other experiments provide information about the barriers to decomposition of CH$_3$CO and HCO. North and coworkers studied the photodissociation of acetone, observing that 30% of CH$_3$CO radicals underwent spontaneous decomposition and determined the barrier to be 6200(1100) cm^{-1}.[42] Tang and coworkers used acetyl chloride as a source of CH$_3$CO, estimating a smaller value for the barrier of 4900(170) cm^{-1}.[45] Combining the latter value for the CH$_3$CO barrier with the 0K thermochemical value for forming CH$_3$CO+H of 30750 cm^{-1}, suggests that a barrier for secondary decomposition *via* CH$_3$CO to produce CH$_3$+CO+H of 35700 cm^{-1}, or $\lambda < 280$ nm. Reported values for the barrier to combination of H + CO $\rightarrow$ HCO depend sensitively on experimental conditions, with values spanning 250–670 cm^{-1}. Peters and coworkers have argued the experimental value to be error, their high-level *ab initio* calculations suggest a substantially higher value of 1600(100) cm^{-1}.[46] Combining their barrier with the 0K thermochemical value for HCO $\rightarrow$ H + CO of 5100 cm^{-1}, results in a barrier of 6700(100) cm^{-1}. Addition of the 0K thermochemical value for formation of CH$_3$+HCO suggests the barrier for secondary decomposition *via* HCO to produce CH$_3$+CO+H of 35600 cm^{-1}, or $\lambda < 281$ nm. The

uncertainty in the barrier height for secondary decomposition of CH₃CO and HCO critically influences the anticipated threshold wavelength for stepwise three-body dissociation. The barriers for the two pathways for stepwise three-body decomposition suggested above are nearly identical; yet have not been reported as such in any other recent work. To compare the barriers on an equal footing potential energy cuts for H-CO and CH₃-CO bond extension are shown in Figure 5-10 at the RMP2/aVDZ level of theory. All calculations were performed using the MOLPRO 2012.1 quantum chemistry package.[47] The minimum energy path was found by optimizing the geometry for a fixed H/CH₃-CO separation, the energies are relative to the HCO / CH₃CO minimum. The calculations indicate that the barrier height for either decomposition route should be approximately equal.
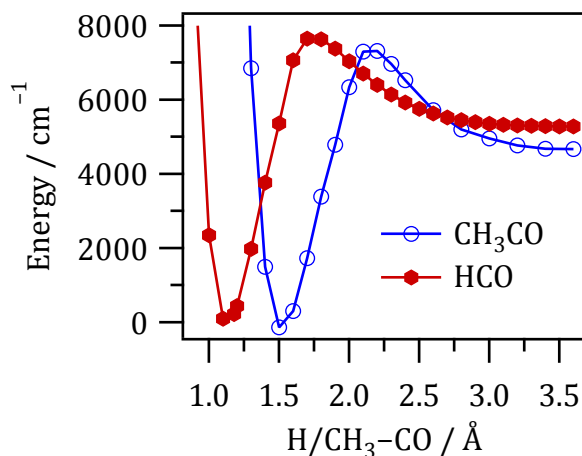
Figure 5-10. Relaxed potential energy cuts for H-CO and CH₃-CO bond extension

Roaming and three-body photodissociation mechanisms in acetaldehyde are both expected to lead to distributions with similar dynamical signatures: minimal translational and rotational excitation in the CO product, making it difficult to distinguish the photochemical mechanism.[38] Phase space theory (PST) was used to predict distributions from a two-step dissociation of CH₃CHO → CH₃+HCO → CH₃+H+CO. The ~6700 cm⁻¹ barrier to secondary decomposition of HCO was neglected. PST assumes the reaction coordinate along the potential energy surface will not influence the rate of

combination i.e. no barrier exists, so the validity of PST to model the second step is questionable. The PST calculations suggest the bulk of the H atom distribution detected following photolysis at 248 nm is more like that expected for CH_3CO+H rather than CH_3+H+CO, however this finding is at odds with experimental results from both cw-CRDS and FTIR emission spectroscopy at the same wavelength that found the CH_3CO+H channel to be inoperative, and suggests the PST calculations are in error. The alternative pathway *via* CH_3CO was not the focus of their study, however Mordaunt and coworkers have discussed the role of a barrier in the dissociation of CH_3CO; a statistical adiabatic impulsive (SAI) model was developed that describes the product translational energy distribution.[48]

We discount the CH_3+H+CO channel for the following reasons: Shubert and Pratt have shown the translational energy distributions of both CH_3 and HCO products are similar at 266 nm, suggesting the fragments share a dissociation origin. Second, the barrier to decomposition of either CH_3CO or HCO should lead to a kick in the translational energy distribution of CH_3 for the former,[48] and H for the latter, which is absent in the experimental data. Third, we add the observation that the PHOFEX action spectra of CH_3 and HCO are identical; *all* of the three-body dissociation routes would enhance the CH_3 yield relative to HCO. Decomposition of CH_4 or CH_3CO produces more CH_3, while the HCO yield would decrease if it decomposes to H+CO.

The contribution of the slow CH_3 channel to the overall CH_3 distribution is shown in Figure 5-11 and grows steadily at $\lambda < 277$ nm, accounting for approximately half of CH_3 products at 266 nm. Having shown that SSE provides a reasonable description for dissociation on S_0 at longer wavelengths, a SSE calculation was performed at an energy at $E_{AVL} = 8645$ cm^{-1}, corresponding to an experimental pump wavelength of 266 nm. The poor agreement between experiment and SSE is illustrated in Figure 5-4, as the statistical expectation continues to predict slow CH_3 fragments.
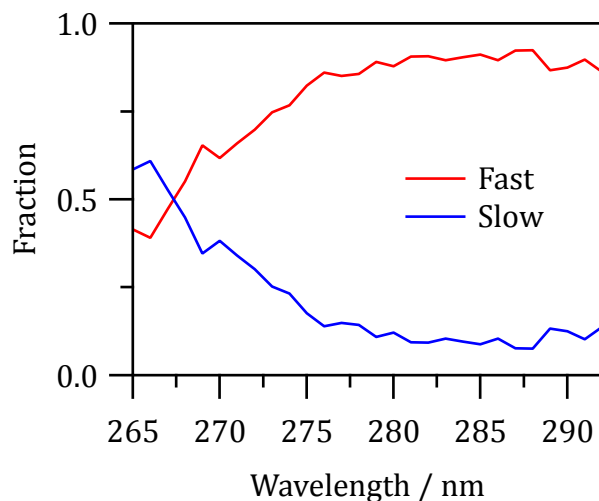
Figure 5-11. Branching between slow and fast CH_3 components from the photolysis of acetaldehyde at a function of pump wavelength

Picosecond pump – probe ion imaging has been used to follow the formation of CH_3, a fit to the speed distribution indicates two CH_3 components have different kinetics, as shown in Figure 5-8. A slow component described by a Gaussian at ~1000 ms^{-1} and faster component at ~2000 ms^{-1} form with time constants of 560(90) ps and 240(50) ps. The later corresponds to products formed on T_1, and places an upper limit on the time for ISC of 240(50) ps following photolysis at 266 nm. ISC from $S_1 \rightarrow T_1$ does not restrict the rate of formation for slow CH_3 at this pump wavelength, while the magnitude of the spin-orbit coupling from $T_1 \rightarrow S_0$ suggests this step should be not be limiting. Barrierless dissociation on S_0 may explore significant regions of the potential, delaying the formation of products.

An alternative mechanistic origin for the slow CH_3 component observed at $\lambda < 277$ nm, is a conical intersection (CI) between the S_1 and S_0 surfaces, potentially funneling population on to S_0, from where CH_3+HCO products could form. Chen and Wang first located such a CI along the CH_3–HCO extension coordinate, however trajectories including coupling between S_1/S_0 are yet to be reported.

134

A barrier on S_1 must be surmounted to access this region of the potential, consistent with the observation of a threshold for slow CH_3 products. To date a considerable range of barrier heights, spanning 5100–7940 cm^{-1} relative to the S_1 minimum have been reported.[31,49,50] As the CI occurs at extended C-C distance and above the CH_3+CHO asymptote, a bifurcation of trajectories may occur, allowing some fraction to follow a repulsive path to products more rapidly than a statistical redistribution of energy can occur, while other fragments may explore a greater extent of the S_0 potential and be produced statistically.

5.4.4 Photolysis quantum yields

Comparing the band shape of the PHOFEX spectrum of acetaldehyde obtained when detecting CH_3 and HCO products to the acetaldehyde room temperature absorption spectrum $\sigma(\lambda)$,[51] the PHOFEX yield is reduced the red and blue edges of the parent absorption band. The wavelength dependence of the product yield should be the product of $\sigma(\lambda)\ \Phi_{CH_3+HCO}(\lambda)$, where $\Phi_{CH_3+HCO}(\lambda)$ is the quantum yield for dissociation to CH_3+HCO as a function of wavelength taken from Moortgat and coworkers,[52] the result is overlaid in Figure 5-6. The action spectra and indirect determinations of product yields agree well across the entire 260–328 nm photolysis range studied. The quality of the agreement is surprising given that reports of CO products from acetaldehyde in collision free environments span ~230–325 nm,[15,50] in contradiction with collisional determinations that suggest $\Phi(CH_4+CO) = 0$ for $\lambda > 290$ nm. Prior studies have argued the product yield at the red edge of the absorption band is reduced, as the quantum yield for dissociation is less than unity, while absorption at the blue edge shows a decline in CH_3+HCO due to the increasing importance of the CH_4+CO product channel.[16,17,53] This study does not detect the fluorescence that should be associated with the former, or the products associated with the later, the results are however consistent with this explanation.

135

5.5   **Conclusions**

Ion imaging experiments show that different dynamics lead to CH_3 products in the photodissociation acetaldehyde, and have been categorized into three photolysis wavelength ranges: at $\lambda > 317$ nm corresponding to dissociation near/below the T_1 barrier slow CH_3 products are formed on S_0 that appear on a timescale of 61(10) ns, consistent with barrierless dissociation on S_0 and supported by statistical model predictions. Between $277 < \lambda < 317$ nm products from S_0 are not observed, dissociation instead occurs promptly on T_1, leading to significant translational recoil. The model of Thompson and coworkers qualitatively describes the partitioning of energy with pump wavelength. A third type of CH_3 is observed for $\lambda < 277$ nm, with two distinct signatures. First, a sharp increase in the fraction of slow over fast T_1 CH_3 fragments is observed, suggesting a barrier must be overcome. Second, CH_3+HCO distributions calculated with statistical models predict distributions with significantly less translation, and cannot reproduce the overall shape of the slow CH_3 component distribution. PHOFEX spectra of acetaldehyde probing CH_3 and HCO products between 260–328 nm are identical, suggesting CH_3+HCO rather than CH_3+CO+H products form at all wavelengths. Picosecond time-resolved ion imaging at 266 nm distinguishes the components in the CH_3 speed distribution, indicating the fast T_1 and slow components appear on different time scales. The T_1 component appears with a time constant of 240(50) ps while the latter has a time constant of 560(90) ps, confirming a different mechanistic origin and places an upper limit for ISC of ~240 ps following photolysis at 266 nm.

5.6   **Acknowledgements**

5.7 References

1.   Akeroyd, E. I. & Norrish, R. G. W. The photolysis of formaldehyde, acetaldehyde, and acetone at high temperatures. *J. Chem. Soc.* 890–894 (1936). doi:10.1039/JR9360000890

2.   Houston, P. L. & Kable, S. H. Photodissociation of acetaldehyde as a second example of the roaming mechanism. *PNAS* **103,** 16079–16082 (2006).

3.   Townsend, D. *et al.* The Roaming Atom: Straying from the Reaction Path in Formaldehyde Decomposition. *Science* **306,** 1158–1161 (2004).

4.   Andrews, D. U. *et al.* Photo-Tautomerization of Acetaldehyde to Vinyl Alcohol: A Potential Route to Tropospheric Acids. *Science* **337,** 1203–1206 (2012).

5.   Liu, H., Lim, E. C., Judge, R. H. & Moule, D. C. The hybrid rotational components in the 000 origin band of the ÃA'(S1)←X̃A'(S0) transition in acetaldehyde. *The Journal of Chemical Physics* **102,** 4315–4320 (1995).

6.   Noble, M., Apel, E. C. & Lee, E. K. C. The singlet π* ← n spectrum of jet-cooled acetaldehyde. *The Journal of Chemical Physics* **78,** 2219–2226 (1983).

7.   Noble, M. & Lee, E. K. C. Mode specificity and energy dependence of the dynamics of single rovibrational levels of S1 acetaldehyde in a supersonic jet. *The Journal of Chemical Physics* **80,** 134–139 (1984).

8.   Noble, M. & Lee, E. K. C. The jet-cooled electronic spectrum of acetaldehyde and deuterated derivatives at rotational resolution. *The Journal of Chemical Physics* **81,** 1632–1642 (1984).

9.   Ohta, N. & Baba, H. Emission properties to acetaldehyde vapor in relation to photodissociation. *J. Phys. Chem.* **90,** 2654–2661 (1986).

10.   Liu, H. *et al.* The T1(nπ*)←S0 laser induced phosphorescence excitation spectrum of acetaldehyde in a supersonic free jet: Torsion and wagging potentials in the lowest triplet state. *The Journal of Chemical Physics* **105,** 2547–2552 (1996).

11.   Gejo, T., Bitto, H. & Huber, J. R. Quantum beats in the S1 dynamics of acetaldehyde. *Chemical Physics Letters* **261,** 443–449 (1996).

12.   Ruscic, B. Active Thermochemical Tables (ATcT) values based on ver. 1.118 of the Thermochemical Network; available at ATcT.anl.gov. (2015).

13.   Shepler, B. C., Braams, B. J. & Bowman, J. M. Quasiclassical Trajectory Calculations of Acetaldehyde Dissociation on a Global Potential Energy Surface Indicate Significant Non-transition State Dynamics. *J. Phys. Chem. A* **111,** 8282–8285 (2007).

14.   Heazlewood, B. R. *et al.* Roaming is the dominant mechanism for molecular products in acetaldehyde photodissociation. *PNAS* **105,** 12719–12724 (2008).

15.   Lee, K. L. K. *et al.* Two roaming pathways in the photolysis of CH3CHO between 328 and 308 nm. *Chem. Sci.* **5,** 4633–4638 (2014).

16.   Horowitz, A. & Calvert, J. G. Wavelength dependence of the primary processes in acetaldehyde photolysis. *J. Phys. Chem.* **86,** 3105–3114 (1982).

17.   Horowitz, A., Kershner, C. J. & Calvert, J. G. Primary processes in the photolysis of acetaldehyde at 3000 .ANG. and 25.degree.C. *The Journal of Physical Chemistry* **86,** 3094–3105 (1982).

18.   Lee, S.-H. & Chen, I.-C. Non-exponential decays of the S1 vibronic levels of acetaldehyde. *Chemical Physics* **220,** 175–189 (1997).

19.   Kono, T., Takayanagi, M., Nishiya, T. & Hanazaki, I. Photodissociation of acetaldehyde studied by photofragment excitation spectroscopy in a supersonic free jet. *Chemical Physics Letters* **201,** 166–170 (1993).

20.   Kono, T., Takayanagi, M. & Hanazaki, I. Rotational excitation of formyl radical produced by

photodissociation of acetaldehyde in a supersonic jet. *J. Phys. Chem.* **97,** 12793–12797 (1993).

21. Lee, S.-H. & Chen, I.-C. Photofragments CH3($\tilde{X}2A2''$)+HCO($\tilde{X}2A'$) from acetaldehyde: Distributions of rotational states and preferential population of K doublets of HCO. *The Journal of Chemical Physics* **105,** 4597–4604 (1996).

22. Terentis, A. C., Stone, M. & Kable, S. H. Dynamics of Acetaldehyde Dissociation at 308 nm: Rotational (N, Ka) and Translational Distributions of the HCO Photoproduct. *J. Phys. Chem.* **98,** 10802–10808 (1994).

23. Yadav, J. S. & Goddard, J. D. Acetaldehyde photochemistry: The radical and molecular dissociations. *The Journal of Chemical Physics* **84,** 2682–2690 (1986).

24. Cruse, H. A. & Softley, T. P. Velocity-map imaging study of the photodissociation of acetaldehyde. *The Journal of Chemical Physics* **122,** 124303 (2005).

25. Heazlewood, B. R., Rowling, S. J., Maccarone, A. T., Jordan, M. J. T. & Kable, S. H. Photochemical formation of HCO and CH3 on the ground S0(A1′) state of CH3CHO. *The Journal of Chemical Physics* **130,** 054310 (2009).

26. Amaral, G. A., Arregui, A., Rubio-Lago, L., Rodríguez, J. D. & Bañares, L. Imaging the radical channel in acetaldehyde photodissociation: Competing mechanisms at energies close to the triplet exit barrier. *The Journal of Chemical Physics* **133,** 064303 (2010).

27. Zhang, Z. *et al.* Ion-Velocity Map Imaging Study of Photodissociation Dynamics of Acetaldehyde. *Chinese Journal of Chemical Physics* **27,** 249–255 (2014).

28. Shubert, V. A. & Pratt, S. T. Photodissociation of Acetaldehyde and the Absolute Photoionization Cross Section of HCO. *J. Phys. Chem. A* **114,** 11238–11243 (2010).

29. Han, Y.-C., Shepler, B. C. & Bowman, J. M. Quasiclassical Trajectory Calculations of the Dissociation Dynamics of CH3CHO at High Energy Yield Many Products. *J. Phys. Chem. Lett.* **2,** 1715–1719 (2011).

30. Shepler, B. C., Braams, B. J. & Bowman, J. M. 'Roaming' Dynamics in CH3CHO Photodissociation Revealed on a Global Potential Energy Surface. *J. Phys. Chem. A* **112,** 9344–9351 (2008).

31. Fu, B., Han, Y. & Bowman, J. M. Three-state surface hopping calculations of acetaldehyde photodissociation to CH3 + HCO on ab initio potential surfaces. *Faraday Discuss.* **157,** 27–39 (2012).

32. Toulson, B. W., Alaniz, J. P., Hill, J. G. & Murray, C. Near-UV photodissociation dynamics of CH_2I_2. *Phys. Chem. Chem. Phys.* **18,** 11091–11103 (2016).

33. Townsend, D., Minitti, M. P. & Suits, A. G. Direct current slice imaging. *Review of Scientific Instruments* **74,** 2530–2539 (2003).

34. Kung, A. H., Young, J. F. & Harris, S. E. Generation of 1182-Å radiation in phase-matched mixtures of inert gases. *Applied Physics Letters* **22,** 301–302 (1973).

35. Aguirre, F. & Pratt, S. T. Photoionization of vibrationally hot CH3 and CF3. *The Journal of Chemical Physics* **122,** 234303 (2005).

36. Baba, M., Hanazaki, I. & Nagashima, U. The S1(n, π*) states of acetaldehyde and acetone in supersonic nozzle beam: Methyl internal rotation and C=O out-of-plane wagging. *The Journal of Chemical Physics* **82,** 3938–3947 (1985).

37. Heazlewood, B. R. *et al.* Near-threshold H/D exchange in CD3CHO photodissociation. *Nat Chem* **3,** 443–448 (2011).

38. de Wit, G. *et al.* Product state and speed distributions in photochemical triple fragmentations. *Faraday Discuss.* **157,** 227–241 (2012).

39. Wittig, C. *et al.* Nascent product excitations in unimolecular reactions: The separate statistical ensembles method. *The Journal of Chemical Physics* **83,** 5581–5588 (1985).

40. Thompson, K. C., Crittenden, D. L., Kable, S. H. & Jordan, M. J. T. A classical trajectory study of the photodissociation of T1 acetaldehyde: The transition from impulsive to statistical

dynamics. *The Journal of Chemical Physics* **124,** 044302 (2006).

41.   Hobday, N. *et al.* Experimental and Theoretical Investigation of Triple Fragmentation in the Photodissociation Dynamics of H2CO. *J. Phys. Chem. A* **117,** 12091–12103 (2013).

42.   North, S. W., Blank, D. A., Gezelter, J. D., Longfellow, C. A. & Lee, Y. T. Evidence for stepwise dissociation dynamics in acetone at 248 and 193 nm. *The Journal of Chemical Physics* **102,** 4447–4460 (1995).

43.   Dutta, A. & Sherrill, C. D. Full configuration interaction potential energy curves for breaking bonds to hydrogen: An assessment of single-reference correlation methods. *The Journal of Chemical Physics* **118,** 1610–1619 (2003).

44.   Harding, L. B., Klippenstein, S. J. & Jasper, A. W. Ab initio methods for reactive potential surfaces. *Phys. Chem. Chem. Phys.* **9,** 4055–4070 (2007).

45.   Tang, X., Ratliff, B. J., FitzPatrick, B. L. & Butler, L. J. Determination of the Barrier Height for Acetyl Radical Dissociation from Acetyl Chloride Photodissociation at 235 nm Using Velocity Map Imaging †. *The Journal of Physical Chemistry B* **112,** 16050–16058 (2008).

46.   Peters, P. S., Duflot, D., Wiesenfeld, L. & Toubin, C. The H + CO ⇌ HCO reaction studied by ab initio benchmark calculations. *The Journal of Chemical Physics* **139,** 164310 (2013).

47.   Werner, H.-J. *et al. MOLPRO, version 2012.1, a package of ab initio programs.* (2012).

48.   Mordaunt, D. H., Osborn, D. L. & Neumark, D. M. Nonstatistical unimolecular dissociation over a barrier. *The Journal of Chemical Physics* **108,** 2448–2457 (1998).

49.   Chen, S. & Fang, W.-H. Insights into photodissociation dynamics of acetaldehyde from ab initio calculations and molecular dynamics simulations. *The Journal of Chemical Physics* **131,** 054306 (2009).

50.   Rubio-Lago, L., Amaral, G. A., Arregui, A., González-Vázquez, J. & Bañares, L. Imaging the molecular channel in acetaldehyde photodissociation: roaming and transition state mechanisms. *Phys. Chem. Chem. Phys.* **14,** 6067–6078 (2012).

51.   Keller-Rudek, H., Moortgat, G. K., Sander, R. & Sörensen, R. The MPI-Mainz UV/VIS Spectral Atlas of Gaseous Molecules of Atmospheric Interest. *Earth System Science Data* **5,** 365–373 (2013).

52.   Moortgat, G. K., Meyrahn, H. & Warneck, P. Photolysis of Acetaldehyde in Air: CH4, CO and CO2 Quantum Yields. *ChemPhysChem* **11,** 3896–3908 (2010).

53.   Parmenter, C. S. & Albert Noyes, W. Energy Dissipation from Excited Acetaldehyde Molecules. *J. Am. Chem. Soc.* **85,** 416–421 (1963).

54.   Pechukas, P. & Light, J. C. On Detailed Balancing and Statistical Theories of Chemical Kinetics. *The Journal of Chemical Physics* **42,** 3281–3291 (1965).

55.   Nesbitt, D. J. *et al.* Photofragmentation dynamics of ketene at 308 nm: Initial vibrational and rotational state distributions of CO product by vacuum UV laser-induced fluorescence. *The Journal of Chemical Physics* **83,** 223–229 (1985).

56.   Konen, I. M., Li, E. X. J., Stephenson, T. A. & Lester, M. I. Second OH overtone excitation and statistical dissociation dynamics of peroxynitrous acid. *The Journal of Chemical Physics* **123,** 204318 (2005).

57.   Hunter, M., Reid, S. A., Robie, D. C. & Reisler, H. The monoenergetic unimolecular reaction of expansion-cooled NO2: NO product state distributions at excess energies 0–3000 cm−1. *The Journal of Chemical Physics* **99,** 1093–1108 (1993).

58.   Green, W. H., Moore, C. B. & Polik, W. F. Transition States and Rate Constants for Unimolecular Reactions. *Annu. Rev. Phys. Chem.* **43,** 591–626 (1992).

5.8   **Phase space theory for unimolecular dissociation appendix**

The underpinning of statistical rate theories for unimolecular dissociation is that a microcanonical ensemble is maintained throughout dissociation *i.e.* energy can freely flow between rotation, vibration and translation. The rate is determined by counting the states that satisfy conservation of energy and angular momentum. One method to calculate the rate of statistical unimolecular dissociation is to view the process in reverse: recombination of the products to form a complex. A prerequisite in applying this method, phase space theory (PST),[54] is that no barrier to recombination exists *i.e.* the transition state must be sufficiently loose that the reaction coordinate along the potential energy surface does not influence the rate of combination. Alternative theories for calculating the properties of unimolecular dissociation require more information about the potential energy surface, but can be modified to be appropriate for systems both with and without a barrier in the reaction coordinate, examples are Rice-Ramsperger-Kassel-Marcus (RRKM) and statistical adiabatic channel model (SACM).

5.8.1   **Rotational phase space theory calculation**

PST calculates the phase space volume accessible for the dissociation of a parent molecule into fragments while conserving energy and angular momentum. We describe the energy levels for two polyatomic fragments as symmetrical tops rotating with energy E_{J_1,K_1} & E_{J_2,K_2}. Angular momentum conservation requires the total angular momentum of the parent molecule $\boldsymbol{J_{\text{parent}}}$ to equal the vector sum of the angular momenta of the fragments $\boldsymbol{J_1}$ & $\boldsymbol{J_2}$ and the orbital angular momenta of the fragments $\boldsymbol{L}$.

$$\boldsymbol{J_{\text{parent}}} = \boldsymbol{J_1} + \boldsymbol{J_2} + \boldsymbol{L}$$
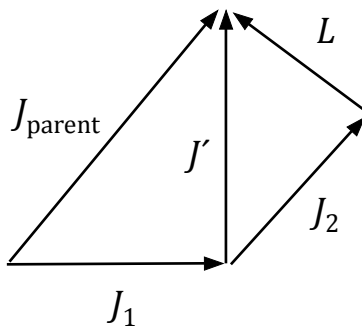
Figure 5-12. Evaluating nested triangle inequalities satisfies angular momentum conservation.

The energy available is defined as $E^{\ddagger} = h\nu - D_0$, where $h\nu$ is the photon energy and D_0 is the bond dissociation energy. Energy conservation allows all states that satisfy $E^{\ddagger} > E_{J_1,K_1} + E_{J_2,K_2}$. The anticipated rotational state population distribution P_{rot} for fragments 1 & 2 is given by

$$P_{rot}\left(J_1, J_2; J_{\text{parent}}, E^{\ddagger}\right) =$$

$$\sum_{J_1=0}^{J_1 \leq J_1^{max}(E^{\ddagger})} \sum_{K_1=0}^{K_1 \leq J_1(E^{\ddagger})} \sum_{J_2=0}^{J_2 \leq J_2^{max}(E^{\ddagger}-E_{J_1,K_1})} \sum_{K_2=0}^{K_2 \leq J_2(E^{\ddagger}-E_{J_1,K_1})} \sum_{J'=|J_{\text{parent}}-J_1|}^{J' \leq J_{\text{parent}}+J_1} \sum_{L=|J'-J_2|}^{L \leq J'+J_2} g(K_1) \cdot g(K_2)$$

The preparation of the parent molecule in a molecular beam is assumed to quench vibrational excitation, leaving only modest rotational excitation, $J_{\text{parent}} \sim 5$. In common with other authors, the small energy associated with parent rotation is neglected. The summation above is equivalent to the statement that all J_1, K_1, J_2, K_2 product states that satisfy conservation of angular momentum and energy are counted, with the degeneracy for $K \neq 0$ counted as 2, and otherwise 1. Conservation of angular momentum is evaluated in two steps for the triangle inequalities. A centrifugal barrier to limit accessible orbital angular momentum L is incorporated into descriptions of PST. However, most often the centrifugal barrier restricts the accessible phase space

141

inconsequentially, as such we neglect this user defined parameter entirely. J degeneracy is implicitly incorporated by the summation over accessible orbital angular momentum L, the number of states from the vector addition is equal to that anticipated for two rotors: $g(J_1) \cdot g(J_1) = (2J_1 + 1)(2J_2 + 1)$. It is desirable to include break statements to curtail the summation over states that are energetically inaccessible, however careful consideration of the energy level pattern is required. The 'zig-zag' structure in prolate and oblate symmetric top energy levels for increasing J, K means that while $E(J, K)$ may exceed $E^\ddagger$, $E(J + 1, K')$ may not. Erroneously breaking the summation over J & K for the first state to exceed $E^\ddagger$ significantly curtails the number states included in the phase space. Schematically the difference in the state count is illustrated in Figure 5-13.
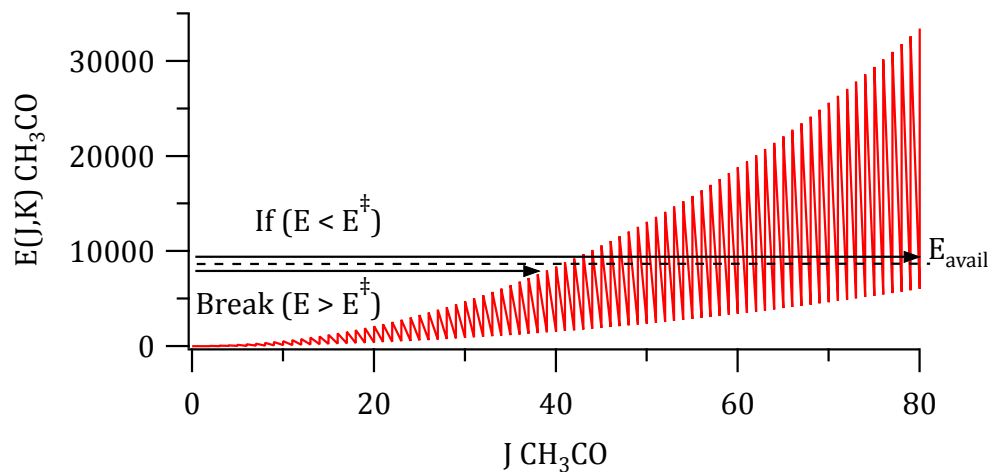
Figure 5-13. Energy of CH_3CO in wavenumbers approximated as a symmetric top as a function of rotational quantum number J.

5.8.2 Separate statistical ensembles calculation

Wittig and coworkers noted that PST calculations often underestimate vibrational excitation in the products of a statistical dissociation. By restricting the density of states to the disappearing vibrational modes, the separate statistical ensembles (SSE) model has successfully predicted product vibrational distributions P_{vib} in NCNO (10.1063/1.449681),[39] ketene[55] (10.1063/1.449812) & HOONO (10.1063/1.2126968).[56] The density expression (10.1063/1.449681) can be recast (10.1063/1.465408),[57] obviating the necessity to evaluate the vibrational density of states.

$$P_{vib}(v_1, v_2) = \frac{\rho^4(E^\ddagger - E_{v_2} - E_{v_1}) \cdot g_{v_2} \cdot g_{v_1}}{\sum_{E_{v_1}}^{E^\ddagger} \sum_{E_{v_2}}^{E^\ddagger - E_{v_1}} \rho^4(E^\ddagger - E_{v_2} - E_{v_1}) \cdot g_{v_2} \cdot g_{v_1}}$$

$$= \frac{(E^\ddagger - E_{v_2} - E_{v_1})^{(0.5T-1)} \cdot g_{v_2} \cdot g_{v_1}}{\sum_{E_{v_1}}^{E^\ddagger} \sum_{E_{v_2}}^{E^\ddagger - E_{v_1}} (E^\ddagger - E_{v_2} - E_{v_1})^{(0.5T-1)} \cdot g_{v_2} \cdot g_{v_1}}$$

T is the number of vibrational modes that disappear upon breaking the parent molecule into fragments 1 and 2, for example in $CH_3CHO \rightarrow CH_3 + HCO$ the parent molecule has 15 vibrational modes; while in the products there are 6+3 modes, leading to 6 disappearing vibrational modes. The vibrational population is proportional to $(E - E_v)^{0.5T-1}$, inspection of the $P_{vib}(v_1, v_2)$ matrix indicates significant vibrational excitation in both CH_3 and HCO simultaneously, a result of both the large exponent and non-zero degeneracy terms for CH_3. g = 1, 1, 2, 2 for v = 3004, 606, 3161, 1396 cm^{-1}.

Wittig and coworkers reported rotational state distributions for CN(v=0) from NCNO using SSE.

First the population of each allowed vibrational state, $P_{vib}(v_1, v_2)$ is determined, and a rotational PST (rPST) distribution calculated at the energy $E^{\ddagger} - E_{v_2} - E_{v_1}$. The P_{rot} from each rPST must be normalized prior to summation, as the contribution to the overall population is determined by P_{vib}.

$$P_{rovib}(J_1, J_2) = \sum_{v_1}^{v_1 \leq v_1^{max}(E^{\ddagger})} \sum_{v_2}^{v_2 \leq v_2^{max}(E^{\ddagger}, v_1)} P_{vib}(v_1, v_2) \cdot P_{rot}(J_1, J_2; J_{parent}, [E^{\ddagger} - E_{v_2} - E_{v_1}])$$

5.8.3 Efficient computation using a single rotational PST calculation

The computational expense grows rapidly with the number of accessible vibrational states, for example CH_3 + HCO products from the photolysis of CH_3CHO at λ = 266 nm ($E^{\ddagger}$ = 8645 cm^{-1}) can form in 127 different vibrational states of CH_3 and 49 states of HCO. Summation would require 6223 rPST calculations to be evaluated.

The rotational state population matrix $P_{rot}(J_1, J_2)$ for $v_1 = 0$ and $v_2 = 0$ can be manipulated into a one dimensional translational energy distribution by use of $E_T = E^{\ddagger} - E_{J_1, K_1} - E_{J_2, K_2}$. The translational energy distribution associated with vibrationally excited products $P_{trans}(E_T; v_1', v_2')$ is just that of $P(E_T; v_1 = 0, v_2 = 0)$ offset to lower E_T by $E_{v_1'} + E_{v_2'}$. Conservation of energy is satisfied by discarding population with $E_T < 0$, and conservation of angular momentum is unchanged, vastly reducing the computational cost as a single rPST calculation can proves sufficient. In SSE the vibrational population determines the contribution to the overall distribution, so each translational energy distribution is normalized to 1 prior to summation.

$$P(E_T) = \sum_{v_1}^{v_1 \le v_1^{max}(E^{\ddagger})} \sum_{v_2}^{v_2 \le v_2^{max}(E^{\ddagger}, v_1)} P_{vib}(v_1, v_2) \cdot P_{trans}(E_T; v_1{}', v_2{}')$$

5.8.4   Vibrational phase space theory calculation

Expressing the product vibrational population distribution found by PST in a similar form to the SSE model introduced above emphasizes the additional vibrational excitation in the SSE model over PST. Transition-state theories, such as PST separate the reaction coordinate from other degrees of freedom, leading to an ensemble of $T - 1$ oscillators; the vibrational population is then proportional to $(E - E_v)^{0.5T-0.5}$ (10.1146/annurev.pc.43.100192.003111).[58]

$$P_{vib}(v_1, v_2) = \frac{(E^{\ddagger} - E_{v_2} - E_{v_1})^{(0.5T-0.5)} \cdot g_{v_2} \cdot g_{v_1}}{\sum_{E_{v_1}}^{E^{\ddagger}} \sum_{E_{v_2}}^{E^{\ddagger}-E_{v_1}} (E^{\ddagger} - E_{v_2} - E_{v_1})^{(0.5T-0.5)} \cdot g_{v_2} \cdot g_{v_1}}$$

6 APPENDIX

6.1 Image analysis

```
/////////////////////////////////////////////////////////////
Function randtheta([w,molecule,bkgnd])
wave w, bkgnd
string molecule
string units = "cm-1"

        if (paramisdefault(w))
        string imagefocused= StringFromList(0,ImageNameList("",";"))
        wave w = ImageNameToWaveRef("",imagefocused)
        endif

        if (paramisdefault(molecule))
        molecule = "S-co"
        Print "Molecule:", molecule
        endif

        duplicate/O w workWav
        if (!paramisdefault(bkgnd))
                workWav = w - bkgnd
        endif

if ( numpnts(w) < 5 )
        Print "Focus on an image to use this function; put cursor A at the center"
else
Print nameofwave(w)

wave molecule_out = PickMolecule_v2(molecule)
//print molecule_out       // tof, mass_ion, mass_cofragment, multiplier_factor, scale
variable deltaV = molecule_out[4] / molecule_out[3] / molecule_out[0]

variable m = dimsize(w,0)
variable n = dimsize(w,1)
variable dx = dimdelta(w,0)
variable dy = dimdelta(w,1)
//print "m =", m, "n =", n, "dx =", dx, "dy =", dy

// redimension speed scaling based on image size
deltaV *= 1024 / dimsize(w,0)

variable cursor_center = 1 // looks at image in focus
 if (cursor_center == 1)
        xc = pcsr(a)
        yc = qcsr(a)
 endif

variable manual_center = 0 // manual override
 if (manual_center == 1)
        xc = 517
```

146

```
            yc = 602
    endif
    print "Xcursor =", xc, "Ycursor =", yc


/////////////////////////////////////// polar transform ///////////////////////////////////////////
Make/O/N=(m,n) radiusWave= round(sqrt(dx^2*(p-xc)^2+dy^2*(q-yc)^2))
Make/O/N=(m,n) angleWave= round((atan2((q-yc)*dy,(p-xc)*dx)+Pi)*180/Pi) // degrees

        variable timerRefNum = StartMSTimer
        Make/O/N=(wavemax(radiusWave)+1,(wavemax(angleWave)+1)) polarWave = 0
        variable i, j
                for(i=0; i< dimsize(w,0); i+=1)
                for(j=0; j< dimsize(w,1); j+=1)
                polarWave[radiusWave[i][j]][angleWave[i][j]] += workWav[i][j]
                endfor
                endfor
        variable elapsedTime = StopMSTimer(timerRefNum) / 1E6
        Print "Polar calc: ", elapsedTime, " seconds"
        timerRefNum = StartMSTimer

Duplicate/O/R=[0,(dimsize(w,0)/2)-1][0,wavemax(angleWave)-1] polarWave, polarWave1
Duplicate/O polarWave1, polarWave
Killwaves polarWave1

        DFREF dfrSave = GetDataFolderDFR()
        NewDataFolder/S/O V
        DFREF dfrStored = GetDataFolderDFR()


/////////////////////////////////////// speed distribution ///////////////////////////////////////////
string nameStr = trim_str_img(w)
string sliceStr =  nameStr +"_iP"
Make/O/N=(dimsize(polarWave,0)) $sliceStr = 0
wave V_wav = $sliceStr
                for(i=0; i< dimsize(polarWave,0); i+=1) // radius
                for(j=0; j< dimsize(polarWave,1); j+=1) // theta
                V_wav[i] += polarWave[i][j] * i *  abs(cos(j/180*Pi))
                endfor
                endfor

SetScale/P x 0,deltaV,"" V_wav
string notes1 = "molecule: " + molecule + ", tof: " + num2str(molecule_out[0]) + ", scale: " +
num2str(molecule_out[4]) + ", multiplier: " + num2str(molecule_out[3])
string notes2 = "mass_ion: " + num2str(molecule_out[1]) + ", mass_cofragment: " + num2str(molecule_out[2])
Note V_wav, notes1
Note V_wav, notes2
        NewDataFolder/S/O V_quad_avg
        DFREF dfrQuad_avg = GetDataFolderDFR()
        SetDataFolder dfrStored
        NewDataFolder/S/O V_quad
        DFREF dfrQuad= GetDataFolderDFR()
/////////////////////////////////////// speed quadrants ///////////////////////////////////////////
variable  quarter_angle = dimsize(polarWave,1)/4

string Squad_1 = nameStr +"_iP1", Squad_2 = nameStr +"_iP2", Squad_3 = nameStr +"_iP3", Squad_4 = nameStr
+"_iP4"
```

```
Make/O/N=(dimsize(polarWave,0)) $Squad_1 = 0, $Squad_2 = 0, $Squad_3 = 0, $Squad_4 = 0
wave quad_1 = $Squad_1, quad_2 = $Squad_2, quad_3 = $Squad_3, quad_4 = $Squad_4

        for(i=0; i< dimsize(polarWave,0); i+=1) // radius
        for(j=0; j< quarter_angle; j+=1) // theta
                quad_1[i] += polarWave[i][j]                    * i *  abs(cos(j/180*Pi))
                quad_2[i] += polarWave[i][j+1*quarter_angle] * i *  abs(cos((j+1*quarter_angle)/180*Pi))
                quad_3[i] += polarWave[i][j+2*quarter_angle] * i *  abs(cos((j+2*quarter_angle)/180*Pi))
                quad_4[i] += polarWave[i][j+3*quarter_angle] * i *  abs(cos((j+3*quarter_angle)/180*Pi))
        endfor
        endfor

string V_Str_avg = nameStr +"_iP_avg", V_Str_avg_sd = nameStr +"_iP_avg_sd"
string quad_list = Squad_1 + ";" + Squad_2 + ";" + Squad_3 + ";" + Squad_4
SetScale/P x 0,deltaV,"" quad_1, quad_2, quad_3, quad_4
fwaveaverage(quad_list,"",1,1,V_Str_avg,V_Str_avg_sd)

wave V_Wave_avg = $V_Str_avg, V_Wave_avg_sd = $V_Str_avg_sd
SetScale/P x 0,deltaV,"" V_Wave_avg, V_Wave_avg_sd
wavestats/Q V_Wave_avg_sd
variable quad_error = V_rms
Duplicate/O V_Wave_avg, dfrQuad_avg:$V_Str_avg
Duplicate/O V_Wave_avg_sd, dfrQuad_avg:$V_Str_avg_sd
killwaves V_Wave_avg, V_Wave_avg_sd

/////////////////////////////////// energy distributions ///////////////////////////////////
        SetDataFolder dfrSave
        NewDataFolder/S/O E
        wave e_out = Speed_to_E_linear_igor(units,molecule,V_wav)
        elapsedTime = StopMSTimer(timerRefNum) / 1E6
        Print "Speed calc: ", elapsedTime, " seconds"
        killwaves radiusWave, angleWave
        Killwaves molecule_out

/////////////////////////////////// calculate beta ///////////////////////////////////
        SetDataFolder dfrSave
        NewDataFolder/S/O B2
        dfrStored = GetDataFolderDFR()
        timerRefNum = StartMSTimer
                string betaStr =  nameStr + "_iB2"
                make/O/N=(dimsize(polarWave,0)) $betaStr
                wave betaWave2 = $betaStr
                make/N=2/O W_coef
                variable thickness = 1 // must be 1 or greater
                for (i=0; i < dimsize(polarwave,0); i+=1)
                        Duplicate/O/R=[i-thickness,i+thickness][] PolarWave, thetaWave2
                        MatrixOp/O thetaWave3 = sumcols(thetaWave2)
                        Redimension/N=360 thetaWave3
                        W_coef[0] = {0,0}
                        FuncFit/N/Q/NTHR=0/W=2 aniso W_coef thetaWave3/D
                        betaWave2[i] = w_coef[1]/w_coef[0]
                        //print "beta =", beta2
                endfor
        elapsedTime = StopMSTimer(timerRefNum) / 1E6
        Print "Beta2: ", elapsedTime, " seconds"
```

148

```
wave W_sigma
string fitString = "fit_" + nameofwave(thetaWave3)
wave fitWave = $fitString
killwaves W_coef, W_sigma, fitWave
killwaves thetaWave2, thetaWave3
betaWave2 = (NumType(betaWave2)==2) ? 0 : betaWave2
SetScale/P x 0,deltaV,"" betaWave2

//////////////////////////////////// beta quadrants ////////////////////////////////////////
        NewDataFolder/S/O B2_quad_avg
        dfrQuad_avg = GetDataFolderDFR()
        SetDataFolder dfrStored
        NewDataFolder/S/O B2_quad
        dfrQuad= GetDataFolderDFR()
        timerRefNum = StartMSTimer
                string betaStr_1 =  nameStr +"_iB2_1", betaStr_2 =  nameStr +"_iB2_2", betaStr_3 =  nameStr
                +"_iB2_3", betaStr_4 = nameStr+"_iB2_4"
                make/O/N=(dimsize(polarWave,0)) $betaStr_1 =  0,  $betaStr_2 =  0,  $betaStr_3 =  0,
                $betaStr_4 = 0
                wave  betaWave_1 = $betaStr_1,  betaWave_2 = $betaStr_2,  betaWave_3 = $betaStr_3,
                betaWave_4 = $betaStr_4
                make/O/N=(dimsize(polarWave,0),4) beta_2D
                make/N=2/O W_coef
                for (j=0; j < 4; j+=1)
                for (i=0; i < dimsize(polarwave,0); i+=1)
                        Duplicate/O/R=[i-thickness,i+thickness][j*quarter_angle,(j+1)*quarter_angle]
                        PolarWave, thetaWave2
                        MatrixOp/O thetaWave3 = sumcols(thetaWave2)
                        Redimension/N=(quarter_angle) thetaWave3
                        W_coef[0] = {0,0}
                                if        (j == 0 || j ==      2)
                                        FuncFit/N/Q/NTHR=0/W=2 aniso W_coef thetaWave3/D
                                elseif (j == 1 || j ==         3)
                                        FuncFit/N/Q/NTHR=0/W=2 aniso_90 W_coef thetaWave3/D
                                else
                                        Print "error in quadrants"
                                endif
                        beta_2D[i][j] = w_coef[1]/w_coef[0]
                        //print "beta =", beta2
                endfor
                endfor
                betaWave_1 = beta_2D[p][0]
                betaWave_2 = beta_2D[p][1]
                betaWave_3 = beta_2D[p][2]
                betaWave_4 = beta_2D[p][3]
        elapsedTime = StopMSTimer(timerRefNum) / 1E6
        Print "Beta2 quadrants: ", elapsedTime, " seconds"

string betaStr_avg = nameStr +"_iB2_avg", betaStr_avg_sd = nameStr +"_iB2_avg_sd"
quad_list = betaStr_1 + ";" + betaStr_2 + ";" + betaStr_3 + ";" + betaStr_4
SetScale/P x 0,deltaV,"" betaWave_1, betaWave_2, betaWave_3, betaWave_4
fwaveaverage(quad_list,"",1,1,betaStr_avg,betaStr_avg_sd)
wave betaWave_avg = $betaStr_avg, betaWave_avg_sd = $betaStr_avg_sd
SetScale/P x 0,deltaV,"" betaWave_avg, betaWave_avg_sd
```

```
Duplicate/O betaWave_avg, dfrQuad_avg:$betaStr_avg
Duplicate/O betaWave_avg_sd, dfrQuad_avg:$betaStr_avg_sd
killwaves betaWave_avg, betaWave_avg_sd
wave W_sigma
wave fitWave = $fitString
killwaves W_coef, W_sigma, fitWave
killwaves thetaWave2, thetaWave3, beta_2D
        Endif

setdatafolder dfrSave
return quad_error
End
/////////////////////////////////////////////////////////////



/////////////////////////////////////////////////////////////
Function/S trim_str_img(w)
wave w

                        string wName = nameofwave(w)
                        variable var_str = grepstring(wName,"_img_")
                                if (var_str == 1)
                                        string Str_1, Str_2, Str_3
                                        string Str_expr = "(.*)(\_img)(.*)"
                                        splitstring/E=(Str_expr) wName, Str_1, Str_2, Str_3
                                        string Str_New = Str_1 + Str_3
                                        print "New name: ", Str_New
                                else
                                        Str_New = wName
                                        print "Name not changed: ", Str_New
                                endif
        return Str_New
End
/////////////////////////////////////////////////////////////
```

```
//////////////////////////////////////////////////////////////
Function aniso(w,theta) : FitFunc
        Wave w
        Variable theta

        //CurveFitDialog/ These comments were created by the Curve Fitting dialog. Altering them will
        //CurveFitDialog/ make the function less convenient to work with in the Curve Fitting dialog.
        //CurveFitDialog/ Equation:
        //CurveFitDialog/ f(theta) = p0 + p2*LegendreA(2,0,sin((theta/360)*2*Pi))
        //CurveFitDialog/ End of Equation
        //CurveFitDialog/ Independent Variables 1
        //CurveFitDialog/ theta
        //CurveFitDialog/ Coefficients 2
        //CurveFitDialog/ w[0] = p0
        //CurveFitDialog/ w[1] = p2

        return w[0] + w[1]*LegendreA(2,0,sin((theta/360)*2*Pi))
End
//////////////////////////////////////////////////////////////

//////////////////////////////////////////////////////////////
Function aniso_90(w,theta) : FitFunc
        Wave w
        Variable theta

        //CurveFitDialog/ These comments were created by the Curve Fitting dialog. Altering them will
        //CurveFitDialog/ make the function less convenient to work with in the Curve Fitting dialog.
        //CurveFitDialog/ Equation:
        //CurveFitDialog/ f(theta) = p0 + p2*LegendreA(2,0,cos((theta/360)*2*Pi))
        //CurveFitDialog/ End of Equation
        //CurveFitDialog/ Independent Variables 1
        //CurveFitDialog/ theta
        //CurveFitDialog/ Coefficients 2
        //CurveFitDialog/ w[0] = p0
        //CurveFitDialog/ w[1] = p2

        return w[0] + w[1]*LegendreA(2,0,cos((theta/360)*2*Pi))
End
//////////////////////////////////////////////////////////////
```

6.2 Speed to linear energy axis

```
/////////////////////////////////////////////////////////
Function/wave Speed_to_E_linear_igor(units,molecule,V_wav)
string units, molecule
wave V_wav

        wave molecule_out = PickMolecule_v2(molecule) // USING A SUBROUTINE
        variable   tof  =  molecule_out[0],  mass_ion  =  molecule_out[1],  mass_cofragment  =
        molecule_out[2]
        Make/O/N=(numpnts(V_wav)) Eaxis_E  // to make new wave for correct energy X scaling
        variable unit = output_units(units)
        Eaxis_E = unit* ((DimDelta(V_wav,0)) *p)^2 * mass_ion * 0.5 * 1.03639E-8 * ( mass_ion /
        mass_cofragment +1 )  // DimDelta   important as this is how we read Pixel to Velocity
        conversion in //
        variable Emax = wavemax(Eaxis_E)
        variable upscale = 250  // Upscale MUST match labview for intensities to be equal
        variable points = (upscale * Emax / unit ) + 1 // Matches labview to maintaining scaling
        string str_Eaxis_Ei = nameofwave(Eaxis_E) + "i"
        make/O/N=(points) $str_Eaxis_Ei = 0
        wave Eaxis_Ei = $str_Eaxis_Ei
        Eaxis_Ei = p * unit / upscale
        string notes = "interpolating: " + nameofwave(Eaxis_E) + " to " + nameofwave(Eaxis_Ei) + ",
        Emax:  " + num2str(Emax) + " " + units + ", upscale:  " + num2str(upscale) + " and points:  " +
        num2str(points)
        //print notes
        note Eaxis_Ei, notes
        string str_E = TrimWaveName_Energy_or_Velocity(V_wav)+"_iE"
        Make/O/N=(numpnts(V_wav)) $str_E = 0
        wave E_wav = $str_E
        E_wav = V_wav / p  /// Need to perform jacobian transformation on Pixel to Energy Y data
        E_wav[0] = 0 // get rid of unspecified point
        string str_Ei = TrimWaveName_Energy_or_Velocity(V_wav) + "_iEi"
        make/O/N=(numpnts(Eaxis_Ei)) $str_Ei = 0
        wave Ei_wav = $str_Ei
        Interpolate2/T=1/N=(numpnts(Eaxis_Ei))/I=3/Y=Ei_wav/X=Eaxis_Ei   Eaxis_E,   E_wav   //
        must supply /X= Xdest as it is used for scaling Emax
        Setscale/I x 0,Emax,"", Ei_wav
        string notes1 = "molecule: " + molecule + ", tof: " + num2str(molecule_out[0]) + ", scale: " +
        num2str(molecule_out[4]) + ", multiplier: " + num2str(molecule_out[3])
        string  notes2  =  "mass_ion:  "  +  num2str(molecule_out[1])  +  ",  mass_cofragment:  "  +
        num2str(molecule_out[2])
        note Ei_wav, notes
        note Ei_wav, notes1
        note Ei_wav, notes2
        killwaves E_wav,  Eaxis_Ei
        return Ei_wav

End
/////////////////////////////////////////////////////////
```

6.3 Islands: $I(r,\theta) \rightarrow I(E_T,\beta)$

```
/////////////////////////////////////////////////////////////
Function Islands_standalone(PEt,B2i,B2i_sd,[set_debug])
wave PEt, B2i, B2i_sd
variable set_debug

variable BEt_dim = numpnts(B2i) /1  // downscale beta to minimize array size
variable Emax = pnt2x(PEt,numpnts(PEt)), Emin = pnt2x(PEt,0)

            print "Axis max: ", Emax, "Wave points: ", numpnts(PEt), numpnts(B2i), numpnts(B2i_sd)
            print "Islands requires all waves have equal number of points, and assumes the
velocity/energy scaling for all waves is the same"
if (numpnts(PEt) == numpnts(B2i) && numpnts(PEt) == numpnts(B2i_sd)) // we require the population and
angular distributions to have the same number of points
                Make /O/N=(numpnts(B2i),BEt_dim) w_island
                wave w_island
                SetScale/I x Emin,Emax,"", w_island
                SetScale/I y -2,3,"", w_island
                variable number_sd = 2

w_island =  PEt[p] /(number_sd*B2i_sd[p]*sqrt(2*pi)) * exp(-( (y-B2i[p])^2 / (2*(number_sd*B2i_sd[p])^2)
)) // y scaling aware: Gaussian to be centered about correct value

        if (set_debug == 1) // check PEt recovered
                Make /O/N=(numpnts(B2i)) PEt_recovered = 0
                SetScale/I x Emin,Emax,"", PEt_recovered
                wave PEt_recovered
                MatrixOp/O PEt_recovered = SumRows(w_island)
        endif

endif
End
/////////////////////////////////////////////////////////////
```

6.4 Molecule database

```
////////////////////////////////////////////////////////////
Function/wave PickMolecule_v2(molecule)
string molecule
variable tof, mass_ion, mass_cofragment
variable coord_multiplier = 2, scale = 74.4
strswitch(molecule)
// String nomenclature: ION - COFRAGMENT //
case "S-co":
tof = 5.7032
mass_ion = 32.07
mass_cofragment = 28.05
break
case "I-ch2i":
tof = 11.3090
mass_ion = 126.90
mass_cofragment = 140.94
break
case "CH3-cho":
tof = 3.956
mass_ion = 15.03
mass_cofragment = 29.02
break // MUST break each case
default:
print "ERROR: must provide molecule to ensure correct fragment masses with an energy axis"
break
endswitch
make/O/N=5 molecule_out
molecule_out[0] = {tof, mass_ion, mass_cofragment, coord_multiplier, scale}
return molecule_out
End
////////////////////////////////////////////////////////////
```